Charles University in Prague

Faculty of Mathematics and Physics

DOCTORAL THESIS

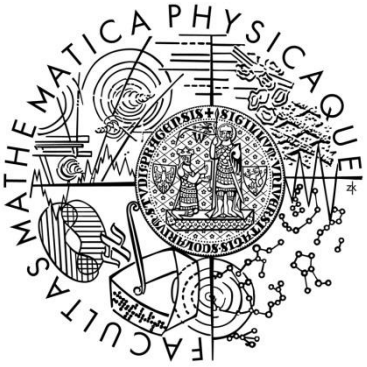

Klára Ševčíková

Study of dependence of the metal-oxide electron structure on the reactivity of these systems

Department of Surface and Plasma Science

Supervisor of the doctoral thesis: doc. RNDr. Václav Nehasil, Dr.

Study programme: Physics

Specialization: F-5 Surface and Interface Physics

Prague 2015

Acknowledgement

First of all, I would like to thank my supervisor, Václav Nehasil, for his guidance and support, both scientific and personal, during my studies at KFPP. It gave me a lot.

Secondly, I would like to express my gratitude to Yoshikawa Hideki-san, for supervising me during my stay at NIMS in Japan and for his endless patience with my oddities.

Special thanks go to Anli Yang-san whose brightness shines through every cloud. Thanks to her, I really enjoyed the one year spent in Aioi.

Furthermore, I would like to thank all colleagues at KFPP, namely Tatiana Kolářová, Miroslav Kettner, Petr Homola and Igor Píš, who were responsible for excellent working conditions and friendly atmosphere in the laboratory. I thank Kobayashi Keisuke-san, Kobata Masaaki-san and Sakata Osami-san for their consultations and support during my experiments at NIMS. Also, I would like to thank Vladimír Matolín who gave me the opportunity to travel and carry out the experiments at various laboratories.

I would like to thank all co-workers who participated at the experiments, especially Nataliya Tsud and Tomáš Skála who supervised the measurements at Materials Science Beamline, and Silvano Lizzit, Paolo Lacovig and Nicoleta Georgiana Apostol from the SuperESCA beamline at Elletra. Also, I thank Michal Václavů, Mykhailo Voroghta and Martin Dubau who prepared most of the samples, Stanislav Haviar who measured SEM, Lucie Szabová who performed DFT calculations, Jiří Libra who provided the excellent software for data processing and Yaroslava Lykhach who helped us with the interpretation and publication of our results.

The experiments performed at the BL15XU of SPring-8 were carried out with the approval of the Japan Synchrotron Radiation Research Institute (Proposals No. 2011B4063 and 2012A4604). I am thankful to the staff of BL15XU for excellent working conditions and their support during my experiments.

Finally, I would like to express my gratitude to my parents and my partner for supporting me during my studies and writing the thesis. Thank you for being there for me.

I declare that I carried out this doctoral thesis independently, and only with the cited sources, literature and other professional sources.

I understand that my work relates to the rights and obligations under the Act No. 121/2000 Coll., the Copyright Act, as amended, in particular the fact that the Charles University in Prague has the right to conclude a license agreement on the use of this work as a school work pursuant to Section 60 paragraph 1 of the Copyright Act.

In Prague, June 8, 2015 Mgr. Klára Ševčíková

Název práce: Studium vlivu elektronové struktury na reaktivitu systémů oxid–kov.

Autor: Klára Ševčíková

Katedra / Ústav: Katedra fyziky povrchů a plazmatu

Vedoucí doktorské práce: doc. RNDr. Václav Nehasil, Dr., Katedra fyziky povrchů a plazmatu

Abstrakt: Předkládaná práce je zaměřena na studium interakce rhodia a oxidu ceru a její vliv na jejich reaktivitu. Dva druhy systémů, Rh/CeO_x a Rh-CeO_x, byly charakterizovány pomocí metod fotoelektronové spektroskopie a teplotně programovaných reakcí. Rh/CeO_x značí systém složený z rhodiových nanočástic nesených tenkou vrstvou oxidu ceru. V této práci ukazujeme, že dochází k elektronické interakci a přenosu náboje mezi rhodiem a oxidem ceru. Tato interakce závisí na míře redukce oxidu ceru, a přitom značně ovlivňuje reaktivitu celého systému. Rh-CeO_x označuje tenké vrstvy oxidu ceru dopované rhodiem. V rámci této práce byly charakterizovány vlastnosti vrstev s různými koncentracemi rhodia. Ukazujeme, že struktura, složení a reaktivita těchto systémů je značně závislá na koncentraci rhodia ve vrstvě oxidu ceru.

Klíčová slova: Rhodium, oxid ceru, interakce oxid–kov, oxidace CO, migrace kyslíku

Title: Study of dependence of the metal-oxide electron structure on the reactivity of these systems

Author: Klára Ševčíková

Department / Institute: Department of Surface and Plasma Science

Supervisor of the doctoral thesis: doc. RNDr. Václav Nehasil, Dr., Department of Surface and Plasma Science

Abstract: The presented thesis focuses on studying the interaction between rhodium and cerium oxide and its impact on the reactivity. We investigated two different systems, Rh/CeO_x and Rh-CeO_x, by means of the photoelectron spectroscopy and the temperature programmed reactions. Rh/CeO_x stands for rhodium nanoparticles supported by cerium oxide thin film. We show that there is an electronic metal-substrate interaction between rhodium and cerium oxide. The type of the interaction depends on a degree of cerium oxide reduction and it has a tremendous impact on the reactivity of the system. On the other hand, Rh-CeO_x represents cerium oxide thin films doped by rhodium. We characterized the properties of the films with various concentration of rhodium. We show that the morphology, chemical composition and reactivity of the samples strongly depend on the concentration of the rhodium dopant.

Keywords: Rhodium, cerium oxide, metal-oxide interaction, CO oxidation, oxygen migration

Contents

1 Introduction

Materials applicable in heterogeneous catalysis has been extensively studied during last few decades because of high demands of industry and society on improving efficiency and lowering the cost of the catalysts controlling environmental pollution, such as automotive exhaust converters [1], biomass gasification systems [2], or fuel cells [3]. In recent year, cerium oxide has been one of main subjects of research in the material science because it can be used as a component in many catalytic systems [4–8].

Cerium oxide is valued mostly for its high oxygen storage capacity (OSC) [9]. As a reducible oxide, it can easily and reversibly transform between two stable states, Ce^{3+} and Ce^{4+}. This transition is accompanied by the release or uptake of oxygen in dependence on the environment. Cerium oxide with a low degree of reduction (stoichiometry close to CeO_2, further referred as ceria) can supply oxygen to the surface reactions in the oxygen-lean environment, which would result in the reduction of Ce^{4+} ions. On the other hand, cerium oxide with a high degree of reduction (stoichiometry close to Ce_2O_3) can absorb excess oxygen from the reaction area leading to oxidation of Ce^{3+} ions. A facile formation of oxygen vacancies and a high mobility of oxygen atoms through the oxide are the main reasons for the wide usage of ceria [1, 9–11].

Cerium oxide, further referred as CeO_x ($1.5 < x < 2$), is often used as a support for nanoparticles of transition metals because it enhances their catalytic activity [12]. In such case, the reactions take place at the supported particles and cerium oxide acts as a buffer layer of oxygen [13]. The transport of oxygen between the particles and the substrate is therefore a very important property of the catalytic system.

The interaction between the metal particle and the oxide substrate is an important factor which can significantly influence the catalytic activity of the system [14]. Even small perturbations of the catalyst electron structure may have a great impact on its properties. These perturbations can be caused for example by the electron exchange between the particle and the oxide support, local electric fields generated by exposed ions of the support, or morphological changes due to the interaction of the particle with the oxide support. These phenomena are collectively called the electronic metal-support interaction (EMSI). The EMSI may enhance, or

suppress the activity of the catalyst depending on the combination and amount of materials [15].

In the case of reducible oxide, such as ceria, an ionic bond can be formed between the oxide surface and metal due to the exchange of electrons [15]. The charge transfer from the metal particles to the ceria support was reported for Pt/CeO_2 [3], Pd/CeO_2 [16], Au/CeO_2 [17], Rh/CeO_2 [18] or Cu/CeO_2 [19] systems. However, only few studies exist which deal with the effects of the metal deposition on reduced CeO_x surfaces [19].

In the presented work, we focus on the systems composed of rhodium and cerium oxide. Rhodium was chosen because it is extensively used in many catalytic systems, especially in automotive exhaust converters [1]. It is valued for its high selectivity to convert toxic nitrogen oxides to N_2 [12, 13]. It is also efficient in oxidizing the unsaturated hydrocarbons [20, 21]. Moreover, the synergetic enhancement of the catalytic activity was reported for the Rh/CeO_x system which makes it worth of interest [2, 22].

The catalytic activity of rhodium particles supported by cerium oxide was extensively studied by many researchers [21, 23–25]. It was found that the degree of cerium oxide reduction plays a key role in the reactivity of the system [26, 27]. While ceria can provide a high amount of oxygen to the reactions at the Rh particles, it is not so for cerium oxide with the high degree of reduction. Moreover, the interaction of molecules adsorbed on Rh/CeO_x is different depending on the degree of cerium oxide reduction. Stubenrauch et al. reported [23] that CO dissociates much more readily at the Rh particles supported by CeO_x with the higher degree of reduction compared to those supported by ceria. Mullins et al. hypothesized [27] that this effect could arise from the electronic interaction between the Rh particles and the CeO_x support. However, the origin of this effect has not been understood yet.

The structure of cerium oxide is another factor determining the activity of the Rh/CeO_x catalyst. Migani et al. [28] reported that the formation of oxygen vacancies in cerium oxide is much more facile at the systems composed of nanocrystals compared to highly oriented extended areas of the defectless ceria structure. Preparing and investigating cerium oxide thin films with various crystallinity and structure has been a major topic of research at the group of Prof Matolín in recent years [29–31]. These thin films are ideal for investigating the interaction between the Rh particles and the CeO_x substrate and its impact on the reactivity.

Doping ceria by another compound can also markedly alter its properties, namely the structure and catalytic activity. It was reported that mixing ceria with another oxide, such as ZrO_2 [32] or SiO_2 [33], or doping it with a metal, such as copper [34] or rhodium [35], can enhance the reducibility and OSC of ceria. The main role of the dopant is to disrupt chemical bonds in the host oxide. The disruptions at the surface area can create new adsorption positions. Also, the oxygen atoms near these sites engage more readily in chemical reactions [22, 36–38]. At the same time, the host oxide lattice can force the dopant into an atypical coordinative bonding which can change its chemical properties [39]. Therefore, the interaction of ceria and dopants is one of the main factors determining the reactivity of the system.

Only few studies exist which report on the systems composed of cerium oxide doped by rhodium [35, 40–42]. These systems were prepared synthetically from powders or by wet chemical deposition methods. However, it is very difficult to achieve the high dispersion and homogeneous distribution of rhodium in ceria lattice using these methods. Radio frequency magnetron sputtering offers a possibility to easily prepare thin films of cerium oxide doped by a noble metal with the well-controlled concentration and the high dispersion of the dopant [34, 43, 44].

In the presented thesis, we investigated and compared two types of systems containing rhodium and cerium oxide. The first one was composed of rhodium particles supported by a thin film of cerium oxide (Rh/CeO_x). CeO_x substrates with different degrees of reduction (various values of x) were used for supporting the Rh particles. The second system consisted of a thin film of cerium oxide doped by rhodium (Rh-CeO_x). The films with various concentration of the dopant were investigated. A special attention was paid to the interaction between rhodium and cerium oxide and its impact on the catalytic activity of the system.

The presented work is mostly experimental but some results are supported by calculations based on the density functional theory. These were performed by Dr Lucie Szabová. The experiments were carried out at various laboratories managed by the Department of Surface and Plasma Science (KFPP) at Charles University in Prague in the Czech Republic and the National Institute for Materials Science (NIMS) in Japan. Furthermore, several experiments were performed at beamtimes at the SPring-8 and Elettra synchrotrons. While the electron structure of the samples was investigated by means of the photoelectron spectroscopy (PES), their reactivity was studied by the temperature programmed reactions (TPR). The X-ray diffraction

(XRD) and the scanning electron microscopy (SEM) were used to check the morphology of the samples. The SEM imaging was performed by Dr Stanislav Haviar.

The results are presented in two chapters dealing separately with the Rh/CeO_x and Rh-CeO_x systems. Both chapters are divided to several sections according to their topics. An individual chapter is dedicated to the preparation of the samples, experimental methods, computation details, and processing and analysing of the data.

2 Materials and methods

2.1 Samples

In the whole document, we use the following notation for designating the samples. The name of every sample consists of several parts. The individual parts mark the compounds or elements forming the sample. The first part (read from the left) corresponds to the surface, while the last one designates the substrate. A slash refers to an interface between two different materials or phases. A dash is used for marking a dopant in a host oxide. Therefore, we distinguish $Rh/CeO_x/SiO_2/Si$ from $Rh\text{-}CeO_x/SiO_2/Si$. While the latter refers to a cerium oxide thin film doped by rhodium and supported by a silicon substrate with an enhanced layer of silicon oxide, the former designates the rhodium particles supported by the cerium oxide thin film on the same silicon-based substrate. We often omit the parts corresponding to the support for better readability of the text. Therefore, the labels of the previously mentioned samples, $Rh/CeO_x/SiO_2/Si$ and $Rh\text{-}CeO_x/SiO_2/Si$, will be reduced to Rh/CeO_x and $Rh\text{-}CeO_x$. The list of all samples, their short names, corresponding substrates and details of the preparation can be found in Appendix A.

2.1.1 $Rh/CeO_x/Cu(111)$ model thin films

Model cerium oxide thin films can be prepared by evaporating metallic cerium in oxygen atmosphere. Following the procedure developed and published by the group of Matolín [29], an epitaxial thin film of CeO_2 grows on the copper single crystal with the surface orientation (111). The model CeO_x thin films were prepared and investigated at MSB at Elettra. These films were used to study the interaction between rhodium and cerium oxide with various degrees of reduction. The list of all samples can be found in Appendix A.

The Cu(111) crystal provided by MaTecK (99.999%, 8 mm diameter) was cleaned in UHV by several cycles of Ar ion sputtering and annealing to 750 K. The surface cleanliness was checked by monitoring the C 1*s* photoelectron signal. No impurities were detected on the Cu(111) surface before the oxide deposition. The orientation of the surface was checked by the low-energy electron diffraction (LEED). The crystal gave a sharp (1 x 1) LEED pattern.

An approximately 6 ML (~19 Å, considering 3.12 Å as the thickness of the O–Ce–O trilayer [45]) thin layer of CeO_2 was deposited onto the Cu(111) single crystal by evaporating cerium (Goodfellow, 99.99%) in $5 \cdot 10^{-7}$ mbar of O_2. A cerium evaporator consisted of a molybdenum crucible heated by an electron bombardment. The body of the evaporator was cooled down by water and it was equipped with a shutter to limit the degasing as much as possible. The temperature of the substrate was kept at 520 K. After the deposition, the sample was annealed 10 more minutes at 520 K and cooled down in $5 \cdot 10^{-7}$ mbar of O_2 to obtain stoichiometric CeO_2. LEED measurements confirmed the (1.5 x 1.5) pattern.

The reduction of the CeO_2 films was achieved by the evaporation of cerium in UHV. The temperature of the substrate was kept at 520 K in order to enhance the migration of oxygen towards the surface and moderate the gradient of the degree of reduction through the cerium oxide film. This method was developed by Duchoň et al. for preparing the ordered phases of reduced CeO_x [31]. They further annealed the samples in UHV up to 870 K enhancing the orderliness of the CeO_x films. In our case, we omitted the post-annealing to avoid the sintering of cerium oxide and exposing the copper substrate. LEED measurements of our films did not show any of the surface reconstructions reported in [31] but only the (1.5 x 1.5) pattern relative to Cu(111). This pattern became more diffusive for the films with the higher degree of reduction.

Rhodium (Goodfellow, 99.9%, wire of 0.5 mm diameter) was evaporated onto the model CeO_x thin films from an evaporator based on the electron bombardment. The evaporator was equipped with a shutter and a water cooling system to limit degasing during the deposition as much as possible. The temperature of the substrate was kept at 300 K and the pressure during the deposition did not exceed $4 \cdot 10^{-9}$ mbar. The Rh deposition was performed in several consecutive steps. The time of deposition did not exceed 1 min during every step. After every step, the photoelectron spectra were acquired to check the state of the sample. The amount of rhodium was determined from the XPS spectra (comparing the Rh/Ce relative intensity with the spectra of $Rh/CeO_x^{(Ox)}$ and $Rh/CeO_x^{(Red)}$). The deposition rate was estimated to 0.1 $nm \cdot min^{-1}$.

2.1.2 $Rh/CeO_x^{(Ox)}$ and $Rh/CeO_x^{(Red)}$

Cerium oxide thin films prepared by radio frequency magnetron sputtering were used as substrates for rhodium particles. The reactivity of the Rh/CeO_x systems was studied on these samples because they exhibit a higher oxygen storage capacity (OSC) than highly oriented cerium oxide thin films [46]. Thus, the reactions involving oxygen originating from the CeO_x substrate are enhanced and well observable. Two types of films were used for temperature programmed reactions: oxidized (Ox) and reduced (Red) cerium oxide.

Pieces of a p-doped Si wafer (10 x10 mm^2) with the surface orientation of (100) were used as supports. The substrates were cleaned ultrasonically in distilled water followed by cleaning in ethanol. The surface contained a few monolayers thin passivating SiO_2 layer.

The cerium oxide deposition was carried out *ex situ* in a vacuum chamber with the base pressure of $5 \cdot 10^{-6}$ mbar. The chamber was equipped with a balanced radio frequency magnetron provided by Kurt J. Lesker. The sputtering was performed in an Ar atmosphere ($4 \cdot 10^{-3}$ mbar) from a CeO_2 target (Kurt J. Lesker, 99.99%, 2 inch diameter) with the radio frequency power of 80 W. The temperature of the substrate was kept at around 300 K. A growth rate was approximately 1 $nm \cdot min^{-1}$. It was estimated from the deposition onto the quartz crystal positioned near the Si substrates. The thickness of the cerium oxide films was approximately 20 nm. SEM measurements confirmed that these films have polycrystalline character with a grain size of about 15 nm.

The CeO_x/Si samples were introduced to the UHV chamber with the base pressure of $3 \cdot 10^{-10}$ mbar (XPS-TPR, KFPP). The photoelectron spectroscopy measurements showed that cerium oxide contains mostly Ce^{4+} ions (fitting the Ce 3*d* spectra showed the $CeO_{1.98}$ stoichiometry). However, the surface contained a high amount of carbonaceous contaminant judging from the intensity of the C 1*s* signal. Therefore, it was necessary to clean the samples before depositing rhodium.

Ion sputtering and annealing are very efficient methods for removing the contaminants from the cerium oxide surface. However, both of these processes lead to partial reduction of cerium oxide [47, 48]. We intended comparing the reactivity of Rh/CeO_x systems with highly oxidized and reduced cerium oxide. Therefore, we

developed cleaning procedures which would result in a desired stoichiometry of cerium oxide and a minimum amount of surface contaminants.

The $CeO_x^{(Ox)}$ substrate was cleaned by annealing up to 640 K for 10 minutes. This caused partial reduction of ceria and desorption of most of contaminants. The exposure by oxygen at 300 K ($5 \cdot 10^{-8}$ mbar) led to partial re-oxidation of the cerium oxide film. The resulting stoichiometry of cerium oxide was $CeO_{1.94}$. The $CeO_x^{(Red)}$ substrate was cleaned by a combination of Ar ion sputtering and heating. First, the film was sputtered for 15 minutes. Then, it was annealed for 10 minutes at 800 K. Thus, the sample was cleaned from all contaminants. However, annealing caused re-oxidation of the cerium oxide surface. Another sputtering (10 min, 1 μA) led to its reduction to the $CeO_{1.85}$ stoichiometry.

The deposition of rhodium was carried out from an evaporator equipped with a shutter based on the electron bombardment of Rh wire (Goodfellow, 99.9%, 0.5 mm diameter). 1 ML of rhodium was evaporated onto both $CeO_x^{(Ox)}$ and $CeO_x^{(Red)}$ substrates. The deposition rate was estimated using the quartz crystal to approximately 0.01 nm·min^{-1}. Due to the long time necessary for reaching 1 ML of rhodium (~40 min, considering the lattice parameter of Rh equal to 3.8 Å [49] and assuming the epitaxial growth [45]), the deposition was divided to 1 min cycles of evaporation onto the sample, and onto the closed shutter. Thus, we avoided overheating the samples due to a long deposition time. The temperature of the substrate was kept at approximately 300 K.

2.1.3 Rh-CeO_x thin films

A large part of the thesis is focused on thin films of cerium oxide doped by rhodium. This topic was studied over a long period of time at two scientific departments (KFFP in the Czech Republic, and NIMS in Japan). Various experimental methods (XPS, HXPS, RPES, XRD, and SEM) were combined to characterize the Rh-CeO_x thin films. All samples were prepared *ex situ* at laboratories of KFPP. An exception is a set of samples prepared *in situ* during a beamtime at MSB at Elettra. These samples will be described separately.

First, we will focus on the samples prepared at KFFP. The Rh-CeO_x films with different concentrations of rhodium were deposited onto the SiO_2/Si(100) substrates. The small pieces of a p-doped silicon wafer (10 x 10 mm^2, 5 x 5 mm^2) were ultrasonically cleaned in distilled water and ethanol. It was reported [50] that a

film of silicon oxide at the interface between the silicon support and the CeO_x-based overlayer partially prevents a migration of silicon into the cerium oxide. That is why the supports were annealed in air at 1430 K for 5 minutes to enhance the SiO_2 surface layer. Annealing of the supports was performed in a high-temperature ceramic oven. The rate of a temperature increment was 60 $K \cdot min^{-1}$. The supports cooled down quickly in an open oven. SEM side view imaging of the fractured support showed that the SiO_2 layer was approximately 60 nm thick.

The thin films of cerium oxide doped by rhodium were prepared in the same UHV chamber as the substrates for Rh/$CeO_x^{(Ox)}$ and Rh/$CeO_x^{(Red)}$. The sputtering was performed in an Ar atmosphere ($6 \cdot 10^{-3}$ mbar) from a composite target. It consisted of the CeO_2 pellet (Kurt J. Lesker, 99.99%, 2 inch diameter) covered by Rh wires and plates (Goodfellow, 99.9%). Several samples were prepared simultaneously. The sputtering was performed with the radio frequency power of 50 W. A growth rate was approximately 1 $nm \cdot min^{-1}$. A temperature of the substrates was kept at around 300 K. The thickness of the Rh-CeO_x films was approximately 20 nm. The concentration of rhodium in the Rh-CeO_x films was altered by placing different amounts of rhodium pieces onto the CeO_2 target. The composition of the thin films was estimated from XPS spectra measured after the deposition (more details can be found in Section 2.3.4). The concentration of rhodium reached values of 1, 2, 3, 5, 6, and 9%. If it was necessary to distinguish the samples with different concentrations of rhodium, the concentration was put into the name of the sample, e.g. Rh(1%)-CeO_x.

Furthermore, the samples prepared *in situ* at MSB at Elettra will be discussed. Two types of the support were used during these experiments. The first one was the SiO_2/Si(100) substrate prepared in the same way as described above. The second type of substrate was made of oxygen-free copper plates (Goodfellow, 99.9%, 10 x 10 mm^2). It was polished by a diamante paste and ultrasonically cleaned in distilled water and ethanol.

Rh-CeO_x films were deposited on Cu or SiO_2/Si supports at the preparation chamber of MSB at Elettra with a base pressure of $2 \cdot 10^{-9}$ mbar. The chamber was equipped by an unbalanced magnetron constructed at KFPP. The sputtering was performed in an Ar atmosphere ($6 \cdot 10^{-3}$ mbar) from the same composite target as described above with the radio frequency power of 45 W. It was possible to prepare only one sample during one sputtering. A temperature of the substrate was kept at

300 K. A growth rate was estimated to approximately 1 nm·min^{-1}. The calibration of the growth rate was performed by depositing the Rh-CeO_x thin film on a reference golden foil. The composition and thickness of the films were checked by XPS. The films were 6 nm thick and the concentration of rhodium was 0% (reference rhodium-free CeO_x), and 1 and 5% (Rh-CeO_x).

2.1.4 Thin films of cerium oxide doped by various elements

In this separate chapter, we briefly describe four samples containing cerium oxide films doped by gold, copper, fluorine or silicon. These films were prepared for various independent experiments. We demonstrate on them the effect of adding the dopant on cerium oxide.

F-CeO_x thin film was deposited *in situ* at SuperESCA by evaporating cerium contaminated by fluorine in oxygen atmosphere onto the Cu(111) single crystal. The parameters of the sample preparation are same as in Section 2.1.1.

Si-CeO_x thin film was prepared unintentionally due to a migration of silicon into the cerium oxide thin film deposited onto the Si(100) substrate [50]. The silicon substrate was covered by a native oxide film few monolayers thin. The deposition of cerium oxide was performed by magnetron sputtering at KFPP (same parameters as in Section 2.1.2). The layer was approximately 3 nm thin. The concentration of silicon dopant cannot be estimated because of mingling signals from the Si substrate and the Si dopant.

Au-CeO_x film was prepared *ex situ* by combining the radio frequency magnetron sputtering of CeO_2 and the simultaneous evaporation of Au. The Au-CeO_x film was deposited onto a C/SiO_2/Si(111) substrate in the laboratories of NIMS. The SiO_2/Si(111) support was prepared in the same way as the SiO_2/Si(100) support described in Section 2.1.3. It was covered by an amorphous carbon layer approximately 30 nm thick. The carbon films was deposited onto the SiO_2/Si(111) support by radio frequency magnetron sputtering in Ar atmosphere ($6\cdot10^{-3}$ mbar) from a graphite target (Goodfellow, 99.997%, 2 inch diameter). The deposition of cerium oxide was performed with the radio frequency power of 60 W in Ar atmosphere ($5\cdot10^{-3}$ mbar) from a CeO_2 target (Kurt J. Lesker, 99.99%, 2 inch diameter). Gold was evaporated simultaneously from the evaporator based on the electron bombardment of an Au wire (Goodfellow, 99.999%, 0.5 mm diameter). The Au-CeO_x layer was about 4 nm thick. The concentration of gold was approximately

5%. A temperature of the sample was kept at 300 K during entire deposition. The Au-CeO_x/C/SiO_2/Si(111) sample was originally prepared as a reference for the high-surface Au/CeO_x/C/SiO_2/Si(111) systems discussed in [51].

Cu-CeO_x thin film was prepared *ex situ* by radio frequency magnetron sputtering onto the previously described SiO_2/Si(100) support. The sputtering was performed at the laboratories of KFPP simultaneously from two magnetrons in Ar atmosphere ($4 \cdot 10^{-3}$ mbar) and at 300 K. Copper and cerium oxide targets were used (Cu: Kurt J. Lesker, 99.9%, 2 inch; CeO_2: Kurt J. Lesker, 99.99%, 2 inch). The radio frequency power was 50 W (CeO_2 magnetron) and direct current power was 50 W (Cu magnetron). The Cu-CeO_x layer was approximately 25 nm thick and contained 8% of copper.

2.2 Experimental methods

2.2.1 Photoelectron spectroscopy

The photoelectron spectroscopy is a technique based on an external photoelectric effect giving the information about the chemical state of the material. It analysis the kinetic energy of electrons liberated from the surface of a material which is caused by the interaction with incident photons. The amount of detected photoelectrons with the specific kinetic energy (E_k) is proportional to the density of states with the corresponding binding energy (E_B). The kinetic and binding energies are bound by a simple relation

$$E_k = h\nu - E_B - e\varphi, \qquad (1)$$

where $h\nu$ stands for the energy of photons, e is the electron charge and φ is a constant representing the work function of the analyser. This constant is unknown but independent of the photoelectron energy and the spectra can be calibrated by shifting the energy according to the position of the known spectral lines (usually Au $4f_{7/2}$).

We can see from Equation (1) that the kinetic energy of emitted electrons depends on the energy of exciting photons. The energy of the incident photons also determines which core levels can be studied. If the energy of photons is not sufficient for emitting an electron from a core level, we can observe no signal from that level. Furthermore, the cross-section of photoemission from a specific level varies for

different energies of incident photons. The signal from the levels close to the Fermi energy is much lower when using the high-energy photons compared to low-energy photons [52]. Therefore, studying core levels or valence band region in ideal conditions requires an optimal photon source.

Within this work, we used various X-ray sources in order to study the electron structure of the samples. Al Kα (1486.3 eV) and Cr Kα (5414.7 eV) anodes were used alongside with tuneable synchrotron radiation sources (MSB and SuperESCA at Elettra, BL15XU at SPring-8). While hard X-ray photoelectron spectroscopy (HXPS, photon energies above 2 keV) was used for measuring deep core levels (such as Ce 3*p*), the core levels close to the Fermi energy (such as Rh 3*d*) were studied using soft X-rays (SXPS, photon energies between 125 and 650 eV). Valence band structures were investigated by means of the ultra-violet photoelectron spectroscopy (UPS, photon energies between 3 and 125 eV). Standard X-rays (XPS, photon energies of 1486.3 eV and 1256.0 eV) were used for acquiring the photoelectron spectra from core levels, such as Ce 3*d*.

One important difference between HXPS, XPS and SXPS is the information depth of the methods. The inelastic mean free path (IMFP) of high-energy electrons in a specific material is significantly longer compared to low-energy electrons. For instance, the detection depth of XPS in cerium oxide doped by rhodium was determined to 5 nm, considering the inelastic mean free path of O 1*s* photoelectrons in Rh-CeO_x [53]. The information depth of HXPS was estimated to be higher than 20 nm. Therefore, the majority of the HXPS signal comes from the deeper layers of the sample. The contribution of surface adsorbates is negligible to the total HXPS signal. On the contrary, the information from the near-surface area is quite prominent in the case of XPS. Finally, the signal from SXPS (the method with the lowest information depth) originates from the top surface.

The photoelectron spectroscopy measurements were carried out at various experimental stations, which are listed below.

2.2.1.1 XPS-TPR

XPS-TPR is an experimental station at the KFPP laboratories in Prague (the Czech Republic) for combined photoelectron spectroscopy and reaction experiments. It consists of an ultra-high vacuum chamber with a base pressure of around $5 \cdot 10^{-10}$ mbar. Fast entry of the samples is possible. The chamber was equipped with a dual-

anode Mg/Al Kα X-ray source, an Omicron EA 125 hemispherical electron energy analyser, an ion gun, a gas inlet system with simple molecular beams [54], a differentially pumped quadrupole mass spectrometer (QMS) Leybold Inficon 2000, and a sample holder enabling heating and cooling the sample in a temperature range 150–800 K. The temperature of the sample was checked by a K-type thermocouple attached to the side of the sample holder. During heating, the temperature increased linearly with a rate of 1 $K \cdot s^{-1}$.

The photoelectron spectra were acquired using the Al Kα X-ray source with the excitation energy of 1486.6 eV. The measurements were performed at normal emission of the photoelectrons with respect to the sample surface. The total resolution was approximately 1 eV.

2.2.1.2 MSB

Materials Science Beamline (MSB) is an experimental station managed by KFPP using the synchrotron radiation source Elettra in Trieste (Italy). The beamline is based on a plane grating monochromator providing narrow band synchrotron light in the energy range 21–1000 eV. The station consists of two ultra-high vacuum chambers, main and preparation, with base pressures of $\sim 10^{-10}$ mbar and $\sim 10^{-9}$ mbar, respectively. A fast entry of the samples is possible.

The main chamber is equipped with a Specs Phoibos 150 hemispherical electron analyser, a dual-anode Mg/Al Kα X-ray source, an ion gun, LEED optics, evaporators (Rh and Ce), a gas inlet, and a sample manipulator enabling precise positioning of the sample and heating and cooling in the temperature range 150–1300 K. The temperature is measured by a K-type thermocouple attached to the rear side of the sample. A preparation chamber can be equipped with various instruments, according to the nature of experiments. In our case, we installed a magnetron for Rh-CeO_x sputtering.

Due to the available photon energies and sufficient intensities, the MSB beamline is suitable for studying valence band and core levels close to the Fermi energy. Furthermore, it provides ideal conditions for the resonance photoelectron spectroscopy (RPES). The measurements using the synchrotron radiation are taken in a glancing incident and normal emission geometry. The total resolution depends on the energy of incident photons. It was estimated from a broadening of the Fermi edge on the cleaned Cu(111) single crystal to 160, 170, 400 and 690 meV for 45, 120, 420

and 630 eV, respectively. Deeper core levels (such as Ce 3*d*) were studied using the Al Kα X-ray source. In this case, the angle between the surface normal and an analyser axis was 20º. The total resolution was about 1 eV.

2.2.1.3 SuperESCA

SuperESCA is an experimental station at the Elettra synchrotron in Trieste (Italy) using an undulator light source providing photons of the energy range 90–1800 eV. The light is monochromatized by a planar grating monochromator and focused by an ellipsoidal mirror. The station consists of a main and a preparation chamber with base pressures of $1 \cdot 10^{-10}$ mbar and $1 \cdot 10^{-9}$ mbar, respectively. The main chamber contained LEED optics and an electron energy analyser PHOIBOS 150 – SPECS with a variable entrance slit. The total resolution was 150, 210, 335, 880 meV at photon energies of 115, 420, 650, 1256 eV, respectively. The preparation chamber was equipped with evaporators (Ce and Rh), a gas inlet system and an ion gun. The sample holder enabled heating the sample up to 1500 K. Temperature was controlled by a programmable PID controller. The fast entry of the samples was possible.

SuperESCA offers ideal conditions for studying the catalysts at elevated temperatures and in a reactive environment. The photoelectron spectroscopy measurements at higher pressures are possible due to a high intensity of the photoelectron signal and a small entrance slit of the analyser. Moreover, a high energy resolution enables studying small changes in chemical state of the system caused by the surface reactions or other treatment.

2.2.1.4 BL15XU

BL15XU is an experimental station at the Spring-8 synchrotron facility in Hyogo (Japan) managed by NIMS. It is an undulator beamline producing light in the energy range of 2–10 keV. During our experiments, the X-rays were monochromatized to 5950.2 eV using an Si 111 double monochromator and an Si 333 channel-cut post-monochromator. The experimental ultra-high vacuum chamber with a base pressure around $2 \cdot 10^{-9}$ mbar was equipped with a VG SCIENTA R4000 10 kV hemispherical analyser and a sample holder for several samples. Fast entry of the samples was possible. The measurements were performed in a glancing incident and normal emission geometry. The total resolution was approximately 250 meV.

2.2.1.5 HEAP Lab

The laboratory system HEAP Lab (Hard X-ray Photoelectron Spectrometer for laboratory use) is an off-line HXPS experimental station of the NIMS branch located at the SPring-8 synchrotron facility in Japan. The laboratory system consists of the ultra-high vacuum chamber with a base pressure of $2 \cdot 10^{-9}$ mbar equipped with a Cr Kα monochromatized X-ray source (5414.7 eV) and a VG SCIENTA R4000 10 kV hemispherical analyser with mesh-lens for a large acceptance-angle [55]. The measurements were taken at a glancing incident and normal emission geometry. The total resolution was approximately 530 meV. The station contains also a preparation chamber with a base pressure ~ 10^{-8} mbar. This chamber was equipped with a sample holder enabling heating samples in UHV conditions. The maximum achievable temperature was 600 K. Fast entry of the samples was possible.

The HEAP Lab system was used for investigating the thermal stability of the Rh-CeO_x films. Because of the high information depth of HXPS method, the experiments were focused on studying the interaction between the Rh-CeO_x films and the SiO_2/Si(100) substrate under thermal treatment. Two Rh(5%)-CeO_x samples were annealed in different conditions. The first one was annealed step by step in UHV conditions (in the preparation chamber). The second sample was annealed in air (in the ceramic high temperature oven). After every step of annealing, the state of the samples was checked by photoelectron spectroscopy.

2.2.2 Temperature programmed reactions

The catalytic activity towards CO oxidation was studied by temperature programmed reaction (TPR) at the XPS-TPR experimental station at KFPP laboratories. Steady-state TPR experiments consisted of several reaction cycles. Within one cycle, the sample was exposed to two molecular beams (CO, O_2) with constant intensities (about $5 \cdot 10^{12}$ molecules$\cdot$cm$^{-2}\cdot$s^{-1}). Simultaneously, it was heated from 300 K to 800 K with a rate of 1 K$\cdot$s^{-1}, and then cooled down to 300 K at approximately the same rate. The partial pressures of CO, O_2 and CO_2 were detected by the QMS during the entire cycle. The temperature was measured using a K-type thermocouple and registered simultaneously by an analogue port of the QMS.

In order to express the relative production of CO_2 to CO over the sample, a CO_2/CO parameter was calculated as a ratio of the total production of CO_2 to the total production of CO during one reaction cycle. The total productions of CO and

CO_2 during the reaction cycle were calculated as an integrated area under the reaction curve over time. It consists of molecules produced during the reactions, molecules desorbed from the surface or molecules from the molecular beam reflected at the surface. The signal from the residual atmosphere in the UHV chamber was subtracted from the reaction curves as a constant background.

The best way to evaluate the oxidizing ability of the sample would be the ratio of the CO_2 production to the amount of adsorbed CO molecules. However, the QMS signal originates from the reflected molecular beams, products of surface reactions as well as the molecules desorbing from the sample surface. We are not able to distinguish between these contributions and evaluate the number of adsorbed molecules on the surface of our samples. Therefore, we discuss the oxidizing ability of the samples in terms of the CO_2/CO parameter.

2.2.3 X-ray diffraction

The structure of thin films was checked by X-ray diffraction (XRD). This method is used to identify the crystal structure of the material. The incident X-ray photons diffract on the crystal planes into specific directions, forming a diffraction pattern. We can obtain the information about the symmetry of the crystal structure of the studied material from analysing the angles and intensities in the diffraction patterns.

XRD measurements were performed at the NIMS laboratories in Tsukuba (Japan), using the D8 DISCOVER Super Speed measurement system equipped with a 5 kW rotating anode Cu X-ray source (1.5406 Å). The measurements were conducted subsequently by a two-dimensional detector Bruker AXS and a scintillating detector working in a standard θ-2θ coupled mode. The size of CeO_2 crystallites in Rh-CeO_x and CeO_x thin films was estimated from the Sherrer formula [56]:

$$\tau = \frac{K\lambda}{\beta \cos\theta}, \qquad (2)$$

where β represents the peak broadening at half the maximum intensity (FWHM), λ is the wavelength of X-rays, and θ the Bragg diffraction angle. K refers to the shape factor which was put equal to 0.9. Because of a low intensity of the diffraction pattern, only the most intense CeO_2 *111* diffraction peak was used for estimating the size of cerium oxide crystallites.

2.2.4 Scanning electron microscopy

Scanning electron microscopy (SEM) is a powerful tool to determine a surface morphology of the solid state materials. The samples are irradiated by a focused beam of electrons which interact with the material. There are several ways how to characterize the material using different modes and detectors of the microscope. In the presented work, we used the secondary emitted electrons to obtain information about the morphology of the surface.

The cerium oxide thin films doped by rhodium were examined by Dr Stanislav Haviar using the HITACHI SU-70 field emission gun scanning electron microscope (FEG-SEM) at European Centre of Excellence (NTIS) in Pilsen (the Czech Republic). The SEM micrographs were acquired at the 30 keV acceleration voltage in the secondary electron mode and a working distance of 5.4 mm. The measurements were performed in a working pressure of $8 \cdot 10^{-6}$ mbar.

2.2.5 Density functional theory

Density functional theory (DFT) is a computational method developed for determining the electronic structure of many-body systems. The interaction between the rhodium adatom and the cerium oxide substrate was investigated by calculations based on the density functional theory. These were performed by Dr Lucie Szabová at NIMS in Tsukuba (Japan), similarly to the previously researched system of Cu/CeO_x [19, 38]. According to recent theoretical works [37, 39, 57, 58], a reliable description of both stoichiometric and reduced cerium oxide based materials can be achieved by employing the generalized gradient approximation (GGA) and adding a Hubbard *U* term to the GGA exchange functional to compensate the strong Coulomb repulsion among the localized Ce 4*f* electrons. The value of the parameter *U* used for the Rh/CeO_x systems was 4.5 eV. More details can be found in [38].

The (111) ceria surface (with or without the oxygen vacancy) was modelled by supercells consisting of three CeO_2 trilayers with the following sequence: O–Ce–O–O–Ce–O–O–Ce–O. Several adsorption configurations of rhodium adatoms were considered for stoichiometric and reduced cerium oxide surfaces. The bonding charge density analysis was performed for the most stable configuration at the CeO_2(111) surface and the surface containing the oxygen vacancy.

The bonding charge density analysis was performed by calculating the charge difference between the densities of the complete system, ρ_{Rh/CeO_x}, and the isolated noninteracting systems of a rhodium atom, ρ_{Rh}, and cerium oxide surface, ρ_{CeO_x}.

$$\Delta\rho = \rho_{Rh/CeO_x} - \left(\rho_{CeO_x} + \rho_{Rh}\right), \quad (3)$$

The adsorption energy of an Rh adatom on the CeO_x surface was calculated in terms of total energies of individual systems according to

$$E_{ads} = E_{Rh/CeO_x} - \left(E_{CeO_x} + E_{Rh}\right), \quad (4)$$

where E_{Rh/CeO_x} is the total energy of the complete system (rhodium adatom interacting with the cerium oxide surface), E_{CeO_x} is the total energy of the corresponding cerium oxide surface and E_{Rh} is the total energy of a rhodium atom isolated in vacuum.

2.3 Analysis of CeO_x photoelectron spectra

2.3.1 Core levels

Characterization of cerium oxide by means of photoelectron spectroscopy is a rather difficult task. Each Ce^{3+} and Ce^{4+} ions contribute to the spectra by separate structures. These are often quite complicated because of a multiple final state effect. In photoelectron spectroscopy, both initial and final states must be taken into consideration. Cerium oxide is usually described by a metal-ligand configuration even though the Ce–O bond has a high degree of covalency [59–61]. Following this notation, Ce^{3+} ions have the $4f^1$ configuration in a ground state. However, a ground state of Ce^{4+} in CeO_2 has been subject to a vigorous discussion. While some authors hold an opinion that Ce^{4+} has a mixed valency of $4f^0$and $4f^1$ in the ground state [62–65], the other authors reported that only the $4f^0$ configuration occurs [58, 66–68]. In the presented work, we follow a notation introduced by Pfau et al. [67], who based their conclusions on their high-resolution electron energy loss spectroscopy (HREELS) and photoelectron spectroscopy experiments.

According to this notation, Ce^{4+} has the $4f^0$ configuration in the ground state and three configurations of final states, $4f^0$, $4f^1$, and $4f^2$, while Ce^{3+} ions have two distinct final states, $4f^1$, and $4f^2$ [67]. These are summarized in Table 1 for a Ce 3*d* core hole. Ce 3*d* core level photoelectron spectra of cerium oxide with mixed valence

Ion	Initial state	Final state
Ce^{4+}	Ce $3d^{10}4f^{0}$	f^{0}: Ce $3d^{9}4f^{0}$ V^{n}
	Ce $3d^{10}4f^{0}$	f^{1}: Ce $3d^{9}4f^{1}$ V^{n-1}
	Ce $3d^{10}4f^{0}$	f^{2}: Ce $3d^{9}4f^{2}$ V^{n-2}
Ce^{3+}	Ce $3d^{10}4f^{1}$	f^{1}: Ce $3d^{9}4f^{1}$ V^{n}
	Ce $3d^{10}4f^{1}$	f^{2}: Ce $3d^{9}4f^{2}$ V^{n-1}

Table 1: Initial and final states of Ce^{4+} and Ce^{3+} ions in Ce 3*d* core level photoelectron spectra. *V* denotes the O 2*p* Ce 6*s*5*d*4*f* valence band, while *n* corresponds to the occupancy of the valence band.

(Ce^{3+} and Ce^{4+}) therefore consist of five singlets (*s* levels) or spin-orbit doublets (*p*, *d*, *f* levels). This is demonstrated in Figure 1 which shows Ce 3*d* photoelectron spectrum for $CeO_{1.87}$. The doublets corresponding to every final state are indicated by arrows.

A generally accepted though rather simplified idea of the multiple final state effect is that a creation of a core hole at a cerium core level through a photoemission results in a transfer of electrons from O 2*p* Ce 6*s*5*d*4*f* valence band to Ce 4*f* level, which drops below the Fermi energy due to the attractive force of the core hole [60, 67, 69]. Different final states have different screening ability of the positive core hole which influences the kinetic energy of the photoelectron resulting in energy shifts in the photoelectron spectra [60]. When the screening of the specific final state is more effective compared to others, the photoelectron core level peak can be shifted to lower binding energy.

Another effect complicating the analysis of the cerium oxide photoelectron spectra is multiplet-splitting. This type of splitting results from a coupling of the unpaired electron in a cerium core level created through the photoemission with an unpaired electron in the valence band, Ce $4f^{1}$ or $4f^{2}$ [66, 70]. The multiplet splitting is strongest when both involved levels are in the same shell (e.g. 4*f*–4*d*) [62]. The difference in the principal quantum numbers between the Ce 3*d* and Ce 4*f* levels reduces the effect of coupling on Ce 3*d* so that it causes only a broadening of the peaks in Ce 3*d* spectra [66]. On the other hand, the coupling is quite strong between Ce 4*d* and Ce 4*f* levels and additional peaks emerge in Ce 4*d* spectra. Moreover, a

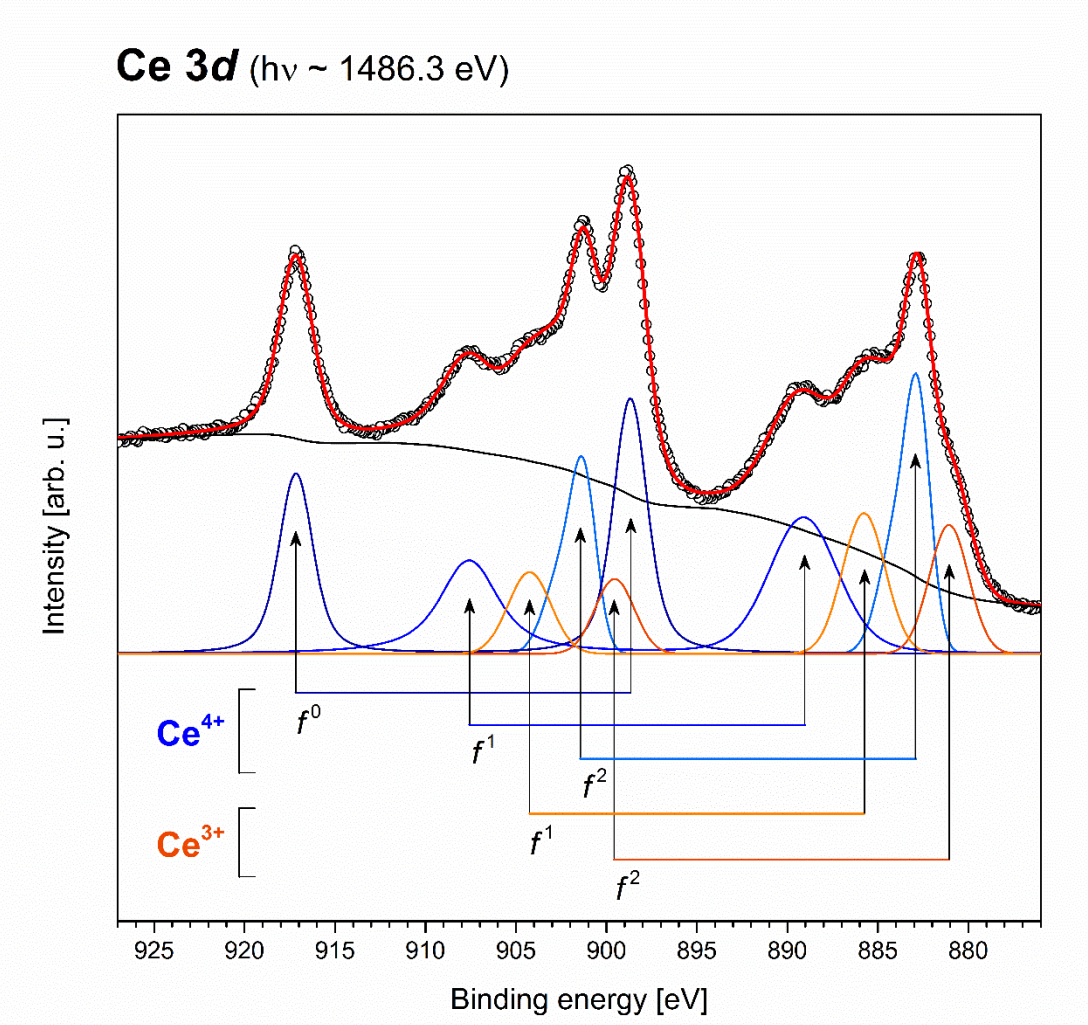

Figure 1: Ce 3*d* spectrum of a model cerium oxide thin film with the stoichiometry of $CeO_{1.87}$ (measured at MSB, Elettra, *hν* ~ 1486.3 eV)

magnitude of the multiplet splitting is similar to that of the spin-orbit splitting which makes it even more difficult to differentiate between the two effects [66].

The examples of Ce 4*d* spectra for cerium oxide with different content of Ce^{3+} and Ce^{4+} ions are plotted in Figure 2 (a). A red line corresponds to $CeO_{1.93}$ and a blue line to $CeO_{1.97}$. According to the literature, peaks W''' and X''' marked in Figure 2 (a) correspond to a spin-orbit doublet of Ce^{4+} with a Ce $4d^{9}4f^{0}$ final state [66, 71]. The remaining structure at a lower binding energy is a mixture of contributions from Ce^{4+} and Ce^{3+} ions with Ce $4d^{9}4f^{1}$ V^{n-1} and Ce $4d^{9}4f^{2}$ V^{n-2} final states, where *V* denotes the O 2*p* Ce 6*s*5*d*4*f* valence band and *n* the occupancy of the valence band. In order to distinguish between contributions from Ce^{4+} and Ce^{3+}, we subtracted the spectrum of $CeO_{1.97}$ from that of $CeO_{1.93}$. Beforehand, the spectra

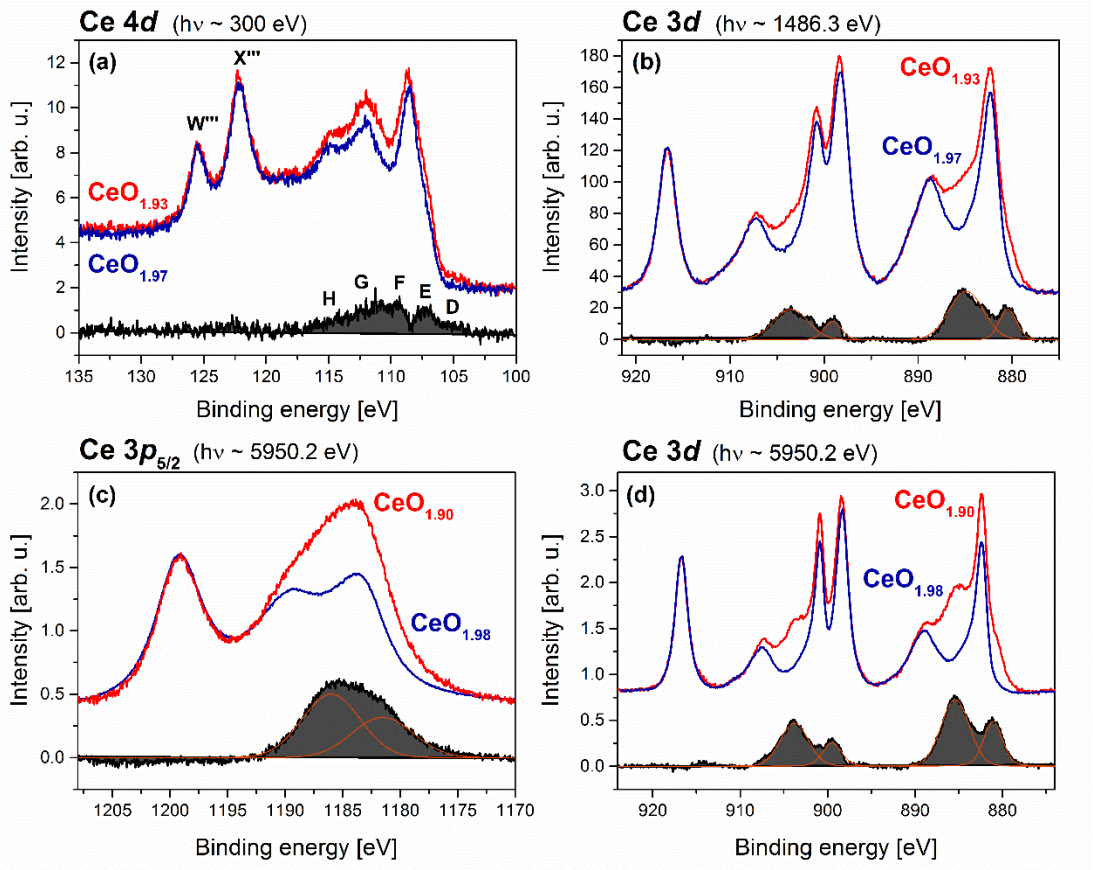

Figure 2: (a) Ce 4*d* photoelectron spectra measured at MSB, Elettra, using the photon energy of 300 eV; (b) Ce 3*d* core levels meaured at MSB, Elettra, using the photon energy of 1486.3 eV (Al Kα); (c) Ce $3p_{5/2}$, and (d) Ce 3*d* core levels meaured at BL15XU, Spring-8, using the photon energy of 5950.2 eV. Red and blue lines correspond to reduced and nearly stoichiometric cerium oxide, respectively. Black lines with filled area uner the curve are differences between the red and the blue lines.

were normalized to the intensity at 125.4 eV (only Ce^{4+} contribute to W'''). The difference spectrum is plotted at the bottom of Figure 2 (a) by a black line. It consists of contributions from Ce^{3+} only. According to the literature, there are at least five peaks, labelled as D–H [66], arising from spin-orbit and multiplet splitting of Ce 4*d* level. We can see that the peaks are not clearly distinguishable and the relative change between the spectra (red and blue) is very small even for a quite large change in the stoichiometry of CeO_x (1.93 and 1.97).

Figure 2 (b) shows Ce 3*d* spectra corresponding to that of Figure 2 (a) and their difference. Ce 3*d* spectra were normalized to the intensity at 916.7 eV corresponding to the Ce $3d^9 4f^0$ final state of Ce^{4+}. We can see that the change in the

spectra of $CeO_{1.97}$ and $CeO_{1.93}$ is much more prominent compared to the Ce 4*d* region. Also, there are only five doublets (due to the spin-orbit splitting) and their separation is considerably higher than in the case of Ce 4*d*, making peaks better resolved [62]. Generally, the separation of peaks in a spin-orbit doublet is higher in deeper core levels. It is 3.3 eV for Ce 4*d*, 18.5 eV for Ce 3*d*, and 87 eV for Ce 3*p*. From this point of view, we should be able to obtain better resolved spectra from the deeper core levels. Furthermore, there should be only very small influence of the multiplet-splitting effect on deeper core levels.

However, the situation is not that simple. According to Briggs et al. [70], the width of photoelectron peaks is determined by (i) the width of the excitation photon source, (ii) the analyser resolution and (iii) the natural linewidth of the core level which is a direct reflection of the lifetime of the core hole state resulting from the emission of the photoelectron under consideration. A core hole lifetime is governed by the processes that follow photoemission, through which the excess energy of the ion state decays. The core holes are filled by higher lying electrons, releasing their energy. Generally, deeper core holes have much shorter lifetime than core holes closer to the Fermi energy because there are more possible channels for de-excitation. Therefore, the core level photoelectron peaks at higher binding energies are broader and so, the analysis of the spectra is much less straightforward.

This is demonstrated in Figures 2 (c) and (d) which show the Ce $3p_{5/2}$ and Ce 3*d* regions, respectively. Ce 3*p* spectra were normalized to the intensity at 1199 eV corresponding to the Ce $3p^5 4f^0$ final state of Ce^{4+}. We can see that the peaks in the Ce $3p_{5/2}$ spectra are much broader than in the case of Ce 3*d*. The Ce $3p_{5/2}$ difference spectrum consisting of two peaks originating from Ce^{3+} is also unresolved, contrary to that of Ce 3*d*. Note that the spectra were obtained from measurements of $CeO_{1.90}$ and $CeO_{1.98}$ at BL15XU, Spring-8, which were performed under the same experimental conditions (incident photon energy: 5950.2 eV, constant passing energy: 200 eV, sample temperature: 300 K). The total resolution given by the experimental set-up (i–ii) was derived from a broadening of the Fermi edge on Au foil as 250 meV. Therefore, the difference between the Ce 3*p* and Ce 3*d* widths is given by the natural linewidths of the core levels only. We can see that this difference may be quite prominent. It is therefore necessary to choose carefully the best compromise between the peak widths and the magnitude of splitting.

Regarding all the effects described above, the Ce 3*d* spectra are most suitable for the analysis. In the present work, several different X-ray sources were used for the photoelectron spectroscopy measurement. In every case, we measured the Ce 3*d* region in order we could compare the results from all experiments.

2.3.2 Ce 3*d* core level

The analysis of the Ce 3*d* spectra is mainly focused on obtaining the concentrations of Ce^{3+} and Ce^{4+} ions in CeO_x. The concentration of the Ce^{n+} on can be derived from the Ce 3*d* spectra [67, 69], according to the equation:

$$Ce^{n+} = \frac{A(Ce^{n+})}{A(Ce)}, \tag{5}$$

where $A(Ce^{n+})$ denotes the sum of areas of the peaks originating from Ce^{n+} (obtained from the deconvolution of the spectra), and $A(Ce)$ is the total area of the Ce 3*d* spectrum after subtracting a background.

However, it is very difficult to obtain exact values of the cerium ions concentrations because a deconvolution of the Ce 3*d* spectra is a very demanding task. Small variations in fit parameters or a background have a great impact on a resulting fit. In the presented work, all spectra were fitted by identical procedures keeping a background and fitting parameters fixed as much as possible. By this way, even small changes in fitting results can give us meaningful information about changes in a sample composition. Because this work is focused on a comparison of various samples rather than a precise characterization of them, this approach seems to be sufficient.

Fitting was performed using the KolXPD software. Since the Ce 3*d* region is very wide, a composite background was used in our fitting procedure. Shirley background was combined with three ranged linear backgrounds (884–894 eV, 894–911 eV, and 911–925 eV) determining a slope of the background in particular regions. If a non-monochromatized X-ray source (Al Kα) was used for measuring cerium oxide thin films supported by copper substrate the satellites originating from Cu 2*p* were subtracted from Ce 3*d* region before the fitting. The spectra themselves were fitted by five doublets corresponding to five final states of Ce^{3+} and Ce^{4+} ions (see Table 1) according to the procedure described in [72]. All peaks were fitted using a Voight profile. The peaks of the Ce^{4+} f^2 doublet were fitted as a sum of two symmetric peaks [72, 73]. Relative positions of the peaks were kept fixed as well as

the ratio between peaks corresponding to particular doublets. The peak widths were allowed to vary moderately because the spectra obtained from measurement systems with different instrumental resolutions were analysed. The sample structure (e.g. polycrystalline, or amorphous) may also influence the peak widths.

An example of the fit of the Ce 3*d* spectrum is plotted in Figure 1. Three blue doublets correspond to Ce^{4+} and two orange doublets to Ce^{3+} ions. The concentration of Ce^{3+} ions in this sample was calculated from the equation (5) as ~0.25. The stoichiometry of cerium oxide is therefore $CeO_{1.87}$ following the equation:

$$x = 2 - \frac{Ce^{3+}}{2}, \tag{6}$$

where Ce^{3+} denotes the concentration of Ce^{3+} ions in CeO_x and x refers to a degree of reduction of cerium oxide ($1.5 < x < 2$).

2.3.3 Valence band

The information about the degree of reduction of cerium oxide can be obtained also from the valence band. The principal feature of the valence band photoelectron spectrum is a band that stretches from approximately 2 to 8 eV. It is demonstrated by black curves in Figure 3. This band corresponds to the emission from O 2*p* valence orbitals hybridized by Ce 5*d*4*f* due to an interaction between cerium and oxygen ions [59–61, 66–68]. Another significant feature of the spectra appears at the binding energy of approximately 1.5 eV (Figure 3, red curve). It was

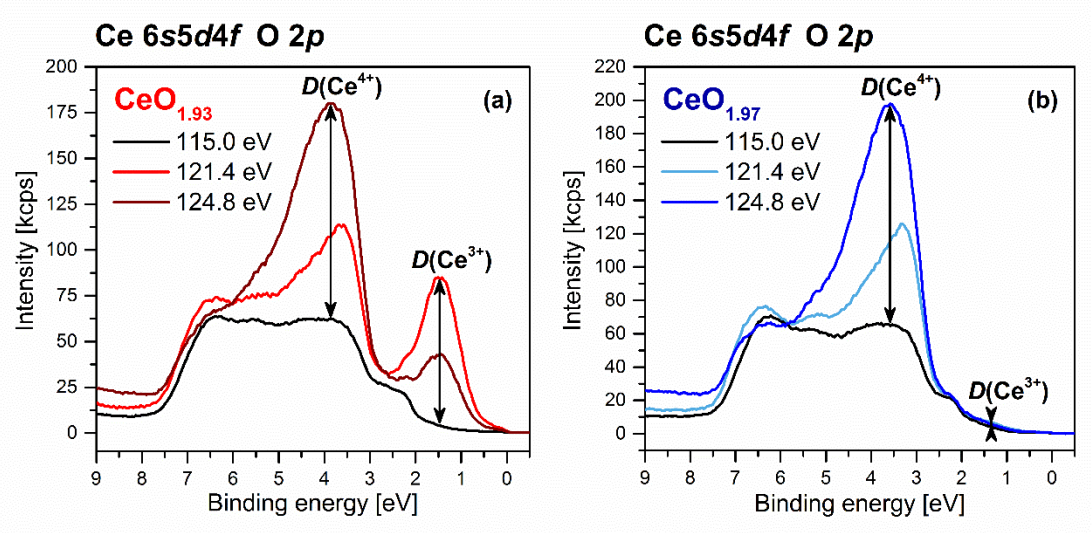

Figure 3: The on-resonance (121.4 eV – Ce^{3+}, 124.8 eV – Ce^{4+}) and off-resonance spectra (115.0 eV) for (a) $CeO_{1.93}$ and (b) $CeO_{1.97}$ measured at MSB, Elettra.

assigned to the emission from the localized Ce 4*f* orbitals. Because Ce^{3+} and Ce^{4+} ions have different occupancy of Ce 4*f* level, the intensity of the Ce 4*f* peak should give us information about the degree of cerium oxide reduction.

However, the intensity of the signal from the Ce 4*f* state is very weak when using standard X-ray sources because the photoemission cross-section from the Ce 4*f* level is considerably lower compared for example to that of O 2*p* [52]. One method how to probe the Ce 4*f* state is a resonant photoelectron spectroscopy (RPES). The resonance photoemission has been recently extensively utilized for extracting the partial density of 4*f* states in cerium oxide based materials [4, 74–79]. The 4*f* photoemission is resonantly enhanced when the incident photons have the exact energy to excite an electron from some core level to the 4*f* level. Most often, the 4*d*→4*f* photoexcitation is used. In that case, when the intermediate state reached by the excitation of 4*d* electron to the 4*f* level decays, the 4*f* electron filling back the 4*d* core hole may transfer the energy to other 4*f* electron and cause its emission [65, 74]. For Ce^{3+}, it can be described as

$$4d^{10}4f^{1} + h\nu \rightarrow 4d^{9}4f^{2} \rightarrow 4d^{10}4f^{0} + e, \qquad (7)$$

where *hν* and *e* stand for an incident photon and an ejected electron, respectively. The notation for the resonant photoemission from Ce^{4+} can be described due to the covalent character of the Ce–O bond as

$$4d^{10}4f^{0} + h\nu \rightarrow 4d^{9}4f^{1} \rightarrow 4d^{10}4f^{0}V^{n-1} + e, \qquad (8)$$

where V^{n-1} denotes the valence band deprived of one electron.

Figure 3 shows the resonant enhancement of the 4*f* photoemission at three different photon energies, 115.0, 121.4 and 124.8 eV, and for two samples, partially reduced CeO_x (a) and mostly stoichiometric CeO_2 (b). The energies of the maximal resonant enhancement were found experimentally, measuring the intensity of the 4*f* photoemission in dependence on the energy of exciting photons using a synchrotron light source [74, 75]. We can see from Figure 3 (a) that there are two resonant maxima. The maximum at approximately 1.5 eV correspond to the photoemission from Ce^{3+} ion and is more pronounced for more reduced CeO_x (a). The energy for this resonance is 121.4 eV. The other maximum appears at around 4 eV and it is a dominant feature in spectra of cerium oxide with a lower degree of reduction (b). It was measured using the energy of 124.8 eV and it was assigned to the photoemission

from the 4*f* state of Ce^{4+} [74]. The valence band spectra obtained at energies 121.4 and 124.8 eV are referred as the on-resonance spectra. In Figure 3, they are plotted by colourful lines. The 4*f* partial density of states can be obtained by subtracting an off-resonance spectrum from an on-resonance spectrum [65]. The off-resonance spectra are plotted by black lines in Figure 3. They were measured at 115.0 eV when no resonant enhancement of the 4*f* photoemission was detected. The differences between the on-resonance and off-resonance spectra, $D(Ce^{4+})$ and $D(Ce^{3+})$ are indicated by arrows.

Although the RPES is very sensitive to subtle changes in the 4*f* occupation, the stoichiometry of cerium oxide cannot be derived directly using this method [62]. In order to qualify a degree of reduction of cerium oxide and compare various samples, the resonance enhancement ratio (RER) is derived from the spectra as

$$RER = D(Ce^{3+})/D(Ce^{4+}). \quad (9)$$

2.3.4 Quantitative analysis

The photoelectron spectroscopy can be used for determining atomic concentrations of the components contained in the studied systems. A precise quantification of the photoelectron spectra is a very complex problem but for the purpose of the presented work, it is sufficient to use a simplified analysis. It is based on the assumption that the intensity of the signal from the element is proportional to its molar fractional content in the system. Because the yield of the photoemission varies significantly for different elements, core levels and energies of exciting photons, it is necessary to scale the intensities of the photoelectron spectra in order the variations in the peak areas would represent the amount of material in the system. Atomic factors of sensitivity, *s*, are used to scale the measured peak areas, *A*. Thus, the concentration *c* of the element *i* in the system containing *N* elements can be estimated as:

$$c_i = \frac{\frac{A_i}{s_i}}{\sum_j^N \frac{A_j}{s_j}}. \quad (10)$$

The atomic factors were derived empirically relative to F 1*s* (*s* = 1) for the most common energies of exciting photons (*hv* = 1486.6 eV for Al Kα, and *hv* = 1253.6 eV for Mg Kα) [80]. We used the following factors of sensitivity for

analysing the XPS spectra: 0.66 (O 1*s*), 4.10 (Rh 3*d*), 10.00 (Ce 3*d*), 4.95 (Au 4*f*), and 4.20 (Cu $2p_{3/2}$). Carbon was not included in the quantitative analysis. For different energies of exciting photons, the photoemission cross-sections were used for scaling the peak areas instead of the atomic factors of sensitivity [52].

This method gives relatively accurate results for homogeneous systems. The concentration of elements was estimated mostly for the thin films of doped cerium oxide prepared by radiofrequency magnetron sputtering which fulfil the condition of homogeneity very well. However, it is inapplicable for the systems with supported particles. In that case, we do not quantify the concentration of elements but we express the amount of deposited material through monolayers (ML). One monolayer represents the amount of the deposit equivalent to a monoatomic flat film of the deposit adsorbed on the substrate. It should be noted that the term of the monolayer refers only to the amount of the deposit but it does not imply anything about its morphology. The deposit can be either in a form of a monoatomic thin film, or three-dimensional particles.

If the deposit forms a flat continuous film, the thickness of the film can be estimated from an attenuation of the photoelectron signal from the support according to the equation

$$t = \lambda \cos(\vartheta) \ln\left(\frac{I_0}{I}\right). \qquad (11)$$

I_0 and I refer to the intensities of the photoelectron peaks originating from the substrate before and after the deposition, respectively. λ corresponds to the inelastic mean free path of an electron emitted from the substrate in the material of the deposit. ϑ marks the detection angle (the angle between the surface normal and the axis of the electron analyser). This method is very well applicable for estimating the thickness of the model cerium oxide thin films deposited *in situ* by evaporation in UHV conditions onto the Cu substrate. In that case, we use the attenuation of the Cu $2p_{3/2}$ peak and λ is put equal to 11.19 Å according to the QUASES-IMFP-TPP2M software based on the calculations of Tanuma et al. [53].

The formula (6) cannot be used when the deposit creates three-dimensional particles. In that case, we estimate the amount of the deposit experimentally using the quartz crystal.

3 Rh/CeO_x

In this chapter, we present the results of studying the system consisting of rhodium particles supported by thin films of cerium oxide. A special attention was paid to the interaction between the Rh particles and the substrate which depends strongly on the degree of CeO_x reduction. This interaction was investigated by means of the photoelectron spectroscopy. The measurements were carried out at the Materials Science Beamline at the synchrotron Elettra. We support our experimental results by calculations based on the density functional theory which were performed by Dr Lucie Szabová. A separate section is dedicated to the reactivity of the Rh/CeO_x system. We show that the interaction between cerium oxide and rhodium particles has a tremendous impact on the catalytic activity which was studied by the temperature programmed reactions focused on the CO oxidation. These experiments were carried out in the XPS-TPR laboratory at the Charles University in Prague.

3.1 Characterization of the interaction between Rh adatoms and CeO_x substrates

In order to thoroughly characterize the interaction between the rhodium deposit and the cerium oxide substrate, we prepared several model thin films of cerium oxide with different degrees of reduction. The preparation of the thin films is described in Section 2. The values of x in CeO_x varied from 1.98 to 1.67 with a higher degree of reduction. Figure 4 (a) shows the Ce 3*d* spectra for the films with the various degrees of reduction. The corresponding O 1*s* spectra are presented in Figure 4 (b).

We can see that the O 1s spectra consist of two peaks. The peak at the lower binding energy, O_{Lat}, can be assigned to oxygen from the ceria lattice [31, 47, 66, 75, 81, 82]. The peak at the higher binding energy is usually associated with OH groups adsorbed on the surface oxygen vacancies close to Ce^{3+} sites [66, 82–84]. The signs of hydroxyl groups are also apparent in the valence band spectra (data not shown). Water is a common component of the residual atmosphere in the UHV system. It does not adsorb on the stoichiometric CeO_2 but it readily fills the oxygen vacancies on the reduced cerium oxide surface. It agrees well with the increment of the OH peak intensity in the O 1*s* spectrum for the CeO_x films with lower x.

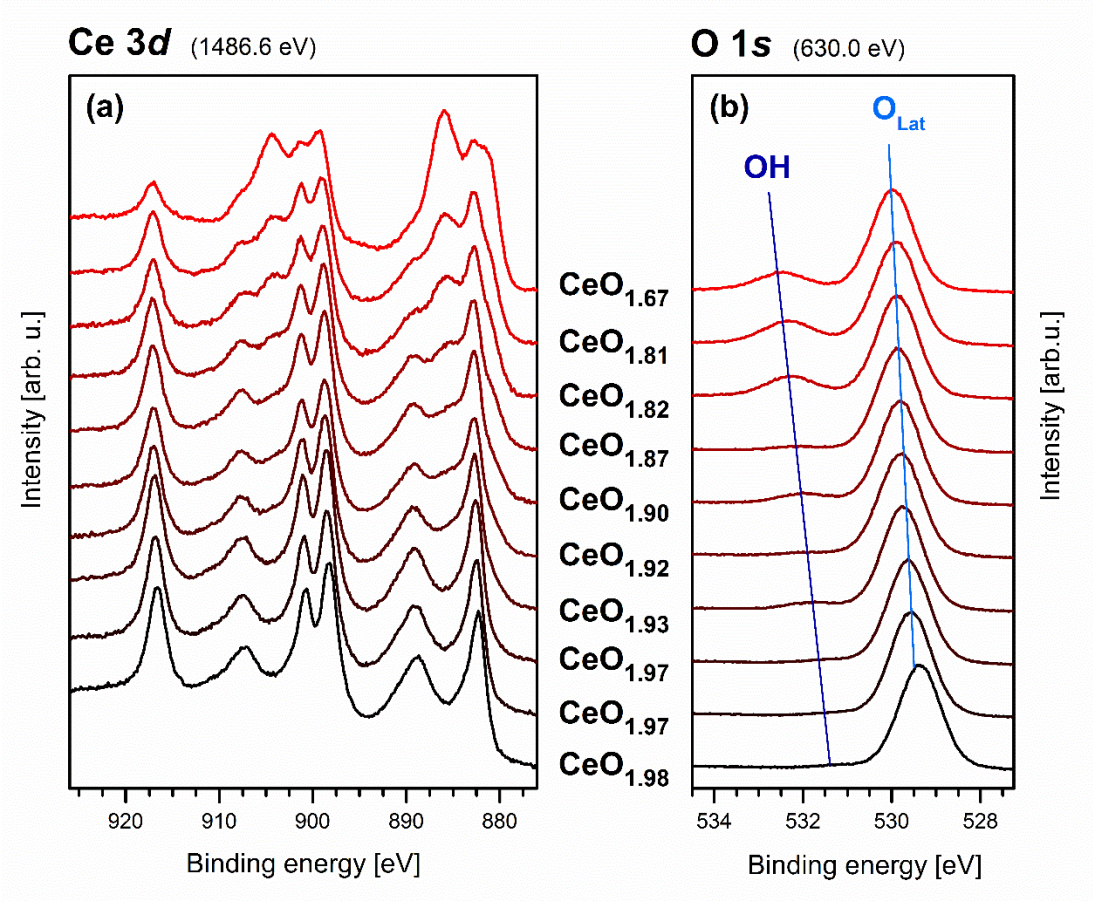

Figure 4: (a) the Ce 3*d* and (b) O 1*s* spectra of cerium oxide films with various degrees of reduction.

Furthermore, we can notice that the O 1*s* peaks shift to higher binding energies for lower *x*. The Ce 3*d* spectra in Figure 4 (a) and the valence band spectra (data not shown) exhibit the same shift. It is more apparent from Figure 5 which shows the binding energies of the Ce $3d_{3/2}$ (Ce^{4+} f^0), O_{Lat} and OH peaks designated in Figure 4. The maximum difference between the binding energies of oxidized $CeO_{1.98}$ and reduced $CeO_{1.67}$ is about 0.5 eV. The shift might be caused by different pinning of the Fermi energy due to changing the occupancy of Ce 4*f* states [39].

It is interesting that the distance between the Ce 3*d* and O 1*s* peaks remains same for all the CeO_x films. This result differs from the work of Duchoň et al. [31] who observed shortening of the distance between the Ce 3*d* and O 1*s* peaks for cerium oxide with the higher degrees of reduction. While Duchoň et al. worked with highly ordered CeO_x thin films with four different surface reconstructions [31], all our systems retained the surface reconstruction of (1.5 x 1.5) relative to the Cu(111)

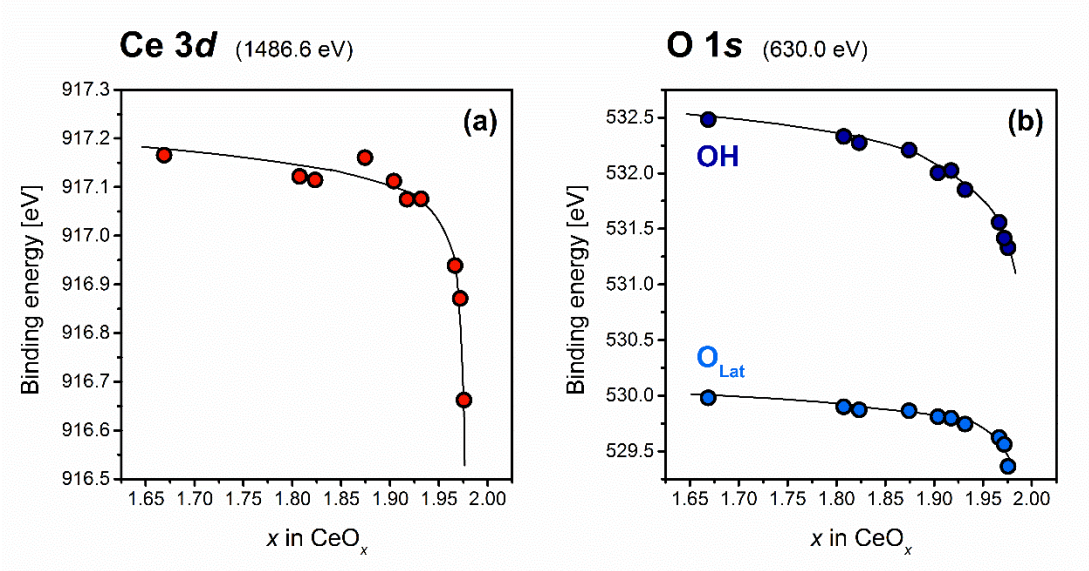

Figure 5: The binding energies of (a) Ce $3d_{3/2}$ (Ce^{4+} f^0) and (b) O 1*s* O_{Lat} and O_{Def} peaks.

substrate. Therefore, the discrepancy between our studied films and the published results might be caused by different morphologies of the films.

The interaction of rhodium and cerium oxide was studied by several consecutive depositions of rhodium onto the model CeO_x thin films. These films are described in more detail in Section 3.1. All depositions were performed *in situ* in the UHV conditions. The temperature of the substrates was approximately 300 K. After every deposition step, XPS and RPES measurements were performed to monitor the changes occurring in the samples.

Figure 6 shows the evolution of the degree of reduction during the deposition of rhodium onto various CeO_x substrates. The parameter *x* estimated from the XPS Ce 3*d* spectra according to the equation (6) is plotted in the graph (a). The resonance enhancement ratio derived from RPES measurements of the valence band at different energies of exciting photons is shown in the graph (b). Both of these parameters can be used independently for expressing the degree of reduction of cerium oxide.

We can see that the degree of reduction develops in two different ways. The films of nearly stoichiometric CeO_2 are reduced by deposited rhodium. On the contrary, CeO_x with lower *x* become more oxidized after adding rhodium. The boundary between these two trends is set by $CeO_{1.93}$ marked by turquoise stars. Both of these effects can be ascribed to the electronic metal-support interaction as is discussed in [46]. Because of the apparently different interactions between rhodium

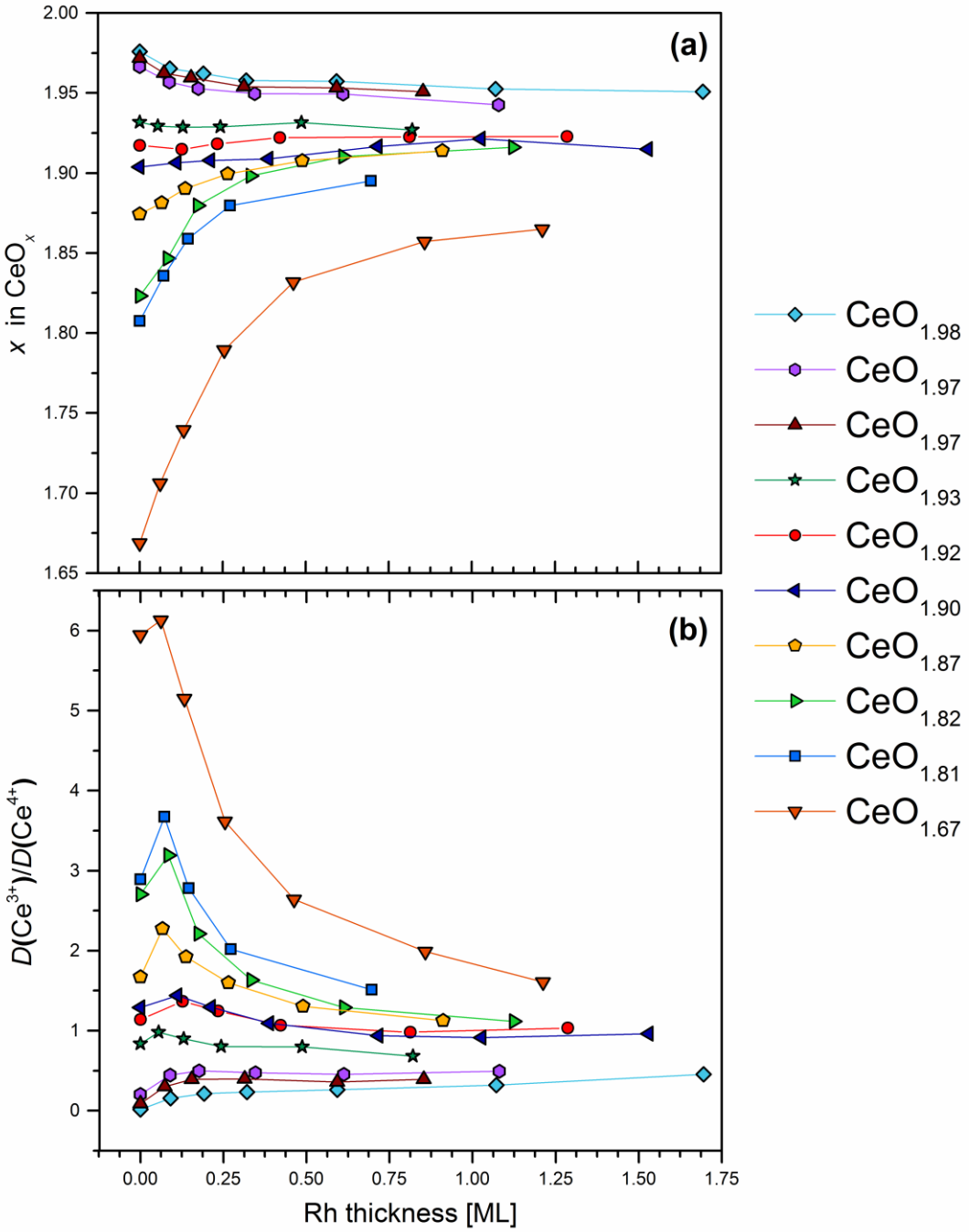

Figure 6: Evolution of the degree of reduction of cerium oxide with different stoichiometries (CeO_x) during the consequent deposition of rhodium obtained from (a) XPS and (b) RPES (measured at MSB, Elettra).

and oxidized or reduced cerium oxide, these two systems will be examined separately.

3.2 $1.93 < x < 2.00$

First, we will examine the interaction between rhodium and nearly stoichiometric CeO_2. The reduction of ceria by a deposited metal is a well-known effect which has been reported earlier for e.g. Pt/CeO_2 [4], Pd/CeO_2 [72], Au/CeO_2 [85], and Cu/CeO_2 [19] systems. In all cases, the reduction of cerium oxide was caused by an electron transfer from the deposited metal to the support, leading to the oxidation of the metal adatoms and the reduction of Ce^{4+} ions. According to Vayssilov et al. [4], the electron transfer from the metal cluster and the formation of Ce^{3+} is facilitated by a small energy difference between the highest occupied levels in the metal and the empty Ce 4*f* states of ceria. This view is corroborated for the $Rh/CeO_2(111)$ system by the work of Pfau et al. [86], who experimentally derived a nonzero overlap between the Rh 4*d* and Ce 4*f* orbitals. The charge transfer from Rh to CeO_2 has been also predicted by the density functional calculations of Lu et al. [18].

The changes in the electron structure of the Rh/CeO_x system due to the interaction between rhodium and nearly stoichiometric ceria are demonstrated on the $CeO_{1.98}$ sample. The total amount of rhodium deposited onto $CeO_{1.98}$ was approximately 2.8 ML. The valence band spectra for every step of the deposition and two photon energies are plotted in Figure 7. The photons with the energy of 45.0 eV have a high cross-section for exciting photoelectrons from Rh 4*d* states. Using this energy, the signal from rhodium is enhanced and the signal from cerium is

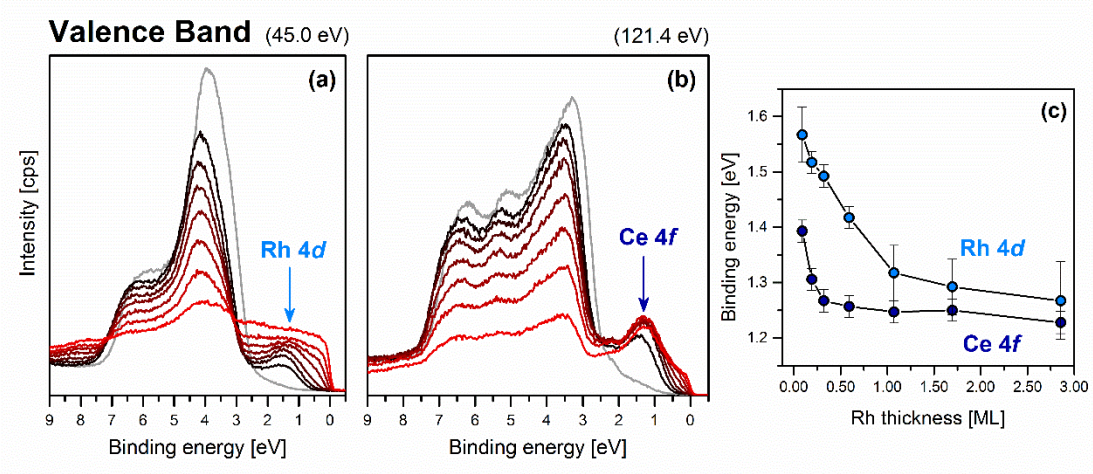

Figure 7: Evolution of the valence band spectra of $Rh/CeO_{1.98}$ during consecutive deposition of rhodium (from black to red) measured with energies (a) 45.0 eV, and (b) 121.4 eV. Grey lines mark $CeO_{1.98}$ before the deposition. Graph (c) shows the binding energy of the Rh 4*d* and Ce 4*f* maxima for every step of the deposition.

suppressed. On the other hand, the photon energy of 121.4 eV corresponds to the resonant electron emission from the 4*f* states of Ce^{3+} thus, highlighting the signal from Ce 4*f*. Figure 7 (c) shows the maxima of the Rh 4*d* and Ce 4*f* structures for every step of the deposition.

The main feature of the valence band spectra stretching from 2.5 to 7.5 eV corresponds to the O 2*p* valence orbitals. The Rh 4*d* and Ce 4*f* states are located around 1.5 eV. The maximum of the Rh 4*d* structure is at slightly higher binding energy than that of Ce 4*f*, as can be seen from Figure 7 (c), but both states clearly overlap. If we look at the spectra plotted in the graph (a) and (b), we can see that the most apparent change is the attenuation of the signal from O 2*p* caused by an increasing coverage of the surface by deposited rhodium. Besides, the maximum of the Rh 4*d* structure moves to lower binding energies with an increasing amount of deposited rhodium. The same shift was observed in the Rh 3*d* spectra (data not shown) and can be attributed to the particle-size effect. The particles exhibit a metallic character from approximately 1.7 ML judging from the formation of the Fermi edge in the valence band spectra.

Furthermore, we can see from the comparison of the grey and black lines in Figure 7 (b) that the Ce 4*f* intensity increases significantly after the first deposition of rhodium. It means that Ce^{4+} ions undergo the reduction by accepting electrons from the Rh adatoms. Figure 6 shows that the reduction of cerium ions proceeds with further deposition of rhodium. The reduction caused by a higher amount of deposited rhodium is less pronounced compared to the reduction induced by the first few steps of the deposition.

This is probably caused by a combination of two effects. Firstly, the less effective reduction of cerium can result from a relatively decreasing amount of rhodium atoms adsorbing directly onto the CeO_x substrate. According to Zhou et al. [87], rhodium grows three dimensionally on the cerium oxide support. It means that the relative amount of rhodium adatoms interacting directly with the substrate is decreasing with further addition of rhodium. Secondly, some of the Ce^{4+} ions accept electrons from rhodium during the first few steps of the deposition. Therefore, the area of stoichiometric CeO_2 diminishes not only because of the deposited rhodium but also because of the reduction of the substrate.

Our experimental results are supported by the calculations based on the density functional theory performed by Dr Lucie Szabová. The results derived from

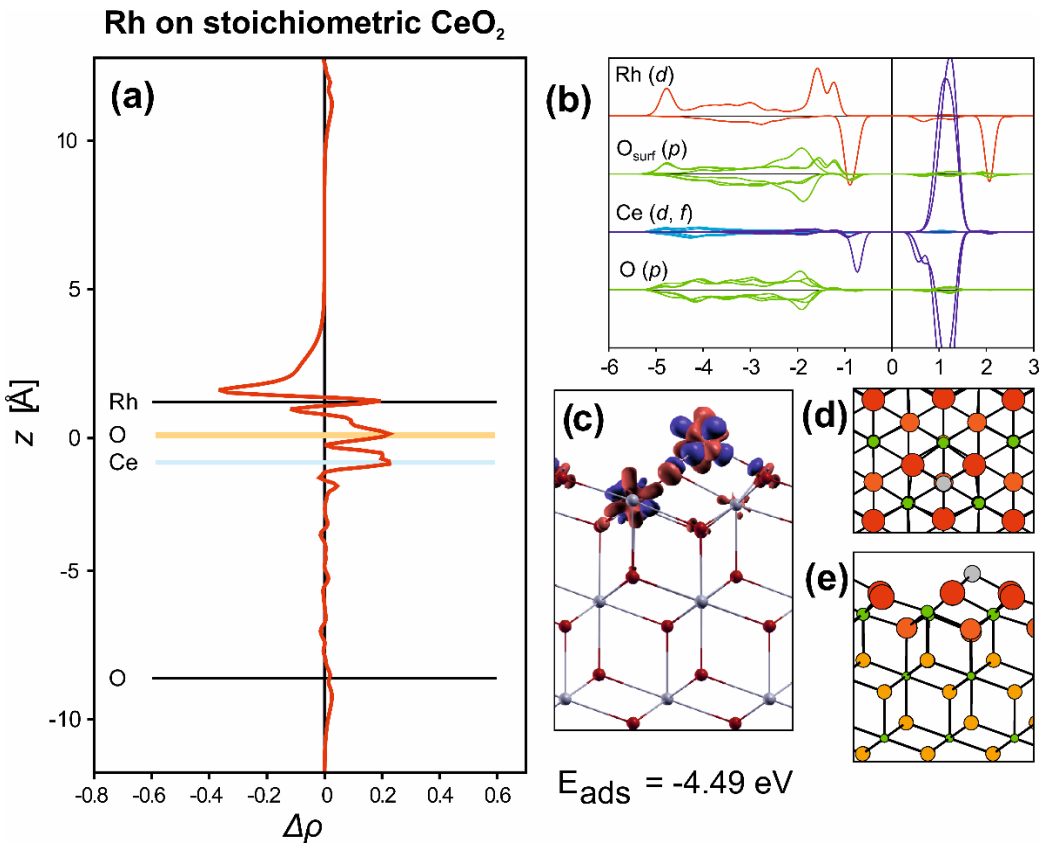

Figure 8: Results from the DFT calculations for an Rh adatom on the stoichiometric CeO_2(111) surface. (a) Change of bonding charge integrated in planes perpendicular to the surface plotted as a function of the height from the surface, (b) atom-resolved projected density of states, (c) an arrangement of the bonding charge· Electron accumulation and depletion are represented by red and blue areas, respectively. (d) Top view and (e) a side view of the most stable adsorption configuration of the Rh adatom on the CeO_2(111) surface (Rh – grey, Ce – green, O – orange, O in the first surface layer – red).

the calculations for the rhodium adatom adsorbed on the stoichiometric CeO_2(111) surface are demonstrated in Figure 8. The most stable adsorption configuration is displayed from a top view and a side view in parts (d) and (e), respectively. The rhodium adatom adsorbs into the hollow between three surface oxygen ions which agrees well with the results of Lu et al. [18]. The projected density of states for different atoms is plotted in Figure 8 (b). The energies are referred to the Fermi level. We can see that rhodium interacts with the surface oxygen and that the Ce 4*f* state accepts some electrons (judging from a peak in the occupied states). The bonding charge analysis displayed in Figure 8 shows the spatial distribution of the charge density difference (c) and the corresponding integrated values on planes parallel to the surface (a). The charge transfer from rhodium to cerium oxide is evident from the

graph (a) showing the depletion of the charge density on rhodium and the accumulation of the charge density on cerium and oxygen ions. The surface oxygen and cerium ions close to the Rh adatom are involved in the charge transfer (see the panel (c)).

3.3 $1.67 < x < 1.93$

The situation is different for rhodium adsorbed on reduced cerium oxide. Figure 6 shows that the deposition of rhodium induces the oxidation of cerium for oxides with the high degree of reduction. The oxidation of an oxide support upon the deposition of a metal is rather unusual. Therefore, we first considered the interaction of the reduced oxide with the residual atmosphere in the UHV system.

Molecular oxygen is not present in the residual atmosphere of the UHV system because of its high reactivity. The atmosphere in the MSB chamber was composed mainly from argon (originated from ion sputtering), hydrogen and carbon dioxide. While argon is completely inert and hydrogen causes the reduction of ceria [88], it was reported that the exposure of the reduced cerium oxide to CO_2 leads to its oxidation [89]. However, the decomposition of CO_2 molecules accompanied by the oxidation of cerium ions also leads to the formation of the surface carbonates and carboxylates. There were no traces of these species in the C 1*s* spectra at our samples. Furthermore, a small amount of water is usually present in the UHV chamber. This either would not cause any detectable oxidation of reduced cerium

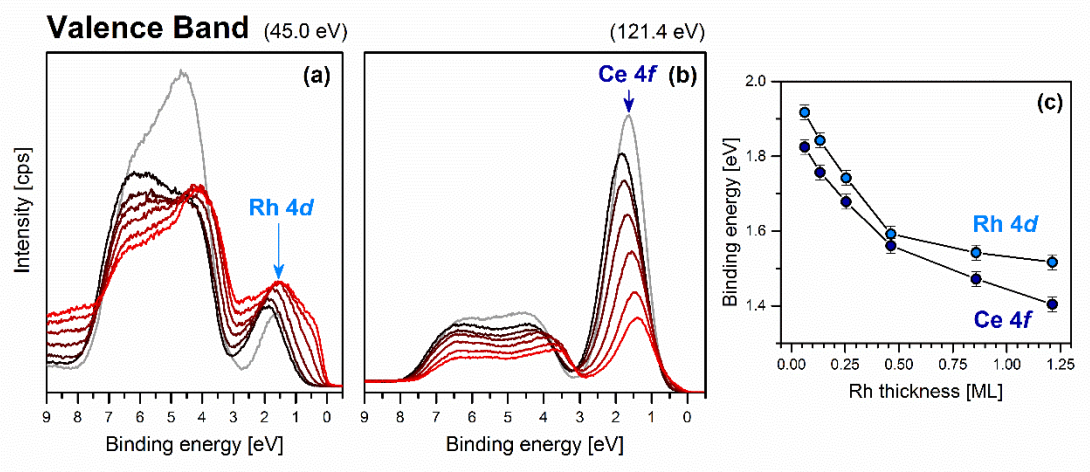

Figure 9: Evolution of the valence band spectra of $Rh/CeO_{1.67}$ during consecutive deposition of rhodium (from black to red) measured with energies (a) 45.0 eV, and (b) 121.4 eV. Grey lines mark $CeO_{1.67}$ before the deposition. Graph (c) shows the binding energy of the Rh 4*d* and Ce 4*f* maxima for every step of the deposition.

oxide at the temperature of 300 K [84, 90]. Therefore, the oxidation induced by adsorbates from the residual atmosphere can be ruled out.

Another way how the surface of reduced cerium oxide can be oxidized is a transport of oxygen from deeper layers towards the surface. The degree of reduction of our model thin films is not uniform. The surface contains more Ce^{3+} ions compared to the deeper layer [31]. The migration of oxygen through cerium oxide is a well-known effect [13]. However, it does not play an important role during Rh deposition at the room temperature because the extent of oxygen migration at 300 K is very low. Besides, we did not observe any significant changes in the O 1*s* spectra (data not shown). Moreover, we observed the oxidation at both, the near surface area (RPES) and the deeper layers (XPS) which goes against the transport of oxygen ions from deeper layers to the surface.

Therefore, the oxidation of reduced cerium oxide has to be induced by the interaction with rhodium, similarly to Cu/CeO_2 [19] and Au/TiO_2 [91, 92] systems. The nature of this interaction is also the electronic metal-support interaction but it is different from that for the Rh/CeO_x samples with the lower degree of reduction. The nearly stoichiometric cerium oxide thin films are terminated with O^{2-} layer (see Figure 8 (a)) while the partially reduced cerium oxide surface contains exposed Ce^{3+} ions. Rhodium can thus interact directly with cerium ions (Rh-Ce), unlike in the case of stoichiometric cerium oxide where Rh and Ce are separated by an oxygen layer (Rh-O-Ce).

The Rh-Ce interaction is evident from our measurement of the valence band region for the Rh/CeO_x samples with the high degree of reduction. The surfaces of such samples contain a high amount of oxygen vacancies and the electron rich Ce^{3+} sites in their vicinity. The valence band spectra for every deposition step onto the sample $CeO_{1.67}$ are plotted in Figure 9. The total amount of deposited rhodium reached approximately 1.2 ML. The interaction between the Ce and Rh atoms induces partial transfer of the electron density from Ce 4*f* to the Rh 4*d* state. The decreasing occupancy of Ce 4*f* state can be clearly seen from Figure 9 (b). The charge transfer from Ce^{3+} to Rh results in a build-up of a negative charge on rhodium. Mullins and Overbury hypothesized that Rh particles could withdraw a charge from relatively electron rich Ce^{3+} sites [27], making Rh slightly anionic on the reduced substrate. This assumption complies with the DFT calculations performed by Dr Lucie Szabová.

Figure 10 shows the results from the DFT calculations for an Rh adatom adsorbed in an oxygen vacancy on the reduced CeO_x(111) surface. The panels (d) and (e) demonstrate the most stable adsorption configuration. We can see that the rhodium atom sits in the oxygen vacancy site, slightly above the position of the original oxygen ion. It is bonded to the nearest oxygen and two closest cerium ions. The projected density of states plotted in the graph (b) clearly shows that the electronic structure of the Rh/CeO_x system is different compared to the Rh/CeO_2 (see Figure 8 (b)). Furthermore, we can see from the bonding charge density analysis displayed in panels (a) and (b) that the charge transfers from cerium ions to rhodium, oppositely to Rh/CeO_2. These calculations brought the evidence about the electronic metal-support interaction on the Rh/CeO_x system which was suggested in [46].

An interesting effect which can be noticed in Figure 6 (b) for reduced CeO_x is

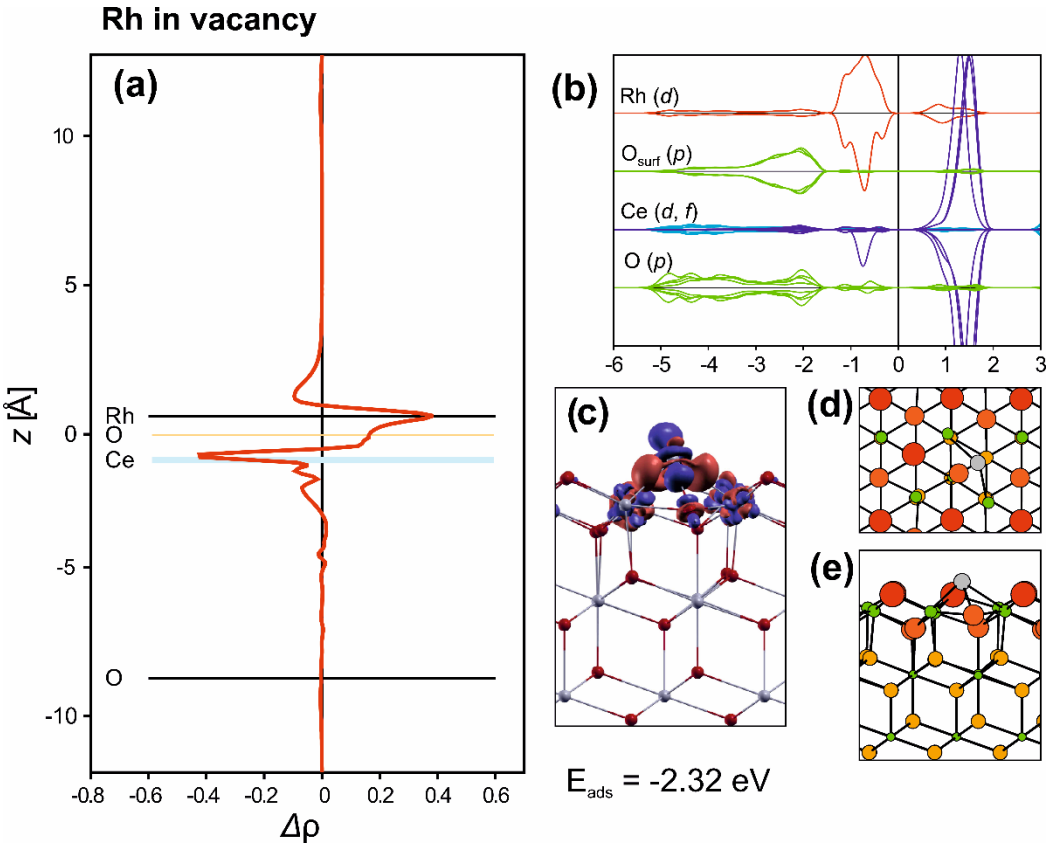

Figure 10: Results from the DFT calculations for an Rh adatom adsorbed on an oxygen vacancy in the reduced CeO_x(111) surface. (a) Change of bonding charge integrated in planes perpendicular to the surface plotted as a function of the height from the surface, (b) atom-resolved projected density of states (DOS), (c) a three-dimensional arrangement of the bonding charge· Electron accumulation and depletion are represented by red and blue areas, respectively. (d) Top view and (e) a side view of the most stable adsorption configuration of the Rh adatom on the CeO_x surface (Rh – grey, Ce – green, O – orange, O in the first surface layer – red).

an increase of the degree of reduction after the first deposition of rhodium. Further deposition results in the oxidation of cerium oxide described above. The initial reduction may be caused by a preferential adsorption of rhodium adatoms on the stoichiometric CeO_2 surface instead of the oxygen vacancy sites. The adsorption energy of rhodium on the stoichiometric CeO_2 surface is about twice higher compared to that of reduced cerium oxide. Rhodium atoms migrate readily over the cerium oxide surface even at the room temperature [87]. Therefore, the oxygen vacancies are occupied by rhodium only if there is no available area of stoichiometric CeO_2 in the vicinity of the adatom. When these positions are saturated, rhodium adsorbs on the oxygen vacancy sites which results in the oxidation of cerium oxide.

3.4 Reactivity of Rh/CeO_x

The reaction experiments were focused on the CO oxidation reaction because it is a very simple reaction suitable for probing the catalytic activity of the studied systems. We compare the reactivity of two samples marked as Rh/$CeO_x^{(Ox)}$ and Rh/$CeO_x^{(Red)}$ which differ from each other by the degree of reduction of the CeO_x substrate before the deposition of rhodium. The stoichiometry of cerium oxide before the deposition was $CeO_{1.94}$ and $CeO_{1.85}$ for (Ox) and (Red), respectively. Therefore, both samples exhibit different metal-substrate interactions (see Sections 3.2 and 3.3). The amount of deposited rhodium was approximately 1 ML on both samples.

It should be noted that the thin films of cerium oxide used in the TPR study were deposited by magnetron sputtering onto the SiO_2 substrate because these films are less vulnerable to sintering at higher temperatures. Moreover, the OSC of the sputtered films is much higher than that of the model systems presented in Section 3.1. This disparity is caused by different morphologies of the Rh-CeO_x films. While the model thin film is formed by large and flat highly oriented ceria structures epitaxially grown on the Cu(111) surface [93], the sputtered films are composed of small crystallites. According to Migani et al. [28], the formation of oxygen vacancies in ceria nanocrystallites is greatly facilitated compared to extended surfaces. Therefore, the effects caused by oxygen migration between the particles and substrate would be significantly enhanced and more easily observable compared to the model systems.

Figure 11 demonstrates the CO oxidation under the steady-state reaction conditions for $Rh/CeO_x^{(Ox)}$ and $Rh/CeO_x^{(Red)}$ samples as well as the reference Rh foil and pure CeO_x with the low degree of reduction. All samples were simultaneously exposed to molecular beams of CO and O_2 in a ratio of 1:1. All reactants and products of reactions were monitored between 300 and 800 K during the linear increase of the temperature (Figure 11, left) and cooling down (Figure 11, right). These two parts of Figure 11 are separated by a dotted line. CO_2 production curves are displayed by black lines, CO and O_2 are coloured by red and blue, respectively.

If we look at the TPR curves of pure cerium oxide (d) there is no production of CO_2. It means that cerium oxide does not react with CO under these experimental conditions. Comparing the $Rh/CeO_x^{(Ox)}$ and $Rh/CeO_x^{(Red)}$ samples we can see that there are two distinct maxima of the CO_2 production common for both samples, (i) and (ii). Similar features can be found in the CO_2 curves of pure rhodium. It suggests that the peaks (i) and (ii) originate from the CO oxidation on rhodium particles. Furthermore, another peak emerges around the break point between heating and cooling of the sample $Rh/CeO_x^{(Ox)}$. It is marked as (iii). Similar feature cannot be found at any other reaction curve. It means that the reaction path leading to CO oxidation at high temperatures is available only at $Rh/CeO_x^{(Ox)}$.

The spillover (molecular transfer from the particle to the support) and the reverse spillover (molecular transfer from the support to the particle) of oxygen occur at the Rh/CeO_x systems at higher temperatures. Therefore, the cerium oxide substrate can act as an oxygen buffer layer. However, the transport of oxygen between the particle and the support is strongly influenced by the electronic metal-substrate interaction [46]. More details about this topic can be found in Appendix B. For the purpose of this work, it is sufficient to summarize that the transport of oxygen is allowed for the $Rh/CeO_x^{(Ox)}$ systems, but it is suppressed for $Rh/CeO_x^{(Red)}$. This explains the difference in the reaction curves of both systems. Furthermore, it demonstrates the importance of the electronic metal-support interaction and its impact on the reactivity of the catalyst.

The reaction mechanism of the CO oxidation under steady-state reaction conditions on Rh/CeO_x system was previously described in [94]. The maxima (i) and (ii) for $Rh/CeO_x^{(Ox)}$ and $Rh/CeO_x^{(Red)}$ can be assigned to the $CO_{ads} + O_{ads} \rightarrow CO_2$ reaction where both reactants are adsorbed on the surface of rhodium particles. It was

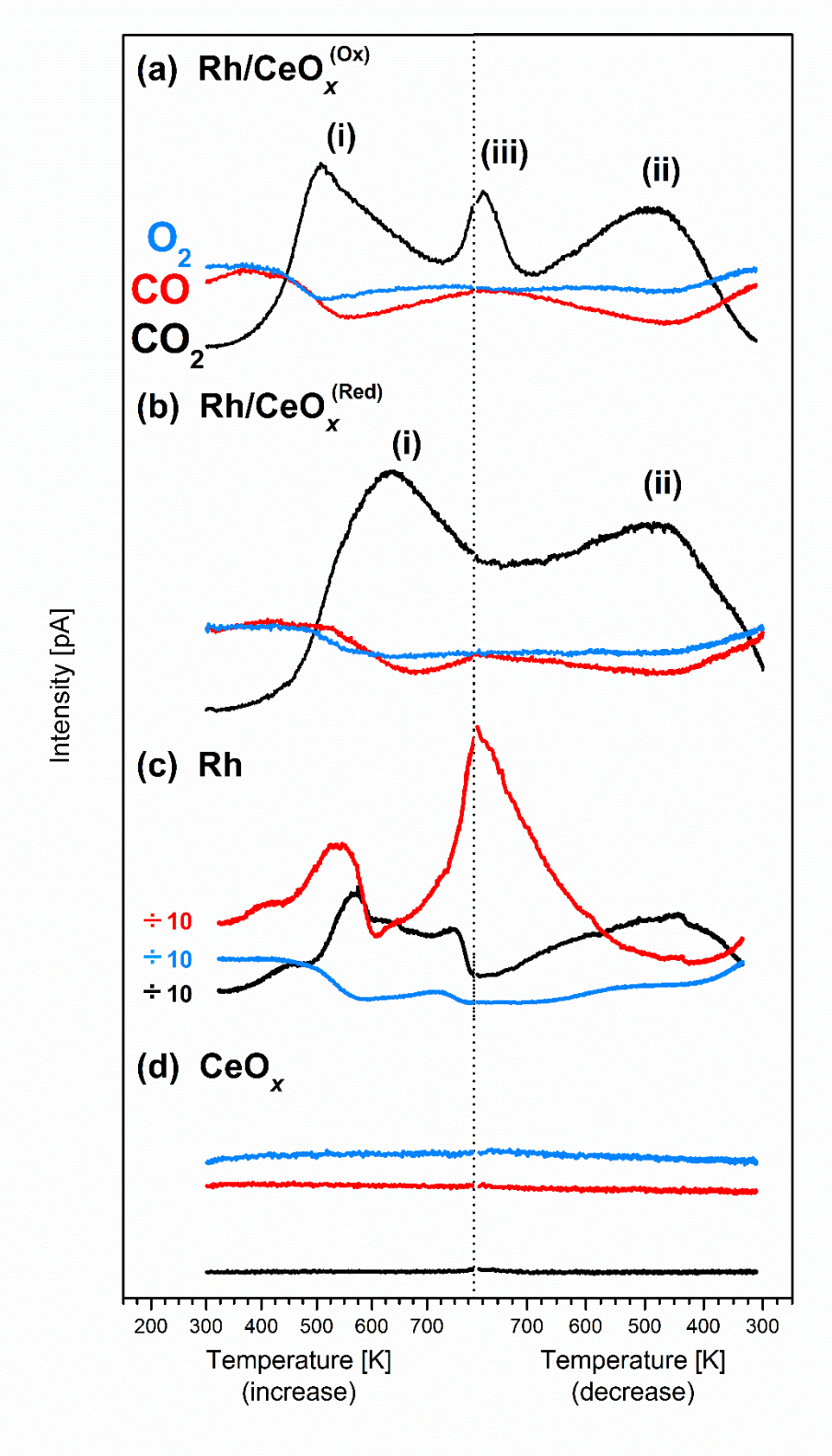

Figure 11: Comparison of CO_2 production (black), and CO (red) and O_2 (blue) consumptions during steady-state reactions on (a) Rh/$CeO_x^{(Ox)}$, (b) Rh/$CeO_x^{(Red)}$, (c) the Rh foil and (d) the CeO_x thin films.

experimentally verified that carbon monoxide adsorb on rhodium but not on cerium

oxide. Oxygen, on the other hand, can come either from the molecular beam, or the substrate. Because both reactants can be adsorbed only on the Rh particles, that is the only available place for the reaction.

The strength of the CO–metal bond determines the energy of the desorption which is very important for the CO_2 production on Rh/CeO_x. Because of the nature of the experiment (several consecutive reaction cycles), we assume that the surface of the rhodium particles is covered by CO at the beginning of the reaction [46, 94]. CO inhibits adsorption positions for oxygen on rhodium [95, 96]. The CO_2 production is very low at temperatures below 400 K because there is no available source of oxygen (the oxygen cannot adsorb on rhodium from the molecular beam due to CO and the reverse spillover is negligible at low temperatures). The reaction starts when the sample is heated sufficiently, enabling the CO desorption. After CO leaves the surface, the liberated positions may be filled by oxygen which can oxidize neighbouring CO molecules. The temperature necessary for the CO desorption is about 450 and 500 K at $Rh/CeO_x^{(Ox)}$ and $Rh/CeO_x^{(Red)}$, respectively [46]. It agrees with the onset of the CO_2 production in Figures 11 (a) and (b).

With a further increment of the temperature, the time of CO residing on rhodium gradually decreases. When it becomes shorter than the time needed for the formation of CO_2, the CO oxidation ceases. To some extent, oxygen can adsorb on the sample surface even at high temperatures (see Figure 11). At elevated temperatures, oxygen can migrate to rhodium from the cerium oxide support quite easily. Therefore, the surface of rhodium particles is partially covered by oxygen atoms at high temperatures.

We can notice from the right part of Figure 11 that the maximum (ii) is on the same temperature for both, $Rh/CeO_x^{(Ox)}$ and $Rh/CeO_x^{(Red)}$. This is different from the case of the maximum (i). The explanation is however very simple. The reaction during cooling the sample is the same as during heating ($CO_{ads} + O_{ads} \rightarrow CO_2$) but the state of the surface is different. As was stated above, the Rh surface is saturated by CO at the beginning of the reaction cycle, when the temperature starts to increase. On the other hand, when the cooling of the sample starts, the surface is covered by oxygen. Because oxygen does not block the adsorption of carbon monoxide on rhodium [95], the reaction can start when the temperature is low enough to allow CO

staying at the surface long enough to react with oxygen. Our experiments suggest that this adsorption is not influenced by the electronic metal-support interaction.

Now, we discuss the peak (iii) formed on $Rh/CeO_x^{(Ox)}$ around the break point between heating and cooling at 800 K. Since the rapid increase of the CO_2 production is above 750 K, the CO oxidation can no longer be described by the reaction of adsorbed CO_{ads} on the surface of the Rh particles. A plausible explanation for the CO_2 production above 750 K would be that the CO molecules impinging the surface react with the oxygen atoms adsorbed on the Rh particles, $CO + O_{ads} \rightarrow CO_2$. The oxygen is supplied by the cerium oxide support via the reverse spillover because the amount of oxygen provided from the molecular beam is not sufficient (judging from the absence of the CO_2 peak above 750 K in Figure 11 (c) corresponding to the Rh foil). Figure 11 shows that this reaction occurs only on the $Rh/CeO_x^{(Ox)}$ system. We cannot find the peak (iii) on the sample $Rh/CeO_x^{(Red)}$. This is because the transport of oxygen between rhodium and cerium oxide is suppressed when the rhodium particle has a net negative charge due to the electronic metal-substrate interaction. Further details can be found in Appendix B.

Within this chapter, we demonstrated that the electronic metal-substrate interaction between rhodium and cerium oxide has a tremendous impact on the reactivity of the system. It is a very important result which could help designing catalyst systems with desired properties.

4 Rh-CeO_x

This chapter focuses on the doped cerium oxide thin films. We discuss the effect of enriching cerium oxide by various dopants, such as Au, Cu, Si and F. A special attention was paid to the Rh dopant. First, we characterize the chemical composition and morphology of cerium oxide thin films with various concentrations of rhodium. The films were studied by means of the photoelectron spectroscopy, X-ray diffraction and scanning electron microscopy. The photoelectron spectroscopy experiments were performed at HEAP-Lab at NIMS (HXPS), BL15XU at SPring-8 (HXPS), MSB and SuperESCA at Elettra (XPS, SXPS, UPS and RPES), and the XPS-TPR laboratory at KFPP (XPS). The X-ray diffraction measurements were carried out at NIMS. Microscopy imaging was performed by Dr Stanislav Haviar at NTIS. A separate chapter is dedicated to a thermal stability of the Rh-CeO_x films. The influence of the environmental atmosphere, the film-substrate interaction and surface adsorbates are discussed. Finally, we present the study of the Rh-CeO_x reactivity which was investigated by means of the temperature programmed reactions at the XPS-TPR laboratory at KFPP.

4.1 Effect of dopants on CeO_x

The interaction of a small metal particle with an oxide surface can result in significant modifications of the electronic structure of the supported species. In particular, charge can flow from the surface to the supported metal or oppositely, from the particle to the substrate. This charge transfer may cause significant changes in the chemical and catalytic properties of the particles. This is the basis for the electronic metal-support interaction [14]. As the size of the deposited metal increases, it is expected that the particles reach chemical and structural properties typical for the corresponding metal, and the effect of the supporting oxide is strongly reduced. But if the particle size decreases, down to the single atoms, the interaction with the substrate may result in major modifications of the electronic structure and catalytic activity of the supported species.

The limit case is that the supported metal is atomically dispersed over the surface of the oxide. It was reported that traces of atomically dispersed gold, or platinum can be found at the cerium oxide surface and that these species are

responsible for the high catalytic activity of the system [97]. A recent experimental and theoretical combined study of the Pt/CeO_2 system helped explaining the origin and unique properties of atomically dispersed platinum over ceria [3]. There are special sites at the CeO_2 surface, so called ceria "nanopockets", which bind Pt^{2+} ions so strongly that they can withstand sintering or bulk diffusion even at higher temperatures. However, a number of these special positions is limited according to the morphology of the ceria surface. There are much fewer available sites at flat surfaces compared to rough surfaces of nanoparticles. If all available positions are saturated, any additional platinum forms larger particles of Pt^0 [3].

In general, it is very difficult to reach the atomic dispersion for metals such as Cu, Au, Pd, Pt or Rh at the surface of cerium oxide because these metals tend to grow in three-dimensional particles and coalesce at higher temperature [38, 45, 87]. Although some special positions may stabilize single metal atoms as in the case of platinum, this is not generally applicable.

A way how to easily achieve an atomic dispersion of metal species is doping a supporting material by the corresponding metal [32, 33, 35, 98, 99]. Recently, very good results were obtained by depositing thin films by radio frequency magnetron sputtering from targets composed of the metal and the support materials, cerium oxide [34, 43, 81, 100, 101]. These films are in a form of a solid solution with ions of the dopant incorporated in the host oxide [11, 81, 100, 102]. Metal ions substitute Ce^{4+} ions and their repulsive charge prevents them from sintering into particles and help to preserve the high dispersion [98]. Dopants substituting cerium usually do not reduce cerium ions directly [37–39] but they disrupt chemical bonds in the host oxide causing significant modifications in a near environment, which may result in a high amount of defects in the cerium oxide lattice [6, 39]. The defective areas have a high concentration of Ce^{3+} ions and oxygen vacancies because their formation releases the strain in the oxide [32, 47, 50]. Furthermore, if the valency of the dopant is lower than that of the host oxide cation (Ce^{4+}), oxygen vacancies are formed to maintain the charge neutrality of the system [15]. Therefore, Ce^{3+} ions in doped cerium oxide can be related to structural defects in cerium oxide caused by the dopants, rather than a direct interaction between cerium and dopant ions and a manifestation of the mixed oxide phase.

The examples the Ce 3*d* spectra of cerium oxide doped by a low-valency metal are shown in Figure 12. The $Au\text{-}CeO_x/C/SiO_2$ or $Cu\text{-}CeO_x/SiO_2$ thin films

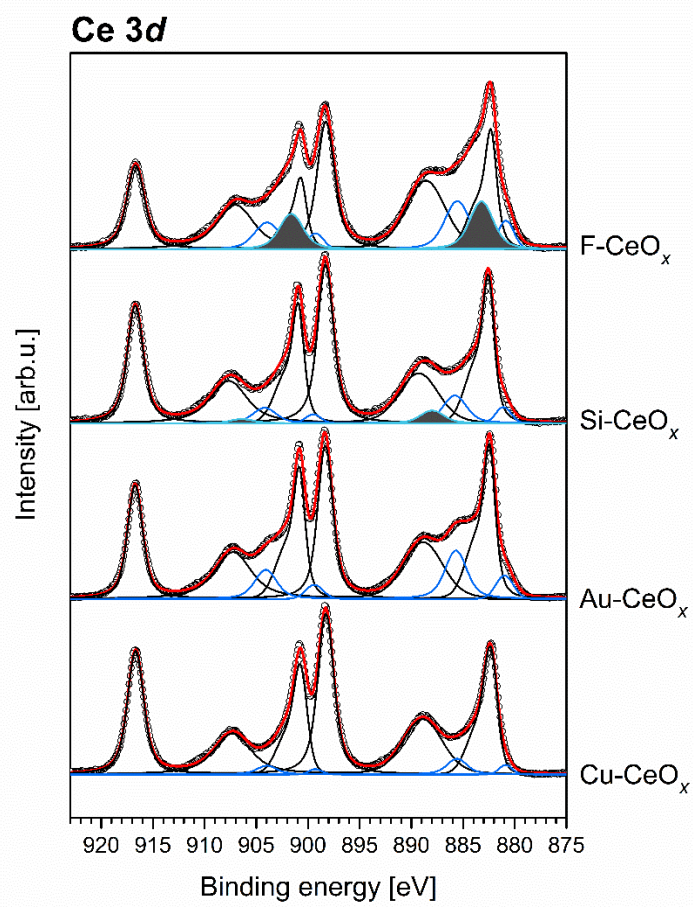

Figure 12: Ce 3*d* spectra of cerium oxide doped by (from top to bottom) fluorine (measured at SuperESCA, Elettra, *hv* ~ 1256.0 eV), silicon, gold and copper (measured at BL15XU, SPring-8, *hv* ~ 5950.2 eV).

containing 5% and 8% of gold and copper, respectively, were prepared by radio frequency magnetron sputtering. While copper is mostly in the Cu^{2+} state which is consistent with other experimental and theoretical studies of Cu-CeO_x mixed oxides [38, 99, 103], gold occurs in Au^{+} and Au^{0} oxidation states. Gold dopants substituting Ce^{4+} ions in the bulk cerium oxide are stable in the Au^{3+} state [37, 100]. Reduced gold species can be found in areas of defected cerium oxide, such as grain boundaries, a surface or an interface with the substrate [44]. In this case, a roughness of the film caused by the interaction of CeO_x with the C substrate during the deposition is responsible for a high amount of Ce^{3+} species seen in Figure 12 [30].

The situation is different when a dopant does not substitute the Ce^{4+} ion in the cerium oxide lattice but forms a new compound, such as silicate or fluoride. The electron structures of such compounds may differ significantly from that of pure cerium oxide which may lead to different core hole screening and different final

states [50]. Therefore, new states can be expected in the photoelectron spectra. The Ce 3*d* spectra of Si-doped and F-doped cerium oxide are shown in Figure 12. The spectra were fitted by the same fitting procedure as Au-CeO_x and Cu-CeO_x, keeping positions and widths of the peaks fixed. But in both cases, an additional doublet emerged in the spectra. The difference between the spectra of F-CeO_x and Au-CeO_x, showing similar degrees of reduction, is apparent at the first glance. A new spectral component appears at approximately 883 eV (Ce $3d_{5/2}$). According to the work of our colleague, this component could be ascribed to CeF_3 or CeF_yO_{2-y} (results not published yet) where fluorine would substitute oxygen ions. In the case of Si-CeO_x, a new spectral component is not as prominent as that of F-CeO_x. However, its existence is supported by a set of data presented by Vorokhta et al. [50]. The new peaks can be assigned to cerium silicates. These are often formed at the interface between cerium oxide thin films and the silicon support due to a migration of Si atoms from the substrate to the overlayer [50, 104–106].

A correct analysis of the Ce 3*d* spectra of CeO_x-based compounds is not an easy task. New components can be easily concealed in broad spectral features, like in the case of Si-CeO_x. Therefore, a systematic analysing the sets of data (for instance, samples with different concentrations of the dopant) or combining several different experimental techniques is usually required to characterize the system properly. Next few chapters focus on the characterization of the cerium oxide thin films doped by rhodium.

4.2 Characterization of Rh-CeO_x with different concentrations of rhodium

Cerium oxide thin films with various concentrations of rhodium were deposited by radio frequency magnetron sputtering onto Si single crystals. The surface of silicon crystals were passivated by a 60 nm thick SiO_2 layer. Chemical composition of the Rh-CeO_x thin films was characterized by the means of the photoelectron spectroscopy. Various energies of exciting photons were used to probe either deeper areas of the films (HXPS), or the near-surface areas (XPS, SXPS, UPS and RPES). The atomic concentration of the dopant was derived from XPS (more details in Section 2.3.4). The morphology of the films was investigated by the scanning electron microscopy (SEM) and X-ray diffraction (XRD).

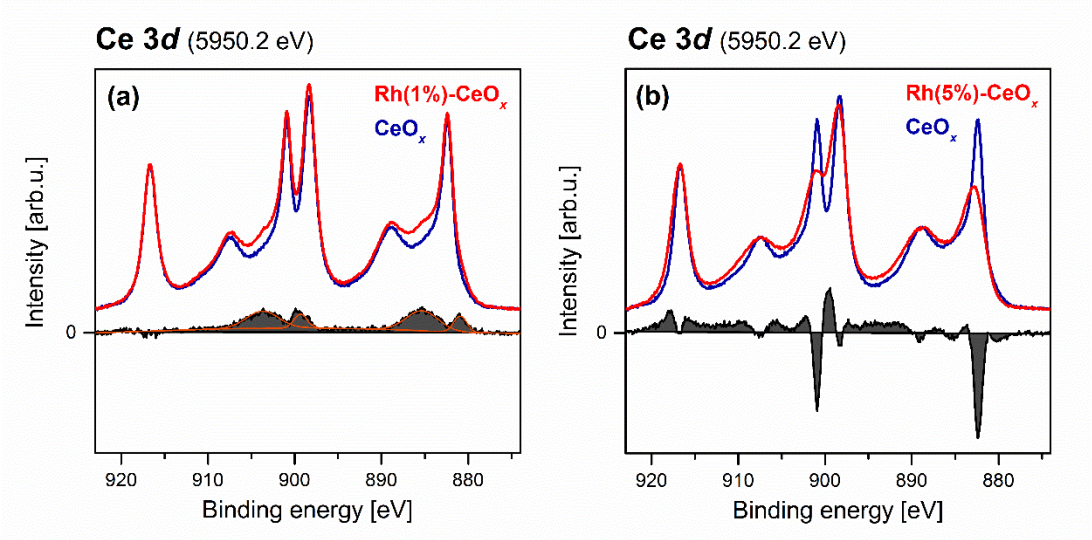

Figure 13: Difference spectra of undoped and Rh-doped CeO_x (black lines with filled areas under the curves). Red lines represent pure cerium oxide, blue lines cerium oxide doped by (a) 1% and (b) 5% of rhodium. Measured at BL15XU, SPring-8, $h\nu \sim 5950.2$ eV.

First, we focus on the analysis of the Ce 3*d* photoelectron spectra because it could show signs of a rhodium-based compound with different final state configuration than that of ceria, such as rhodates [107, 108] or Rh-Ce alloys [109–111]. Figures 13 (a) and (b) show Ce 3*d* spectra of two Rh-CeO_x samples with 1% and 5% or rhodium (red lines), respectively. These are compared with the Ce 3*d* spectrum of the reference undoped CeO_x sample prepared and measured in the same conditions (blue lines). All spectra were normed to the intensity at 916.7 eV.

The spectrum of Rh(1%)-CeO_x does not differ much from that of pure cerium oxide. The difference spectrum plotted in Figure 13 (a) by a black line shows only an increased concentration of Ce^{3+} ions. The situation is different for cerium oxide with 5% of rhodium in Figure 13 (b). We can see that the peaks are not as sharp as in the case of pure cerium oxide. Also, their relative ratio changed significantly. No new component can be discerned from the difference spectrum plotted in Figure 13 (b). It shows only a broadening of the peaks and a lower intensity of the Ce^{4+} f^2 component. Therefore, the Ce 3*d* spectra were fitted according to the standard procedure described in 2.3.2 but the widths of the peaks were not restricted.

The HXPS and XPS spectra of the Ce 3*d* region for the Rh-CeO_x samples with various concentrations of rhodium and the reference sample, pure CeO_x, are plotted in Figures 14 (a) and (b), respectively. The spectra are normalized to the total

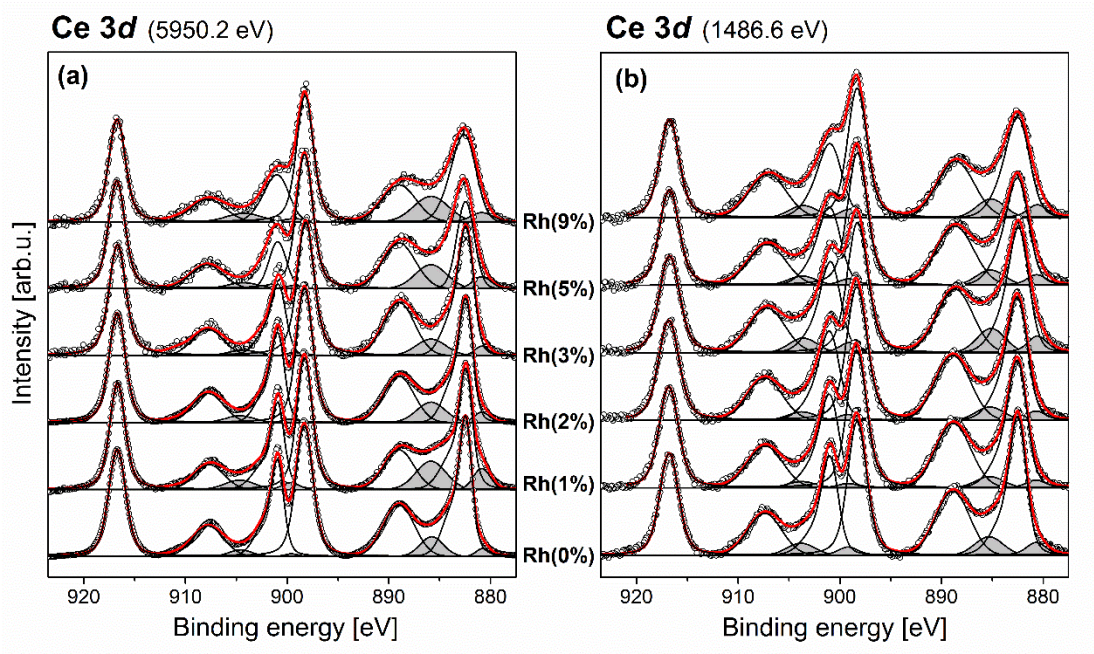

Figure 14: (a) HXPS and (b) XPS Ce 3*d* spectra of Rh-CeO_x samples with different Rh concentrations (1-9%) and the reference CeO_x sample (0%). Measured data are displayed by round scattered symbols, fitting components by thin solid lines (Ce^{3+} components tinged with grey), and fitting results by red lines. Spectra were normalized to the total area.

area under the curve after the background subtraction. We can see that the Ce^{4+} state prevails in all samples and for both, XPS and HXPS. The broadening of the peaks with an increasing concentration of rhodium is also apparent in both, deeper layers and near-surface areas. It suggests that the chemical composition of the Rh-CeO_x films is more or less homogeneous.

The same peak-broadening was observed for ceria films doped by platinum prepared by magnetron sputtering and it was explained by a formation of a solid solution of platinum and cerium oxide [102]. The Rh-CeO_x films also exhibit signs of a solid solution. The broadening of the peaks may be caused by a disruption of the bond lengths in the ceria lattice due to the presence of the dopant, which can be quite significant for higher dopant concentrations. The decreased intensity of the Ce^{4+} f^2 components might be a result of changes in the valence state hybridization (Rh 4*d* or Pt 5*d* states are involved [39]) leading to an alteration of the final state configuration.

Figures 15 (a) and (b) show HXPS and XPS spectra of the O 1*s* region for the Rh-CeO_x samples with various concentrations of rhodium (1-9%) and the CeO_x

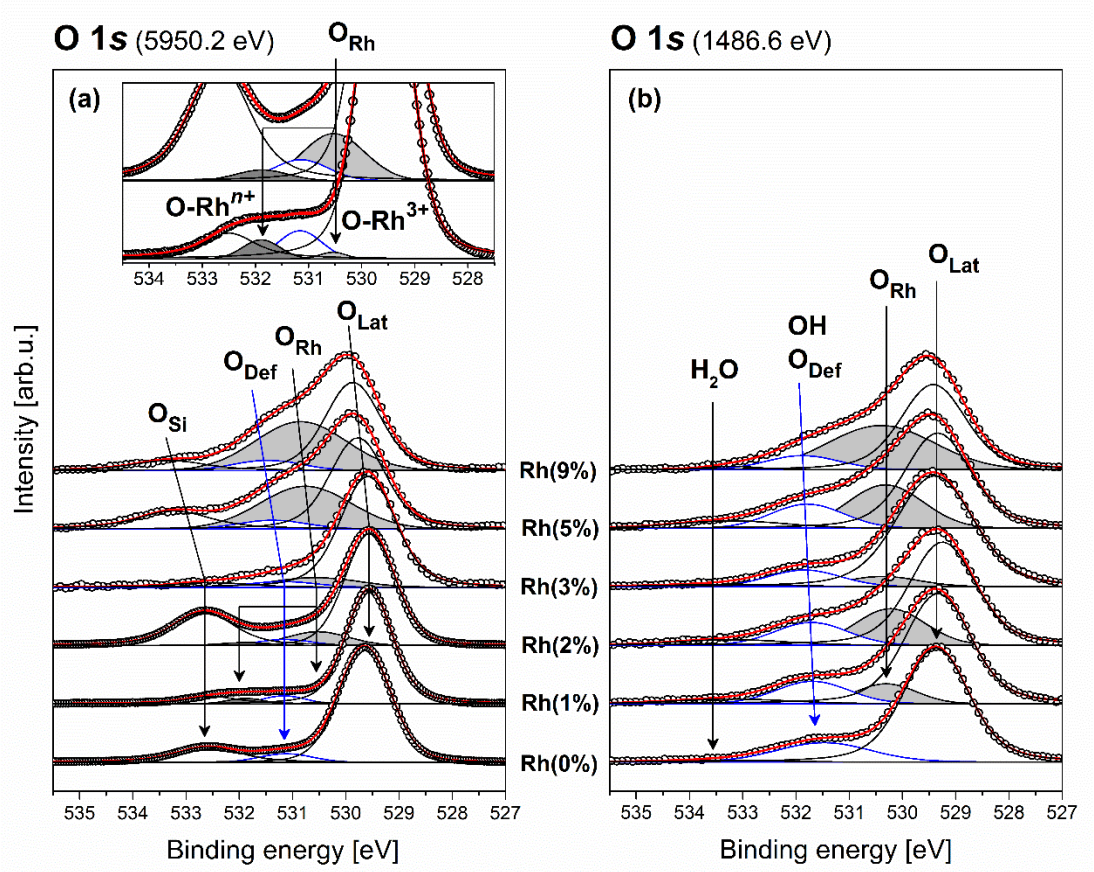

Figure 15 (a) HXPS and (b) XPS O 1*s* spectra of Rh-CeO_x samples with different Rh concentrations (1-9%) and the reference CeO_x sample (0%). The inset of graph (a) shows fitted HXPS spectra of Rh(1%)-CeO_x and Rh(2%)-CeO_x. Measured data are displayed by round scattered symbols, fitting components by thin solid lines (O_{Rh} components tinged with grey, O_{Def} coloured by blue), and fitting results by red lines. Spectra were normalized to the total area.

reference sample (0%). The spectra are normalized to the total area. Figure 16 (a) and (b) show the corresponding HXPS and XPS Rh 3*d* spectra, respectively.

First, we will focus on the HXPS O 1*s* spectrum of the pure cerium oxide plotted at the bottom of Figure 15 (a). The main component at binding energy of 529.7 eV marked as O_{Lat} corresponds to oxygen from the ceria lattice [47, 66, 75, 81, 82]. Another component found at approximately 532.6 eV, O_{Si}, was assigned to oxygen from SiO_2 according to the measurements of the O 1*s* spectrum from the reference SiO_2/Si substrate. The third oxygen peak located at approximately 531.2 eV, labelled as O_{Def} and coloured by blue, can be associated with oxygen species with lower coordination compared to oxygen ions from the ceria lattice [47, 75]. These oxygen species are related to Ce^{3+} ions. As was mentioned in Section 4.1,

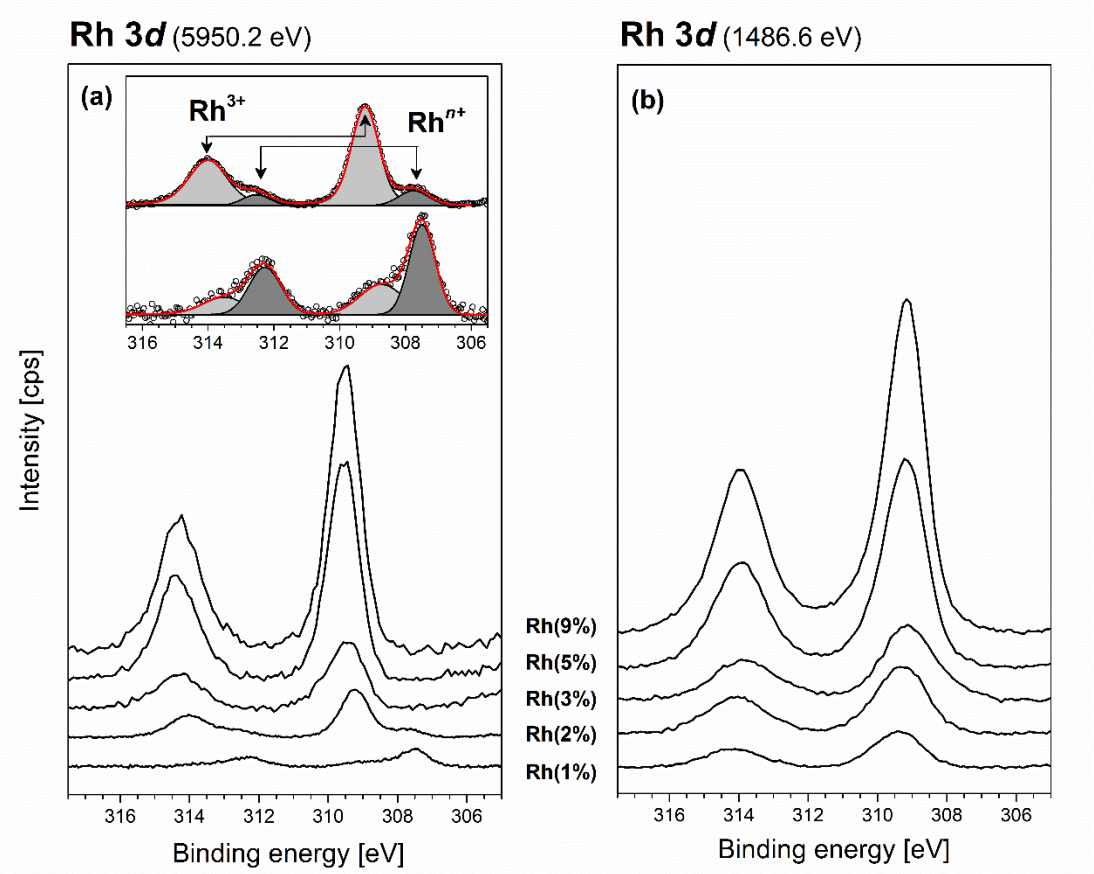

Figure 16: (a) HXPS and (b) XPS Rh 3*d* spectra of Rh-CeO_x samples with different Rh concentrations (1-9%). The inset of graph (a) shows fitted HXPS spectra of Rh(1%)-CeO_x and Rh(2%)-CeO_x normalized to the total area. Measured data are displayed by round scattered symbols, fitting components by thin solid lines tinged with light grey (Rh^{3+}) and dark grey (Rh^{n+}), and fitting results by red lines.

Ce^{3+} ions are located mainly in areas of defective crystal structure, such as crystal grain boundaries, the surface or the interface with the substrate. It was reported that these areas contain a high amount of low-coordinated and weakly bound oxygen anions (marked as O_{Def}) [34, 47, 88, 112]. These oxygen ions are very important for catalytic reactions because they enhance the OSC of ceria [32].

The contribution of O_{Def} to the O 1*s* spectrum reaches approximately 6 % which agrees very well with the contribution of Ce^{3+} ions to pure CeO_x shown in Figure 17 (a). Judging from a relatively high intensity of Ce^{3+} components in the HXPS spectra, it seems that the pure CeO_x films contain a high amount of structural defects. Because the contribution from the surface area to HXPS spectrum is very small and the influence of the substrate and interfacial silicates can be neglected due to the pre-oxidized Si substrate and the sufficient thickness of the CeO_x film [50,

113], the majority of structural defects originates from grain boundaries in the cerium oxide film. The polycrystalline character of the CeO_x films was supported by XRD.

The XPS O 1*s* spectrum of the pure CeO_x plotted in Figure 15 (b) consists of the O_{Lat} component and two additional peaks at binding energies of 531.6 eV and 533.5 eV. The O_{Lat} component corresponds to oxygen form the ceria lattice. The peak at 531.6 eV was marked as O_{Def} in consistence with the HXPS spectrum in Figure 15 (a). It is more intensive and slightly shifted to higher binding energies compared to the HXPS spectrum. Because XPS is more surface sensitive than HXPS, the peak can originate not only from low-coordinated oxygen ions bound to Ce^{3+} but also from surface adsorbates, such as OH [66, 82–84] or CO [114]. The small peak at 533.5 eV can be assigned to water molecules chemisorbed at the surface [82, 84].

Further, we compare the XPS and HXPS O 1*s* spectra of pure cerium oxide with those of Rh-CeO_x mixed oxide. Two additional peaks can be found in the XPS and HXPS O 1*s* spectra of Rh-CeO_x compared to undoped cerium oxide. These new peaks can be found at approximately 1 eV and 2.3 eV above the O_{Lat} component. The component at 1 eV above O_{Lat} is discernible in all the Rh-CeO_x spectra and it is apparently increasing with the concentration of rhodium. These are collectively marked as O_{Rh}.

The increasing contribution of O_{Rh} to the O 1*s* spectra is also apparent from Figure 17 (b). It shows the ratio of peak areas from O_{Rh} and O_{Σ}. The latter represents the sum of all O 1*s* components originating from the Rh-CeO_x film ($O_{\Sigma} = O_{Lat} + O_{Def} + O_{Rh}$). The contributions from surface adsorbates and the substrate are excluded from O_{Σ}. The component at higher binding energy was detected only by HXPS and only for the samples containing 1% and 2% of rhodium (see the inset of Figure 15 (a)). This is consistent with Rh 3*d* spectra presented in Figure 16. HXPS measurements of the films doped by 1% and 2% of rhodium showed two states of rhodium contrary to other Rh 3*d* spectra. The emergence of the new components and their correlation with the amount of rhodium in the Rh-CeO_x films suggest that both of these peaks are related to rhodium.

The O_{Rh} peak 1 eV above O_{Lat} could be assigned to oxygen bound to Rh^{3+} ions (O-Rh^{3+}). Values of the O-Rh^{3+} binding energy reported in the literature vary from 530.3 eV to 532.0 eV [83, 107, 115]. The binding energy measured for our Rh-CeO_x films fit well into this range. It also coincides with the energy attributed to oxygen from mixed oxide systems, such as Sn-O-Ce [81] and Ga-O-Ce [75].

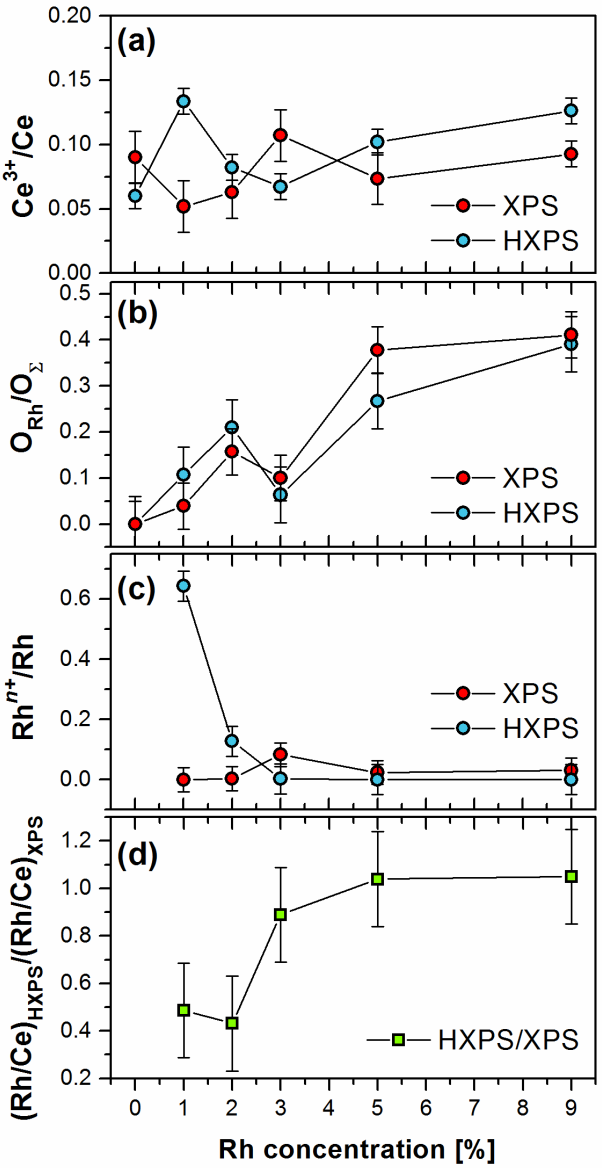

Figure 17: Comparison of (a) Ce^{3+}/Ce, (b) O_{Rh}/O_{Σ}, (c) Rh^{n+}/Rh and (d) $(Rh/Ce)_{HXPS}/(Rh/Ce)_{XPS}$ ratios derived from XPS (1486.6 eV) and HXPS (5950.2 eV) for Rh-CeO_x samples with different Rh concentrations (1-9%) and the reference CeO_x sample (0%). The parameters in (a-c) (HXPS - blue symbols, XPS - red symbols) were calculated as the ratio of the peak area corresponding to the particular fitting component (Ce^{3+}, Rh^{n+}) to the area of the respective region (Ce 3*d* and Rh 3*d*), or a sum of relevant peak areas (O_{Rh} = O-Rh^{n+} + O-Rh^{3+}, $O_{\Sigma} = O_{Rh} + O_{Lat} + O_{Def}$ in the O 1*s* region). The parameter in (d) was estimated as a ratio of Rh/Ce proportions obtained from HXPS and XPS.

Therefore, we can expect the existence of the Rh-O-Ce bonds in Rh-CeO_x. The O_{Rh} component approximately 2.3 eV above O_{Lat} could correspond to oxygen bound to rhodium with lower valency than Rh^{3+}, analogically to Au-CeO_x discussed in Section

4.1 and in consistence with Rh 3*d* spectra (Figure 16). We refer to it as Rh^{n+} and the corresponding O 1s peak is labelled as O-Rh^{n+}.

Figure 16 shows the Rh 3*d* spectra obtained by HXPS (a) and XPS (b) for the Rh-CeO_x samples with various concentrations of rhodium. We can clearly see a growing intensity of the Rh peaks with the increasing concentration of rhodium. The Rh 3*d* spectra consist of two spin-orbit doublets, marked as Rh^{3+} and Rh^{n+}. The fits of the HXPS spectra of the samples Rh(1%)-CeO_x and Rh(2%)-CeO_x are plotted in the inset graph of Figure 16 (a) for an illustration of both components. To simplify a following discussion, we will be referring only to the Rh $3d_{5/2}$ peaks of the Rh 3*d* doublet.

The most prominent Rh $3d_{5/2}$ component is located at around 309.2 eV. According to the literature [20, 40, 83, 116], this feature can be attributed to Rh^{3+} ions dispersed in the ceria lattice. Yang et al. calculated that Rh ions would substitute Ce^{4+} in the ceria lattice [39]. The experiments performed by Gayen et al. led to the same conclusion [35]. According to Hedge et al. [98], it is energetically favoured for Rh^{3+} ions to substitute Ce^{4+} ions. Furthermore, cerium favours the Ce^{4+} state.

These statements agree very well with our results. It suggests that the Rh-CeO_x sputtered thin films are in a form of a mixed oxide. The Rh-O-Ce bond is characteristic for the rhodium-cerium mixed oxides [20, 35, 39, 40, 42, 88]. The emergence of the O_{Rh} components discussed above supports the existence of the mixed oxide phase in Rh-CeO_x.

Apart from Rh^{3+}, we can find another rhodium component in the Rh 3*d* spectra. In Figure 16, we can clearly distinguish the Rh $3d_{5/2}$ peak at approximately 307.6 eV. It is marked as Rh^{n+}, while $n+$ is expected to be between 3+ and 0 oxidation states judging from the binding energy. This component is most prominent in the HXPS spectra for the samples with low concentrations of rhodium. It is clearly seen in Figure 17 (c) showing the contribution of Rh^{n+} to the Rh 3*d* spectra. We may notice that the occurrence of the Rh^{n+} state in the Rh 3*d* spectra corresponds to the occurrence of the O_{Rh} component located at 2.3 eV above O_{Lat} in the O 1*s* spectra. Therefore, we can relate this oxygen peak to Rh^{n+}.

The most possible interpretation of the Rh^{n+} state is that it arises from rhodium atoms or ions highly dispersed in the sputtered Rh-CeO_x thin films having lower valence compared to Rh^{3+}. Determining the nature and the oxidation state of

the Rh^{n+} specie is rather difficult but it will be discussed in more details in Section 4.3 which is focused on thermal stability of the Rh-CeO_x films.

A comparison of the Rh^{n+}/Rh ratio in Figure 17 (c) shows that the relative contribution of Rh^{n+} to Rh 3*d* decreases with the increasing concentration of rhodium in deeper layers of the Rh-CeO_x films. But the Rh^{n+} concentration remains relatively stable (though almost negligible) in the near-surface regions. The difference may be caused by an inhomogeneity of the rhodium concentration. Figure 17 (d) shows a ratio of Rh/Ce proportions obtained by HXPS (deep-laying regions) and XPS (near-surface region) for all the Rh-CeO_x films. The Rh/Ce was calculated as the ratio of the Rh $3d_{5/2}$ to Ce $3d_{5/2}$ photoelectron peak areas divided by corresponding photoionization cross-sections [52].

We can see that the $(Rh/Ce)_{HXPS}/(Rh/Ce)_{XPS}$ ratio equals approximately 1 for the films doped with 3%, 5% and 9% of rhodium. It means that rhodium is relatively evenly dispersed through these films. On the other hand, the $(Rh/Ce)_{HXPS}/(Rh/Ce)_{XPS}$ ratio for the Rh(1%)-CeO_x and Rh(2%)-CeO_x films is around 0.5. It means that the concentration of rhodium at the near-surface area is higher compared to deeper layers of the films. This result is in agreement with the work of Sayle et al. [117]. They calculated that the Rh dopants in ceria would segregate at the surface and the segregation would be stronger for lower concentrations of rhodium.

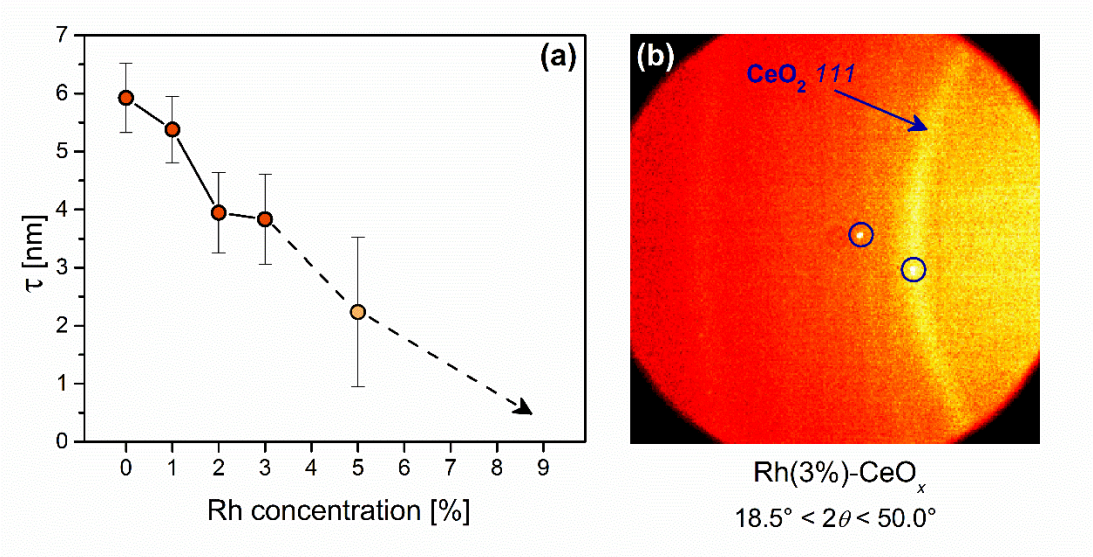

Figure 18: (a) Size of CeO_2 crystallites in the Rh-CeO_x films estimated for samples with different concentrations of rhodium, as well as the reference CeO_x film (0%). (b) The XRD diffraction pattern of the Rh(3%)-CeO_x thin film. Blue circles mark spots from the Si single crystal.

Morphology of the Rh-CeO_x films was investigated by X-ray diffraction (XRD) and scanning electron microscopy (SEM). XRD diffraction patterns consisted of weak diffractions rings and sharp spots. The rings can be assigned to CeO_2 showing that cerium oxide thin films have a polycrystalline character. The spots originate from the diffraction on the single crystalline silicon support. No signs of rhodium-based compounds were found in the spectra.

The ring pattern became less clear with higher concentrations of rhodium. The broadening and weakening of the CeO_2 diffraction peaks with higher concentrations of rhodium were detected also by the scintillating detector. Figure 18 (a) shows a size of CeO_2 crystallites in the Rh-CeO_x and CeO_x films derived from the diffractograms according to the Sherrer formula (2). The thin film of pure cerium oxide is composed of approximately 6 nm large crystallites. When it is doped by rhodium, the crystallites become gradually smaller with the increasing concentration of the dopant. For concentrations higher than 5%, the diffraction peaks are already hardly discernible. That is why these are only indicated by an arrow in Figure 18 (a).

SEM images of the Rh(1%)-CeO_x and Rh(6%)-CeO_x are displayed in Figures 19 (a) and (b), respectively. We can see that the surface of the film with 6% of rhodium is almost completely flat while the surface of the film containing 1% of rhodium is relatively rough. It shows signs of very small grains. This is consistent with the interpretation of the XRD measurements.

If we summarize the results from XRD and SEM we may conclude that the films with low concentrations of rhodium are polycrystalline but the films with higher concentrations exhibit an amorphous character. The dependence of the film

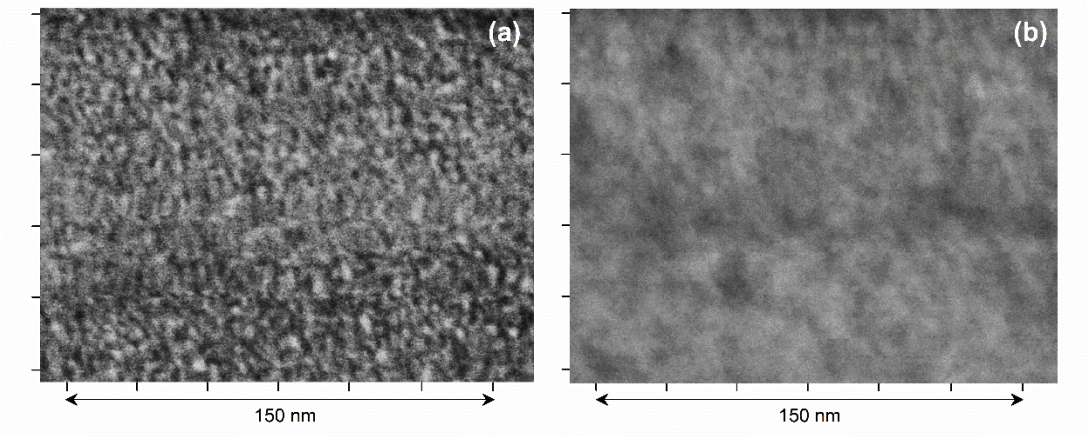

Figure 19: SEM images of (a) Rh(1%)-CeO_x and (b) Rh(6%)-CeO_x.

structure on the concentration of the dopant is a very important result because the structure of the films and their surface morphology can significantly influence the properties of the system which is demonstrated in Section 4.4.

Furthermore, we would like to point out an interesting difference between doped and undoped cerium oxide films. Figure 17 (a) shows that Ce^{3+} ions are more concentrated in the near-surface area compared to deeper layers of the CeO_x film. This is consistent with the literature [47]. However, the situation is opposite in the case of the Rh-CeO_x films. This difference may be caused by the presence of the Rh atoms disrupting the CeO_2 structure (especially Rh^{n+} judging from the comparison of Figures 17 (a) and (c)).

Another reason for these differences may be the stoichiometry of the films. We estimated the stoichiometries of all investigated films from the atomic concentrations derived by XPS and plotted them into the Rh-Ce-O phase diagram displayed in Figure 20. Red circles correspond to the studied Rh-CeO_x thin films, green circles to known phases of rhodium-cerium mixed oxides [40, 41], and blue circles to the stable oxides. We can see that the studied Rh-CeO_x thin films do not

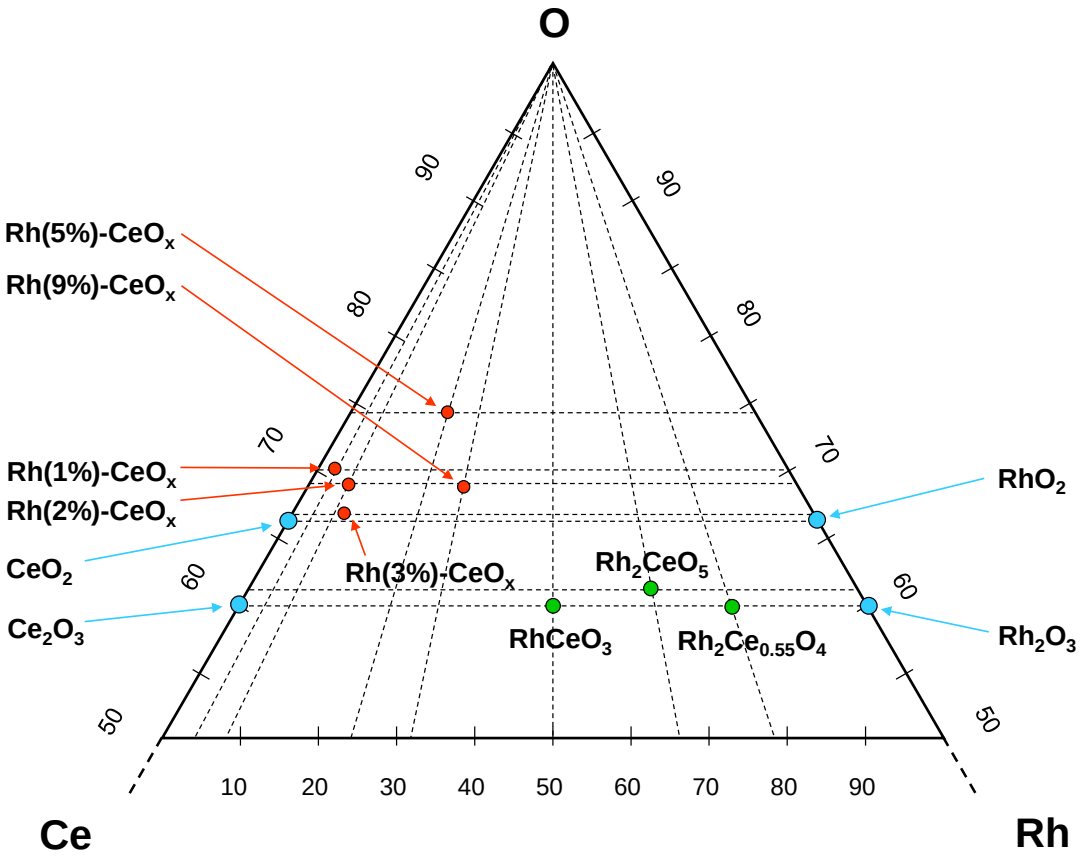

Figure 20: The Rh-Ce-O phase diagram.

coincide with any known phase of rhodium-cerium mixed oxide, nor oxide. The exception is Rh(3%)-CeO_x whose stoichiometry is very close to $Rh_yCe_{1-y}O_{2-\delta}$ described by Gayen et al. [35]. The other films contain relatively more oxygen.

The Rh(3%)-CeO_x is rather exceptional. We can see from Figure 17 that the characteristics of the Rh(3%)-CeO_x film slightly deviates from those of other Rh-CeO_x films. It resembles undoped cerium oxide more than other doped oxides. The reason behind these differences is still unknown but one possible explanation is a structure of the Rh-CeO_x films. As was discussed above, the films with low concentrations of rhodium have different structure than the films with higher concentrations. The properties of these two types of films are also different. The films containing approximately 3% of rhodium are in a kind of a transition state between two Rh-CeO_x film morphologies. Characterizing these films is not much straightforward because the properties of both structures are mixed together. Therefore, we focus more intensely on the Rh-CeO_x films with lower or higher concentrations of Rh.

4.3 Thermal stability of Rh-CeO_x

Thin films of Rh-CeO_x mixed oxides are investigated mainly from the viewpoint of catalysis. The stability at elevated temperature and under various conditions is one of the most important properties of the catalyst. Therefore, a special attention was paid to the thermal stability of the Rh-CeO_x thin films under different environments.

At first, we focus on the annealing of *ex situ* prepared films in the UHV conditions. Figure 21 (a) shows the evolution of Rh $3d_{5/2}$ of Rh(6%)-CeO_x with the increasing temperature. The sample was heated continuously with a temperature ramp of five degrees per minute and the Rh $3d_{5/2}$ region was measured approximately every minute using the photon energy of 420.0 eV. After reaching temperatures of 473, 523, 580, 620 and 774 K, the sample was cooled down to the room temperature (~ 300 K) and all regions were measured to check the state of the sample. The Ce $3d$ spectra are plotted in Figure 21 (b). We can see that both rhodium and cerium undergoes a reduction with increasing temperature.

Figure 22 shows an example of the Rh $3d_{5/2}$ spectrum. It is composed of three components which are marked as Rh^{3+}, Rh^{n+} and Rh^0. All Rh $3d_{5/2}$ spectra in

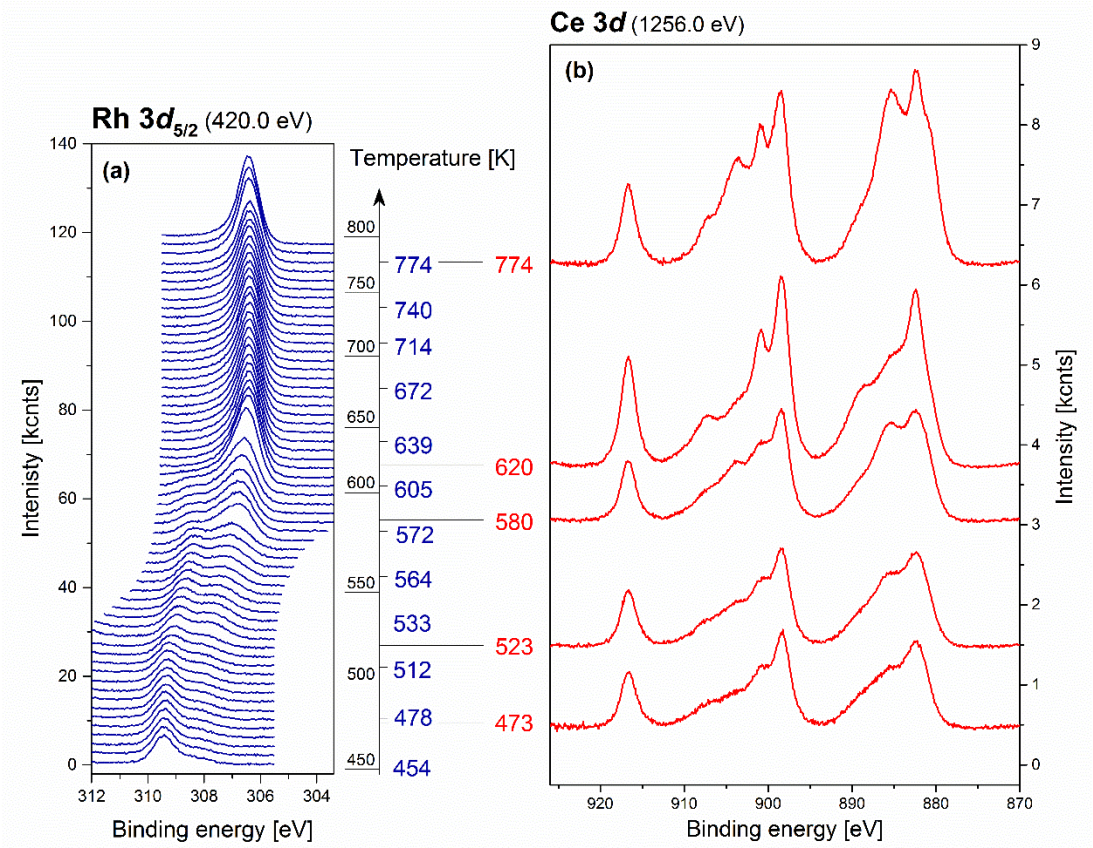

Figure 21: (a) the Rh3 $d_{5/2}$ region time scan of Rh(6%)-CeO_x measured during heating from 450 to 800 K at elevated temperature (blue), and (b) Ce 3*d* region of Rh(6%)-CeO_x measured after heating the sample at the marked temperature (red) and after cooling down below 350 K (measured at SuperESCA, Elettra).

Figure 21 (a) were fitted by these three peaks. A development of their peak areas and the binding energies are plotted in Figures 23 (a) and (b), respectively.

At 300 K, the Rh $3d_{5/2}$ spectrum consists of a main component at 309.4 eV with a shoulder at 307.6 eV. According to the discussion in Section 4.2, the component at 309.4 eV can be assigned to Rh^{3+}. The peak at lower binding energy is referred to Rh^{n+}. This configuration remains relatively stable up to 525 K. Above this temperature, a new peak, Rh^0, emerges in the Rh $3d_{5/2}$ spectra. A signal from Ce^{3+} ions becomes also more prominent in the Ce 3*d* spectra (Figure 21 (b)). Up to 625 K, the area of the Rh^{3+} peak continuously decreases, while the areas of Rh^0 and Rh^{n+} increase. Above 625 K, the composition of Rh $3d_{5/2}$ spectra does not change significantly. We can see that there are no signs of Rh^{3+} and that the other peak areas slightly decrease (Figure 22 (a)). There is also a noticeable sharpening of the Rh^0 peak above 625 K (Figure 21 (a)). Furthermore, if we look at the Ce 3*d* spectrum at

620 K plotted in Figure 21 (b) we can see that cerium is slightly re-oxidized and its peaks appear narrower. After annealing to even higher temperature, cerium becomes more reduced.

The interpretation of these data may be as following. When the Rh-CeO_x is annealed, some of its most labile oxygen species are released from their bonds. It results in the reduction of Rh^{3+} and Ce^{4+} ions. In the case of rhodium, Rh^{n+} is formed preferentially to Rh^0. The temperature above 525 K is necessary to form Rh^0. Rh^0 shows signs of the coalescence at higher temperatures (the peak sharpening and the intensity decrement). The binding energy of this component measured at the room temperature was 307.1 eV which corresponds well to the value obtained for metallic

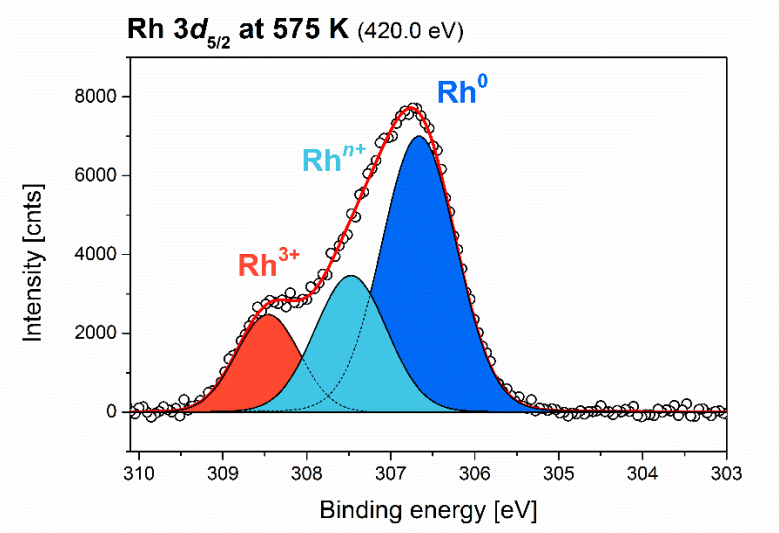

Figure 22: Rh $3d_{5/2}$ of Rh(6%)-CeO_x at 575 K (measured at SuperESCA, Elettra).

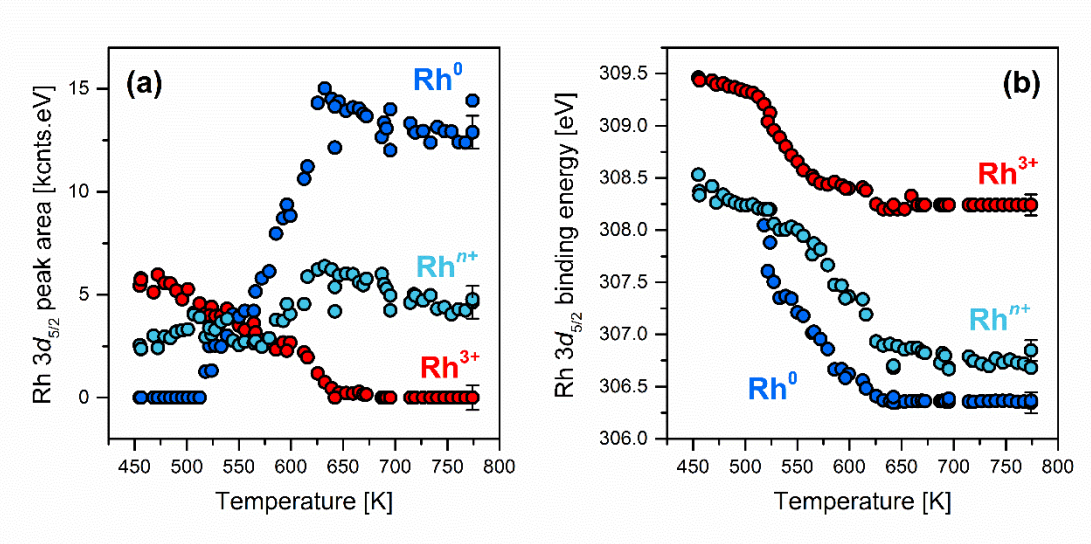

Figure 23: Fitting parameters of the Rh3 $d_{5/2}$ region during heating of Rh(6%)-CeO_x from 450 to 800 K (measured at SuperESCA, Elettra).

rhodium [80]. Therefore, Rh^0 can be assigned to rhodium from the Rh particles formed above 525 K. Rh^{n+} species could be attributed to reduced rhodium atoms dispersed in the ceria lattice. Above 625 K, all traces of Rh^{3+} disappear as all Rh-O-Ce bonds are decomposed. The released oxygen atoms can temporarily fill the vacancies in cerium oxide, resulting in its partial re-oxidation. Further annealing causes the reduction of cerium because the high temperature enhances the migration of oxygen and weakly bound rhodium. As a result, rhodium particles grow bigger.

These results suggest that the Rh-CeO_x thin film completely decomposes above 625 K and rhodium and cerium oxide form separate phases. The concentration of rhodium dopant does not change this fact; only the temperature necessary for the decomposition of the films is different. Our measurements showed that the Rh-CeO_x films with lower concentrations of rhodium are more reducible and the temperature needed for a complete decomposition is lower compared to the films with higher concentrations of dopants (525 K for Rh(1%)-CeO_x). The oxygen released from the reduction of the Rh-CeO_x films is spent either to reactions with surface contaminants (the intensity of carbonaceous species in the C 1*s* spectra decreases), or the oxidation of the substrate.

Another interesting feature of Figure 21 (a) is the apparent shift of the Rh $3d_{5/2}$ peaks to lower binding energies in the temperature range between 300 and 625 K. The shift may reach up to 1.4 eV. This effect may be caused by an enhanced conductivity of the Rh-CeO_x films at elevated temperature. It is consistent with the work of Mizoguchi et al. [40] who reported a semiconductive character of the Rh-CeO_x mixed oxide systems. An absence of this energy shift above 625 K suggests some major modification of the material, such as the separation of rhodium and cerium oxide phases discussed above.

Furthermore, we would like to point out the difference between thermal stabilities of the films annealed in the ultra-high vacuum conditions and in the atmospheric pressure. Figures 24 (a) and (b) show developments of Rh^{3+}/Rh and Ce^{3+}/Ce ratios in Rh-CeO_x films with 5 and 6% of rhodium. We can see that both rhodium and cerium reduced when the sample was annealed in UHV. The reduction of rhodium starts around 480 K. On the contrary, no reduction was observed when heated in air and atmospheric pressure. The Rh-CeO_x film is stable up to 800 K which is a very important result from the viewpoint of catalysis.

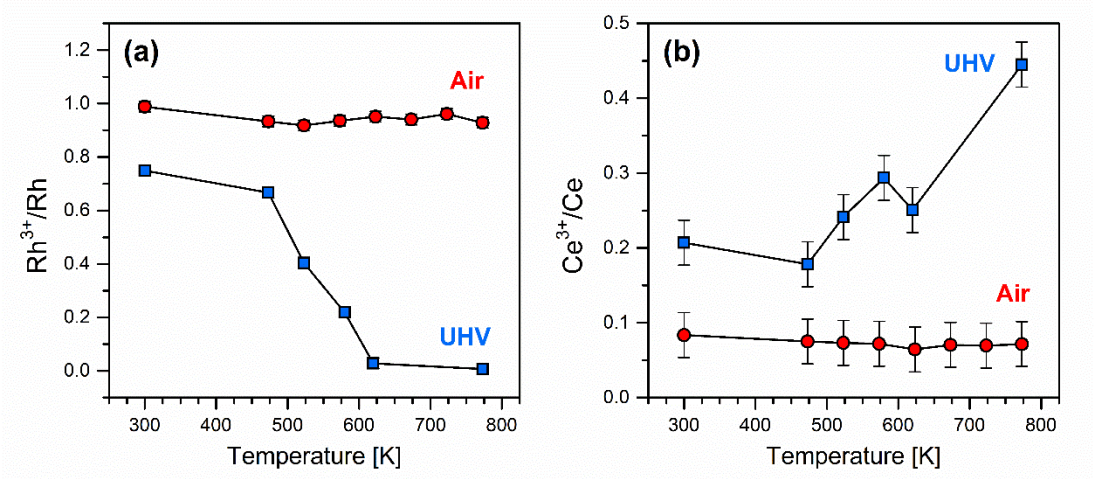

Figure 24: Evolution of the Rh^{3+}/Rh and Ce^{3+}/Ce ratios for Rh(5%)-CeO_x heated in air and atmospheric pressure (red circles, measured at HEAP Lab, 5414.7 eV), and Rh(6%)-CeO_x heated in UHV (blue squares, measured at SuperESCA, 420.0 and 1256.0 eV).

Further discussion will deal with an influence of the interaction with the substrate, or the surface adsorbates on the thermal stability of the Rh-CeO_x films. In order to avoid the influence of the adsorbates as much as possible, the Rh-CeO_x films were deposited and subsequently heated in UHV conditions. All treatment was performed *in situ* (MSB, Elettra). The Rh-CeO_x films with 5% of rhodium were deposited onto the SiO_2 and Cu substrates. The reference CeO_x thin films were prepared in the same conditions. In order to estimate the effect of adsorbates on the behaviour of the Rh-CeO_x films, one sample prepared in UHV was exposed to the air for 24 hours.

Figure 25 shows the evolution of the resonant enhancement ratio (9) during subsequent heating of the Rh-CeO_x and CeO_x films supported by different substrates. The samples were heated step by step from 300 K to 800 K. The photoelectron spectra were acquired after cooling the samples down to the room temperature. Corresponding Rh 3*d* spectra for Rh-CeO_x supported by copper and silica are plotted in Figures 26 (a) and (b), respectively. We can see from both graphs that before heating, all rhodium was in the Rh^{3+} state and the majority of cerium occupied the Ce^{4+} state.

At first, we focus on the pure cerium oxide films, CeO_x/Cu and CeO_x/SiO_2. We can see from Figure 25 that the $D(Ce^{3+})/D(Ce^{4+})$ ratio for CeO_x/SiO_2 is relatively stable in the whole temperature range. A slight reduction can be noticed below 450 K. The changes in the O 1*s* and C 1*s* spectra (data not shown) indicate that this

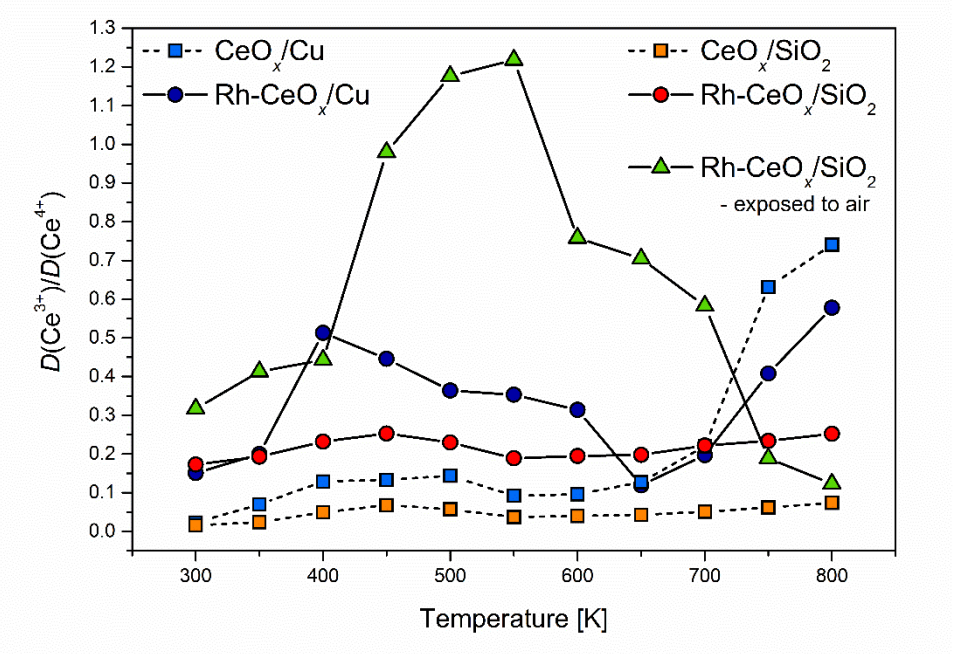

Figure 25: Evolution of the resonant enhancement ratio during subsequent heating in UHV for the CeO_x and Rh-CeO_x thin films deposited onto the Cu and SiO_2 substrates. The films marked by squares and circles were treated *in situ*, the film marked by triangles was exposed to the air for 24 h prior to heating. The valence band spectra were acquired using energies of 121.4, 124.8 and 115.0 eV (measured at MSB, Elettra).

reduction is caused by surface contaminants desorbing from the surface at elevated temperatures. The re-oxidation at around 600 K may result from an enhanced migration of oxygen in the cerium oxide thin film. The situation is different for CeO_x/Cu. The trends of the $D(Ce^{3+})/D(Ce^{4+})$ ratios for CeO_x/Cu and CeO_x/SiO_2 are very similar up to 600 K but in the case of CeO_x/Cu, an intense reduction of cerium occurs above 600 K. Judging from a significant increase of the Cu 2*p* intensity (data not shown), the cerium oxide undergoes some major modifications in the morphology of the film, such as a formation of three-dimensional particles. Simultaneously, a massive amount of oxygen is released from the film causing the reduction of cerium.

Rh-CeO_x treated in situ exhibits similar trends of the resonance enhancement ratio as CeO_x. The only difference between the Rh-CeO_x/SiO_2 and CeO_x/SiO_2 films is an initial offset of the $D(Ce^{3+})/D(Ce^{4+})$ ratios. We can see from Figure 25 that the doped oxide contains more Ce^{3+} ions than the pure cerium oxide. This difference can be explained by a higher amount of structural defects in the Rh-CeO_x films which results in a higher occurrence of Ce^{3+} ions, as was discussed in Section 4.2. Another

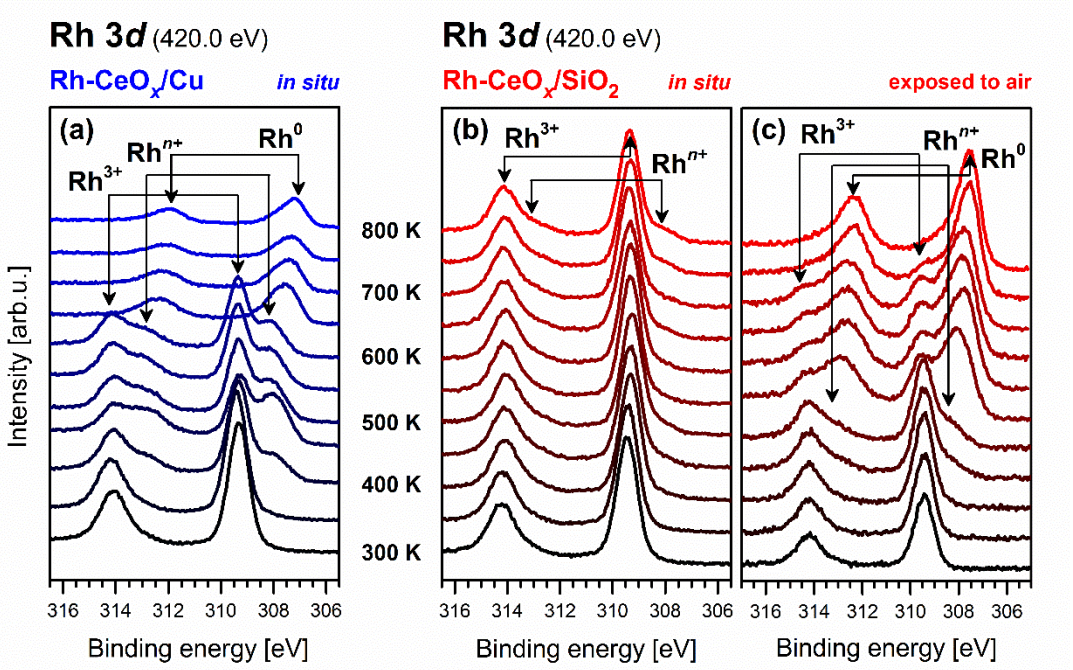

Figure 26: Evolution of the Rh 3*d* spectra during subsequent heating in UHV for the Rh-CeO_x thin films with 5% of rhodium deposited onto the (a) Cu and (b-c) SiO_2 substrates (measured at MSB, Elettra). The films (a) and (b) were investigated *in situ*. The film (c) was prepared in the same way as the film (b) but it was exposed to the air for 24 h prior to heating.

reason for a higher degree of reduction of Rh-CeO_x may be an influence of the surface adsorbates. Traces of water and carbonaceous species were detected at all samples. While pure cerium oxide is relatively inert to these adsorbates at low temperature and pressure, Rh-CeO_x is more reactive which leads to the release of oxygen and the partial reduction of cerium.

In the case of Rh-CeO_x deposited onto copper, a significant reduction of cerium occurs at 400 K. It coincides with the reduction of rhodium and the formation of Rh^{n+} which is apparent from Figure 26 (a). The decomposition of the Rh-O-Ce bonds in the Rh-CeO_x films supported by copper starts at 400 K. After the initial reduction of Rh-CeO_x/Cu at 400 K, the Ce^{4+} concentration increases again (see Figure 25). Simultaneously, the Rh^{n+} intensity grows at the expense of Rh^{3+}. It could be explained by a further decomposition of the Rh-O-Ce bonds and the reduction of rhodium. The released oxygen is spent for oxidizing some of the Ce^{3+} ions. This trend continues up to 650 K. At this temperature, the $D(Ce^{3+})/D(Ce^{4+})$ ratios for CeO_x/Cu and Rh-CeO_x/Cu reach the same value. Simultaneously, Rh^0 state appears in Figure 26 (a). These effects correspond to the total decomposition of the mixed

oxide and the segregation of rhodium and cerium oxide into separate phases. These phases are developed further with the increasing temperature. Rhodium forms larger clusters, while cerium oxide releases its oxygen due to the high temperature, similarly to CeO_x/Cu.

We may notice that the Rh-O-Ce bonds in Rh-CeO_x/Cu are decomposed at a markedly lower temperature (400 K) than the same films deposited onto silica (Rh^{n+} appears above 700 K). This disparity between the two systems is probably caused by a different film-substrate interaction. It is well known that cerium and silicon form cerium silicates in the oxygen rich environment [106, 118, 119]. In the case of cerium oxide thin films supported by Si or SiO_2, the silicates are created due to the migration of silicon atoms into the cerium oxide thin film [50, 104]. We observed the migration of silicon and the formation of cerium silicates at elevated temperatures also at the Rh-CeO_x films. More details about this topic can be found in [113]. Nevertheless, it was reported that silicon-based compounds dispersed in cerium oxide may prevent sintering of ceria and thus, enhance the thermal stability of the systems [33]. It agrees well with the high thermal stability of the Rh-CeO_x films supported by SiO_2.

On the other hand, cerium oxide is not bound strongly to the copper substrate. The interaction between cerium oxide and copper is limited to few layers around the interface [38]. At elevated temperatures, ceria is very mobile, its atoms migrate over the copper substrate and build three-dimensional structures [93]. It is consistent with the observed uncovering of the copper substrate at elevated temperatures and the high reducibility of the Rh-CeO_x supported by Cu.

We showed that the film-substrate interaction affects strongly the reducibility and thermal stability of the Rh-CeO_x films. Hereafter, we will discuss the influence of the surface adsorbates. The Rh 3*d* spectra of subsequently heated Rh-CeO_x/SiO_2 treated *in situ* and exposed to the air before heating are compared in Figure 26 (b) and (c), respectively. As was stated before, the temperature needed for decomposing the Rh-O-Ce bonds, which is accompanied by the appearance of the Rh^{n+} state, is higher than 700 K for the film treated in the UHV conditions. However, the film exposed to the air shows the signs of the decomposition at a significantly lower temperature. Rh^{n+} appears already at 450 K.

The subsequent heating of the Rh-CeO_x film causes further reduction of rhodium. The formation of Rh^{n+} is accompanied by the increase of the resonant

enhancement ratio (Figure 25). Simultaneously, the C 1*s* signal from carbonaceous species, mainly CO [76], decreases (data not shown). These effects can be interpreted by the reaction of carbonaceous species adsorbed at the surface with oxygen released from the Rh-O-Ce bonds. The most significant loss of the carbon intensity occurs between 500 and 550 K. It coincides with the most distinct changes in the Rh 3*d* spectra in Figure 26 (c), i.e. the emergence of the Rh^0 state. When Rh^0 appears, the resonant enhancement ratio begins decreasing again. At 800 K, it reaches the value similar to the pure cerium oxide film treated *in situ*. At the same point, there are no traces of Rh^{3+}. It means that rhodium and cerium oxide segregated into separate phases.

It is interesting to note that the carbonaceous adsorbates influence mainly rhodium but have only a small effect on cerium. Also, we may notice that all Rh-CeO_x films converge to the same state, i.e. the decomposition of the mixed oxide phase. The maximum temperature which can be achieved without decomposing the mixed oxide differs in dependence on the film-substrate interaction. The influence of the environment is also quite strong. The Rh-CeO_x films are stable up to 800 K in the oxidizing environment, such as air, but decompose readily due to the reactions with reductants, e.g. CO. This information is very important for understanding the behaviour of the films under reaction conditions.

4.4 Reactivity of Rh-CeO_x

The reactivity of cerium oxide doped by rhodium principally differs from the reactivity of rhodium particles supported by cerium oxide. In the case of the supported Rh particles, reactions take place at rhodium because it provides adsorption positions for the oxidizing, as well as reducing reactants. But in the case of the doped oxide, the reductants adsorb at electron deficient sites, such as the cations of the dopant, while oxidants adsorb at the electron rich oxygen vacancies in their vicinity [98]. Therefore, it can be expected that the mechanisms for the same reactions are different for doped oxides and supported particles. Furthermore, the oxygen ions bound to the dopants are often very labile and thus, easily available to the reactions [22, 36, 38]. The oxygen storage capacity (OSC) of the doped oxides is often significantly higher than that of pure ceria [32].

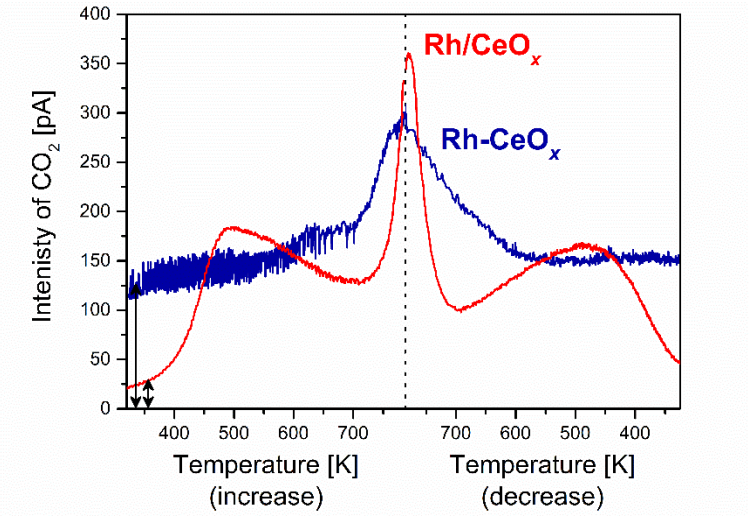

Figure 27: Comparison of CO_2 signals from $CO+O_2$ steady-state reactions on $Rh/CeO_x^{(Ox)}$ (red; Rh particles supported by cerium oxide, 1 ML of Rh, 5th reaction cycle) and $Rh(5\%)\text{-}CeO_x$ (blue; Rh-doped cerium oxide, 2nd reaction cycle). Constant background was subtracted from both curves.

The reaction experiments were focused on CO oxidation because it is a very simple reaction suitable for probing the catalytic activity of the studied systems. CO oxidation at cerium oxide supporting rhodium particles, Rh/CeO_x, proceeds via the Langmuir-Hinshelwood mechanism, as was discussed in Section 3. Both reactants, oxygen and carbon monoxide, must first adsorb onto the Rh particle. Then, CO_{ads} and O_{ads} can react forming CO_2 which desorb immediately. At elevated temperature, oxygen can be supplied from the ceria support by the reversed spillover which enhances the oxidizing ability of the Rh/CeO_x system.

In the case of cerium oxide doped by rhodium, $Rh\text{-}CeO_x$, CO oxidizes by Mars-van Krevelen mechanism [98]. According to McFarland and Metiu [6], CO reacts with a surface oxygen atom forming an $O_{surface}$-CO group. CO molecules bind most strongly to oxygen atoms that are easiest to remove. These are the labile oxygen species from the Rh-O-Ce bonds. The CO_2 molecules formed in this way desorb easily from the surface, leaving behind an oxygen vacancy which is readily filled by O_2. The vacancy donates electrons to the adsorbed O_2 molecule, weakening the O-O bond. Therefore, O_2 adsorbed at the vacancy site reacts readily with CO and forms carbonate which decomposes to CO_2 and oxygen, healing the oxygen vacancy.

A comparison of the CO_2 curves from TPR steady-state reactions is shown in Figure 27. It should be noted that a significantly higher noise in the signal of $Rh\text{-}CeO_x$ was caused electronically, due to the different power supply used for heating

the sample. We can see that the CO_2 signal is relatively constant up to 600 K and increases at higher temperature on Rh-CeO_x. When the heating is switched off, the signal is slowly decreasing until it reaches approximately the same intensity as at the beginning of the reaction.

It is apparent that at low temperatures, the CO_2 production is significantly higher at Rh-CeO_x compared to Rh/CeO_x (see the arrows in Figure 27). It could be taken as an evidence of different reaction mechanisms. While CO can oxidize on Rh/CeO_x only at higher temperatures because the adsorption positions for oxygen are blocked by the CO molecules at low temperatures, the oxidation of CO at Rh-CeO_x can occur even at low temperatures via the Mars-van Krevelen mechanism.

At higher temperatures, both Rh-CeO_x and Rh/CeO_x systems serve as very good catalysts for CO oxidation. In the case of Rh-CeO_x, the increased production of CO_2 at higher temperatures compared to the low temperature region could be explained by a thermal decomposition of the Rh-CeO_x mixed oxide. This is accompanied with a formation of small rhodium particles and a massive release of oxygen which can be spent in the reactions.

The CO_2/CO ratio can be considered as an indicator of the catalyst efficiency for the oxidizing reactions. Therefore, we use it to compare the oxidizing ability of the Rh-CeO_x films. Figure 28 (a) shows the CO_2/CO parameter derived from three consecutive TPR steady-state reactions for Rh-CeO_x with different concentrations of rhodium. The CO_2/CO ratios for the reference CeO_x film and the Rh foil are also included in Figure 28 (a). We can see that the CO_2/CO ratio is generally higher in the 1st TPR cycle and drops in the two following cycles. This difference is caused by major modifications of the Rh-CeO_x films during the first TPR cycle.

When the samples are heated in UHV for the first time, the films undergo a thermal reduction, as was discussed in Section 4.3. Both cerium and rhodium ions are reduced. The reactants do not significantly influence the reduction of the films but they react with the weakly bound oxygen and surface contaminants which is evident from a decrease of the C 1*s* signal, data not shown. The CO_2/CO ratios from the 2nd and 3rd TPR cycles are reproducible within the uncertainty of the measurement indicating that the morphology of the films stabilizes during the first reaction cycle and do not change noticeably in the following cycles.

Figure 28 (b) shows the Rh^{3+}/Rh parameter before the reactions, and after the 1st and 3rd TPR cycles. The decrease of Rh^{3+}/Rh signifies the reduction of rhodium.

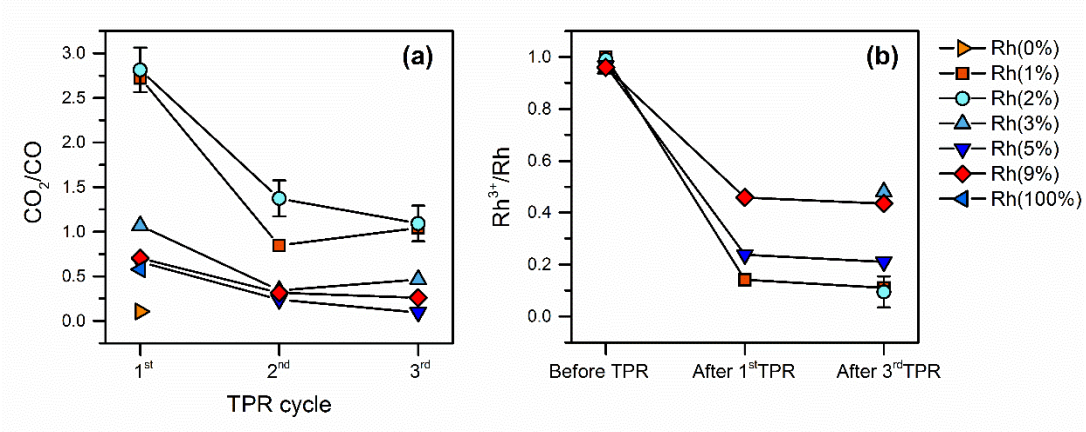

Figure 28: (a) CO_2/CO ratio for three consecutive TPR reaction cycles, (b) development of Rh^{3+}/Rh ratio derived from XPS measured before and after the reactions for the Rh-CeO_x samples with different Rh concentrations (1-9%), the reference Rh foil (100%) and the reference CeO_x film (0%). Rh^{3+}/Rh was calculated as the ratio of the Rh^{3+} area to the area of the Rh 3*d* region.

Reduced rhodium atoms create metal particles at elevated temperature. Silicon substrate partially prevents the sintering but it is still evident from the XPS spectra. Rh 3*d* peaks belonging to Rh^0 shift to lower binding energy which is a sign of the formation of larger particles. This effect is most prominent for the sample Rh(2%)-CeO_x. It coincides well with dramatic changes of its parameters in Figure 28. We can see that the reduction occurs most readily for Rh-CeO_x films with low concentrations of rhodium (1-2%).

The catalytic efficiency for the Rh-CeO_x films with different concentrations of rhodium is compared in Figure 29 (a). Green circles show the CO_2/CO parameter derived from the 2nd TPR cycle for the sputtered films (0-9% of rhodium). The purple circle corresponds to the Rh foil (100% of rhodium), and the orange circle represent the Rh/$CeO_x^{(Ox)}$ from the Section 3. The amount of rhodium in the Rh/$CeO_x^{(Ox)}$ sample was approximately 1 ML. In order to compare this sample with the Rh-doped cerium oxide films, the rhodium concentration was estimated according to equation (10) to approximately 13%.

The oxidizing ability of pure cerium oxide is negligible looking at the small value of CO_2/CO in Figure 29. That is because CO does not adsorb on pure cerium oxide under our experimental conditions as was already shown in Section 3.4. When ceria is doped by rhodium the CO oxidation ability increases rapidly with the increasing concentration of rhodium, reaching the maximum at around 2%. This is a

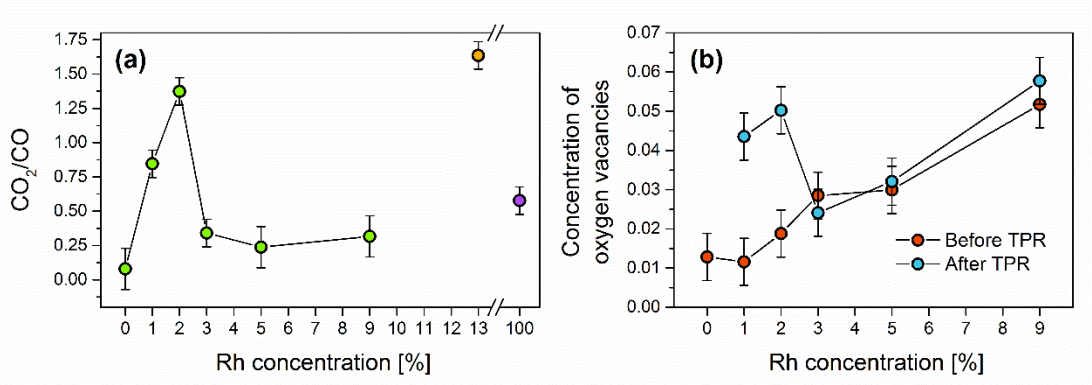

Figure 29: (a) Ratio of the total CO_2 signal to the total CO signal detected during the 2nd TPR reaction cycle for the Rh(0-9%)-CeO_x thin films (green), Rh/$CeO_x^{(Ox)}$ (orange) and the Rh foil (purple). (b) Concentration of oxygen vacancies in near-surface region before (red) and after (blue) TPR reactions for the Rh(0-9%)-CeO_x thin films.

very good result considering a very low amount of rhodium in the system. We can see that the CO oxidation ability of the Rh(1%)-CeO_x and Rh(2%)-CeO_x films is significantly higher compared to that of the Rh foil (purple circle). For higher concentrations of rhodium in the Rh-CeO_x films, the CO_2/CO ratio drops below the value measured for the rhodium foil. Decrease of the CO oxidation ability is probably caused by the suppressed oxygen mobility in the Rh-CeO_x films which will be discussed later.

We can see from Figure 29 (a) that the Rh(2%)-CeO_x and Rh/$CeO_x^{(Ox)}$ samples have similar oxidizing ability (the values of the CO_2/CO ratios are very close) but the reaction mechanisms are different for both systems. Nevertheless, both of these systems exhibit a noticeably higher oxidizing ability than pure rhodium or pure cerium oxide. This clearly demonstrates the efficiency of the combined metal-oxide catalyst.

There are two main factors determining the reactivity of the Rh-CeO_x films. The first is a number of active sites at the surface. It is defined by the structure and the chemical composition of the surface area. The other factor, important especially for oxidizing reactions, is the ability of the Rh-CeO_x system to release the oxygen and transport it from deeper layers to the surface area. It strongly depends on the structure of the thin films.

First, we focus on the active sites at the surface of the Rh-CeO_x films. It was reported that the sites close to rhodium ionic dopant are active for the CO oxidation

[10, 32, 40, 83, 88]. At elevated temperature, the metallic rhodium particles are formed which also offer the active sites for CO oxidation [46]. Furthermore, the oxygen vacancies are also very important for catalytic activity of doped oxides because they can offer additional adsorption or reaction positions. They can be monitored indirectly through the Ce 3*d* spectra. When oxygen is removed from cerium oxide lattice, it leaves behind two electrons to maintain its charge neutrality. These electrons are accommodated in the empty 4*f* states of cerium atoms in vicinity of the oxygen vacancy, reducing two Ce^{4+} ions to Ce^{3+} [59]. Thus, Ce^{3+} ions are indicators of oxygen vacancies in cerium oxide.

If a low-valence metal dopant is present in cerium oxide, oxygen vacancies are formed to maintain the charge neutrality and release the strain in the lattice caused by modifications of bond lengths near the dopant [6, 15, 36, 103]. Additionally, oxygen vacancies may be formed in a direct vicinity of the dopant because the oxygen atoms bound to the dopant are very labile and the oxygen vacancy formation energy is very low [36, 38, 103]. In that case, the excess electrons may be accommodated in the empty or partially filled states of the metal dopant apart from the Ce 4*f* states [6]. Therefore, the Ce^{3+} states are not the only indicators of oxygen vacancies in doped cerium oxides. The dopants must be also taken into consideration when estimating a number of oxygen vacancies.

Figure 29 (b) shows the concentration of oxygen vacancies in the near-surface area before and after TPR reactions. Considering that one oxygen vacancy is accompanied by two Ce^{3+} or Rh^{3+} ions for balancing the charges [39], the concentration of the vacancies was roughly estimated as a half the sum of Ce^{3+} and Rh^{3+} atomic concentrations in the Rh-CeO_x films. The atomic concentrations of Ce^{3+} and Rh^{3+} ions were derived from XPS: the atomic concentrations of cerium and rhodium were weighted by relative concentrations of Ce^{3+} and Rh^{3+} ions to the total signal of cerium and rhodium, Ce^{3+}/Ce or Rh^{3+}/Rh.

We can see from Figure 29 (b) that the concentration of oxygen vacancies before the reactions increases with Rh concentration. As we showed before, cerium oxide itself does not provide adsorption sites for carbon monoxide under our experimental conditions. But rhodium is able to create the adsorption positions for CO at the surface, whether it is in a form of a dopant or a particle. Small number of rhodium can create only few of these positions. Higher concentration of rhodium would result in more adsorption sites.

However, Figure 29 (a) shows that the ability of the Rh-CeO_x films to oxidize CO decreases with growing concentration of rhodium, from approximately 3%. It coincides with the change of the oxygen vacancy concentrations before and after the reactions plotted in Figure 29 (b). We can see that the number of vacancies increased significantly after the reactions for the samples with the low concentration of rhodium (1-2%). On the other hand, the concentration of vacancies remained almost unchanged for the films with the higher amount of rhodium (3-9%). These results can be explained by the different ability of the film to donate oxygen to reactions. The films with the low concentration of rhodium release oxygen readily. On the contrary, the migration of oxygen seems to be suppressed in the films with the higher amount of Rh.

The transport of oxygen towards the adsorption sites is a very important factor for surface reactions. Weakly bound oxygen species exhibit a very high mobility through the ceria-based films [10, 21, 32, 112]. The migration process involves the oxygen vacancies and thus, it is enhanced in defective cerium oxide structure [10, 21, 26, 32, 47, 66, 120]. Their formation may be also boosted by the increasing concentration of rhodium dopants which act as additional defects in the ceria lattice. Grain boundaries are ideal paths for the oxygen transport [32, 47, 83].

According to Figure 18 (a), the crystal grains become gradually smaller with the increasing concentration of rhodium as the films grow more and more amorphous. The oxygen migration is probably suppressed by the amorphous-like structure of the films. The oxygen TPR signal shows that only up to 8% of oxygen from the molecular beam is spent for the CO oxidation. The majority of oxygen consumed during the reactions originates from the Rh-CeO_x films. Therefore, the decrease of the CO_2/CO production for the films with higher concentration of rhodium is most probably caused by the insufficient transport of oxygen to the surface area.

The participation of oxygen from the Rh-CeO_x film in the CO oxidation is also apparent from the XPS spectra. Figures 30 (a)-(c) show the O 1*s*, Rh 3*d* and Ce 3*d* regions of the Rh(2%)-CeO_x sample before, and after the TPR reactions. The arrows in the graphs indicate the changes of spectral features. We can see that the O_{Rh} and O_{Def} components in the O 1*s* spectra (designated in Figure 15) decreased. Furthermore, both cerium and rhodium became partially reduced. These effects can be explained by the release of oxygen from the Rh-CeO_x film.

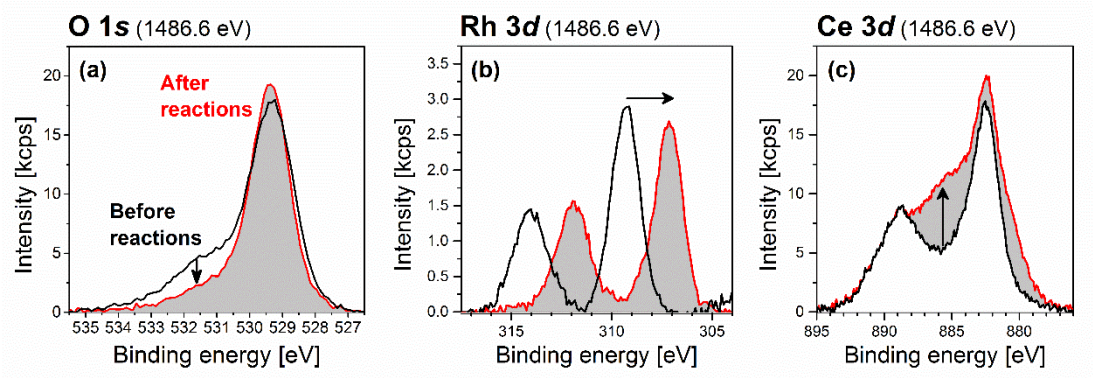

Figure 30: (a) O 1*s*, (b) Rh 3*d*, and (c) Ce 3*d* XPS spectra before (black and white) and after (red and grey) the TPR experiments for Rh(2%)-CeO_x.

The decrease of the O_{Rh} component and the partial reduction of rhodium and cerium ions suggest that the oxygen from the Rh-O-Ce bonds is spent in the surface reactions. The O_{Def} component arises from the weakly bound and highly mobile oxygen species in cerium oxide which signifies that these species also participate in the reactions. The reduction of cerium and rhodium ions is caused by an accommodation of the electrons left behind by oxygen released from bonding to the neighbours [6, 39]. These results support the existence of the Rh-O-Ce bonds in the sputtered ceria films doped by rhodium which was formerly reported for the Rh-CeO_x mixed oxide systems prepared by chemical deposition methods [20, 35, 40, 42].

As was discussed above, the number of active sites at the surface and the oxygen transfer from deeper layers to the surface area are very important for the catalytic activity of the system. We showed that these parameters are strongly dependent on the concentration of rhodium in the Rh-CeO_x sputtered thin films. This result is very interesting from the viewpoint of designing a catalyst with specific properties. Reaching the desired properties can be achieved by tuning the concentration of the Rh dopant in the cerium oxide thin film.

5 Summary

The presented thesis reports on systems containing rhodium and cerium oxide. Two types of systems were investigated by means of the photoelectron spectroscopy and the temperature programmed reactions: (I) the rhodium particles supported by the cerium oxide thin films (Rh/CeO_x), and (II) the cerium oxide thin films doped by rhodium (Rh-CeO_x).

(I) Rh/CeO_x

The systems consisting of the rhodium particles supported on cerium oxide exhibited the electronic metal-substrate interaction. Our experiments with the deposition of rhodium onto the cerium oxide support with various degrees of reduction suggested that there is a charge transfer between the Rh particles and the CeO_x support. The direction of the charge transfer depended on the degree of cerium oxide reduction.

For CeO_x with x between 2.00 and 1.93, the deposition of rhodium induced the reduction of cerium ions Ce^{4+} to Ce^{3+}. It is a result of an electron transfer from the rhodium adatom to the cerium oxide support. On the contrary, the deposition of rhodium onto cerium oxide with a higher degree of reduction (x between 1.93 and 1.67) caused a partial oxidation of cerium oxide. It can be interpreted by an electron transfers from Ce^{3+} to the Rh adatom, leading to oxidizing the Ce^{3+} ion to Ce^{4+} and a build-up of the negative charge on the Rh deposit. These experimental results and interpretations were supported by calculations based on the density functional theory

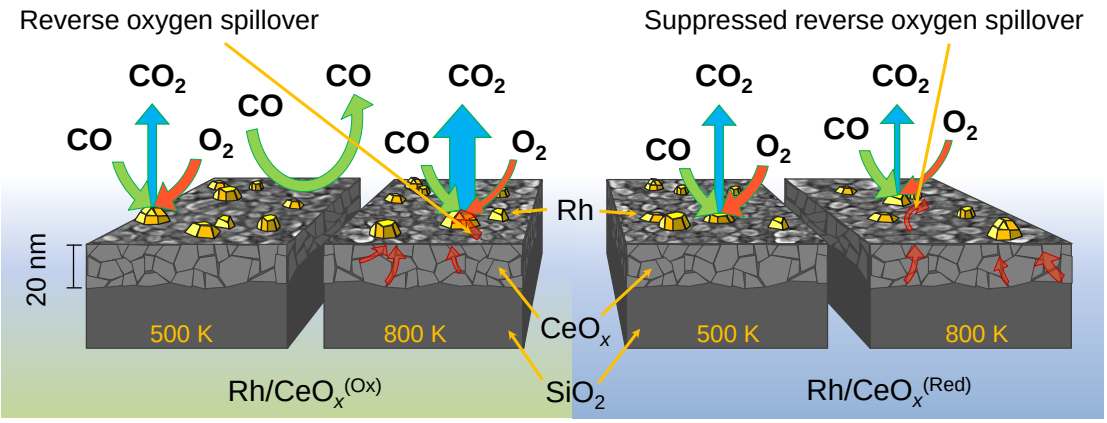

Figure 31: Schematic illustration of the reactivity of Rh/$CeO_x^{(Ox)}$ ($1.93 < x < 2.00$) and Rh/$CeO_x^{(Red)}$ ($1.67 < x < 1.93$) at 500 and 800 K.

performed by Dr Lucie Szabová.

Furthermore, we show that the electronic metal-support interaction has a tremendous impact on the reactivity. The CO oxidation on the Rh/CeO_x system is illustrated in Figure 31 for Rh/$CeO_x^{(Ox)}$ and Rh/$CeO_x^{(Red)}$. These systems had different types of the electronic metal-substrate interaction. The reactivity of both systems differed at higher temperatures, around 800 K. At this temperature, the cerium oxide films released a high amount of oxygen. The reverse oxygen spillover onto the Rh particles was allowed on the Rh/$CeO_x^{(Ox)}$ system but was suppressed on Rh/$CeO_x^{(Red)}$ because of the net negative charge on rhodium. Therefore, the CO_2 production at high temperatures was much higher on Rh/$CeO_x^{(Ox)}$ compared to the Rh/$CeO_x^{(Red)}$.

(II) Rh-CeO_x

Doping the cerium oxide thin films by rhodium had a tremendous impact on their properties. The morphology and the oxidizing ability of the Rh-CeO_x films with various concentrations of rhodium are illustrated in Figure 32.

The CO oxidation on pure cerium oxide in the UHV conditions was negligible because CO did not adsorb on the surface. Rh dopants provided adsorption positions for the reactant. Therefore, all Rh-CeO_x films exhibited the higher oxidizing ability than pure cerium oxide. However, their properties strongly depended on the concentration of the dopant.

The films with low concentrations of rhodium (1-2%) were composed of small crystallites and exhibited a high reducibility and oxidizing ability. The concentrations of the rhodium dopant was different in the near surface area and deep laying regions due to the segregation of rhodium towards the surface. The chemical

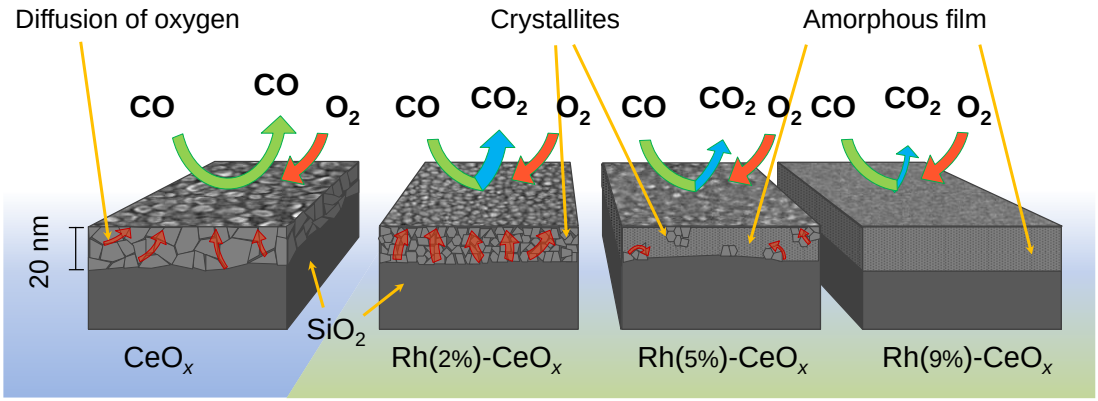

Figure 32: Schematic illustration of the structure and reactivity of the Rh-CeO_x films.

states of rhodium also differed in dependence on the depth from the surface. While, rhodium favoured the Rh^{3+} state at the surface area, it was present in Rh^{3+} and Rh^{n+} states in the deeper layers of the films. The Rh^{n+} species were assigned to highly dispersed rhodium atoms or ions with a lower valency compared to Rh^{3+}.

On the contrary, the Rh-CeO_x films with higher concentrations of rhodium (3-9%) are more or less homogeneous and amorphous. Their oxidizing ability is limited because of the suppressed mobility of oxygen through the films.

We showed that it is possible to tune the properties of the rhodium-cerium oxide based systems, both (I) and (II), during their preparations. Altering the degree of cerium oxide reduction before the rhodium deposition leads to establishing various electronic metal-substrate interactions between rhodium and cerium oxide at Rh/CeO_x. On the other hand, the concentration of the rhodium dopant in the cerium oxide thin film influences the oxygen mobility in Rh-CeO_x. We showed that these effects have a tremendous impact on the oxidizing ability of the systems. We consider these results very interesting because they can be useful for designing a catalyst with desired properties applicable for specific reactions.

References

[1] MURAKI, H and ZHANG, G. Design of advanced automotive exhaust catalysts. *Catal. Today*. 2000. Vol. 63, no. 2-4, p. 337–345.

[2] MIYAZAWA, T, KIMURA, T, NISHIKAWA, J, KUNIMORI, K and TOMISHIGE, K. Catalytic properties of $Rh/CeO_2/SiO_2$ for synthesis gas production from biomass by catalytic partial oxidation of tar. *Sci. Technol. Adv. Mater*. 2005. Vol. 6, no. 6, p. 604–614.

[3] BRUIX, A, LYKHACH, Y, MATOLÍNOVÁ, I, NEITZEL, A, SKÁLA, T, TSUD, N, VOROKHTA, M, STETSOVYCH, V, ŠEVČÍKOVÁ, K, MYSLIVEČEK, J, FIALA, R, VÁCLAVŮ, M, PRINCE, KC, BRUYÈRE, S, POTIN, V, ILLAS, F, MATOLÍN, V, LIBUDA, J and NEYMAN, KM. Maximum noble-metal efficiency in catalytic materials: Atomically dispersed surface platinum. *Angew. Chemie - Int. Ed.* 2014. Vol. 53, p. 10525–10530.

[4] VAYSSILOV, GN, LYKHACH, Y, MIGANI, A, STAUDT, T, PETROVA, GP, TSUD, N, SKÁLA, T, BRUIX, A, ILLAS, F, PRINCE, KC, MATOLÍN, V, NEYMAN, KM and LIBUDA, J. Support nanostructure boosts oxygen transfer to catalytically active platinum nanoparticles. *Nat. Mater.* 2011. Vol. 10, no. 4, p. 310–315.

[5] BARBIER JR, J and DUPREZ, D. Steam effects in three-way catalysis. *Appl. Catal. B Environ.* 1994. Vol. 4, no. 2-3, p. 105–140.

[6] MCFARLAND, EW and METIU, H. Catalysis by doped oxides. *Chem. Rev.* 2013. Vol. 113, no. 6, p. 4391–4427.

[7] BOARO, M, VICARIO, M, DE LEITENBURG, C, DOLCETTI, G and TROVARELLI, A. The use of temperature-programmed and dynamic/transient methods in catalysis: characterization of ceria-based, model three-way catalysts. *Catal. Today*. 2003. Vol. 77, no. 4, p. 407–417.

[8] TROVARELLI, A, DE LEITENBURG, C, BOARO, M and DOLCETTI, G. The utilization of ceria in industrial catalysis. *Catal. Today*. 1999. Vol. 50, no. 2, p. 353–367.

[9] KAŠPAR, J, FORNASIERO, P and GRAZIANI, M. Use of CeO_2-based oxides in the three-way catalysis. *Catal. Today*. 1999. Vol. 50, no. 2, p. 285–298.

[10] ROYER, S and DUPREZ, D. Catalytic Oxidation of Carbon Monoxide over Transition Metal Oxides. *ChemCatChem*. 2011. Vol. 3, no. 1, p. 24–65.

[11] MATOLÍN, V, CABALA, M, MATOLÍNOVÁ, I, ŠKODA, M, VÁCLAVŮ, M, PRINCE, KC, SKÁLA, T, MORI, T, YOSHIKAWA, H, YAMASHITA, Y, UEDA, S and KOBAYASHI, K. Pt and Sn Doped Sputtered CeO_2 Electrodes for Fuel Cell Applications. *Fuel Cells*. 2010. Vol. 10, no. 1, p. 139–144.

[12] GANDHI, HS, GRAHAM, GW and MCCABE, RW. Automotive exhaust catalysis. *J. Catal.* 2003. Vol. 216, no. 1-2, p. 433–442.

[13] ZAFIRIS, G and GORTE, RJ. Evidence for Low-Temperature Oxygen Migration from Ceria to Rh. *J. Catal*. 1993. Vol. 139, no. 2, p. 561–567.

[14] CAMPBELL, CT. Catalyst-support interactions: Electronic perturbations. *Nat. Chem*. 2012. Vol. 4, no. 8, p. 597–598.

[15] PACCHIONI, G. Electronic interactions and charge transfers of metal atoms and clusters on oxide surfaces. *Phys. Chem. Chem. Phys*. 2013. Vol. 15, no. 6, p. 1737–1757.

[16] SKÁLA, T, TSUD, N, PRINCE, KC and MATOLÍN, V. Bimetallic bonding and mixed oxide formation in the Ga–Pd–CeO_2 system. *J. Appl. Phys.* 2011. Vol. 110, no. 4, p. 043726 (6pp).

[17] ŠKODA, M, CABALA, M, MATOLÍNOVÁ, I, PRINCE, KC, SKÁLA, T, ŠUTARA, F, VELTRUSKÁ, K and MATOLÍN, V. Interaction of Au with CeO_2(111): A photoemission study. *J. Chem. Phys.* 2009. Vol. 130, no. 3, p. 034703 (7pp).

[18] LU, Z and YANG, Z. Interfacial properties of NM/CeO_2(111) (NM = noble metal atoms or clusters of Pd, Pt and Rh): a first principles study. *J. Phys. Condens. Matter*. 2010. Vol. 22, no. 47, p. 475003 (10pp).

[19] SZABOVÁ, L, SKÁLA, T, MATOLÍNOVÁ, I, FABRIS, S, FARNESI CM and MATOLÍN, V. Copper-ceria interaction: A combined photoemission and DFT study. *Appl. Surf. Sci.* 2013. Vol. 267, p. 12–16.

[20] MIYAZAWA, T, OKUMURA, K, KUNIMORI, K and TOMISHIGE, K. Promotion of Oxidation and Reduction of Rh Species by Interaction of Rh and CeO_2 over Rh/CeO_2/SiO_2. *J. Phys. Chem. C*. 2008. Vol. 112, no. 7, p. 2574–2583.

[21] FERRIZZ, RM, EGAMI, T and VOHS, JM. Temperature programmed desorption study of the reaction of C_2H_4 and CO on Rh supported on α-Al_2O_3(0001), YSZ(100) and CeO_2 thin films. *Surf. Sci*. 2000. Vol. 465, no. 1-2, p. 127–137.

[22] CUNNINGHAM, J, HICKEY, NJ, CATALUNA, R, CONESA, JC., SORIA, J and MARTINEZ-ARIAS, A. Interfacial RhO_x/CeO_2 sites as locations for low temperature N_2O dissociation. *Stud. Surf. Sci. Catal.* 1996. Vol. 101, p. 681–690.

[23] STUBENRAUCH, J and VOHS, JM. Interaction of CO with Rh Supported on Stoichiometric and Reduced CeO_2(111) and CeO_2(100) Surfaces. *J. Catal.* 1996. Vol. 159, no. 1, p. 50–57.

[24] KUNDAKOVIC, LJ, MULLINS, DR and OVERBURY, SH. Adsorption and reaction of H_2O and CO on oxidized and reduced Rh/CeO_x(111) surfaces. *Surf. Sci*. 2000. Vol. 457, no. 1-2, p. 51–62.

[25] BUNLUESIN, T, CORDATOS, H and GORTE, R.J. Study of CO Oxidation Kinetics on Rh/Ceria. *J. Catal*. 1995. Vol. 157, no. 1, p. 222–226.

[26] CORDATOS, H, BUNLUESIN, T, STUBENRAUCH, J, VOHS, JM and GORTE, RJ. Effect of Ceria Structure on Oxygen Migration for Rh/Ceria Catalysts. *J. Phys. Chem.* 1996. Vol. 100, no. 2, p. 785–789.

[27] MULLINS, DR and OVERBURY, SH. CO Dissociation on Rh Deposited on Reduced Cerium Oxide Thin Films. *J. Catal.* 1999. Vol. 188, no. 2, p. 340–345.

[28] MIGANI, A, VAYSSILOV, GN, BROMLEY, ST, ILLAS, F and NEYMAN, KM. Greatly facilitated oxygen vacancy formation in ceria nanocrystallites. *Chem. Commun.* 2010. Vol. 46, no. 32, p. 5936–5938.

[29] MATOLÍN, V, LIBRA, J, MATOLÍNOVÁ, I, NEHASIL, V, SEDLÁČEK, L and ŠUTARA, F. Growth of ultra-thin cerium oxide layers on Cu(111). *Appl. Surf. Sci.* 2007. Vol. 254, no. 1, p. 153–155.

[30] HAVIAR, S, DUBAU, M, LAVKOVÁ, J, KHALAKHAN, I, POTIN, V, MATOLÍN, V and MATOLÍNOVÁ, I. Investigation of Growth Mechanism of Thin Sputtered Cerium Oxide Films on Carbon Substrates. *Sci. Adv. Mater*. 2014. Vol. 6, no. 6, p. 1278–1285.

[31] DUCHOŇ, T, DVOŘÁK, F, AULICKÁ, M, STETSOVYCH, V, VOROKHTA, M, MAZUR, D, VELTRUSKÁ, K, SKÁLA, T, MYSLIVEČEK, J, MATOLÍNOVÁ, I and MATOLÍN, V. Ordered phases of reduced ceria as epitaxial films on Cu(111). *J. Phys. Chem. C*. 2014. Vol. 118, no. 1, p. 357–365.

[32] BOARO, M, DE LEITENBURG, C, DOLCETTI, G and TROVARELLI, A. The Dynamics of Oxygen Storage in Ceria–Zirconia Model Catalysts Measured by CO Oxidation under Stationary and Cycling Feedstream Compositions. *J. Catal.* 2000. Vol. 193, no. 2, p. 338–347.

[33] ROCCHINI, E, VICARIO, M, LLORCA, J, DE LEITENBURG, C, DOLCETTI, G and TROVARELLI, A. Reduction and oxygen storage behavior of noble metals supported on silica-doped ceria. *J. Catal.* 2002. Vol. 211, no. 2, p. 407–421.

[34] TSCHÖPE, A and YING, JY. The effects of non-stoichiometry and dopants in nanocrystalline cerium oxide-based catalysts on redox reactions. *Nanostructured Mater.* 1995. Vol. 6, no. 5-8, p. 1005–1008.

[35] GAYEN, A, PRIOLKAR, KR, SARODE, PR, JAYARAM, V, HEGDE, MS, SUBBANNA, GN and EMURA, S. $Ce_{1-x}Rh_xO_{2-\delta}$ Solid Solution Formation in Combustion-Synthesized Rh/CeO_2 Catalyst Studied by XRD, TEM, XPS, and EXAFS. *Chem. Mater.* 2004. Vol. 16, no. 11, p. 2317–2328.

[36] NOLAN, M, VERDUGO, VS and METIU, H. Vacancy formation and CO adsorption on gold-doped ceria surfaces. *Surf. Sci.* 2008. Vol. 602, no. 16, p. 2734–2742.

[37] CAMELLONE, MF and FABRIS, S. Reaction mechanisms for the CO oxidation on Au/CeO_2 catalysts: Activity of substitutional Au^{3+}/Au^{+} cations and deactivation of supported Au^{+} adatoms. *J. Am. Chem. Soc.* 2009. Vol. 131, no. 30, p. 10473–10483.

[38] SZABOVÁ, L, CAMELLONE, M F, HUANG, M, MATOLÍN, V and FABRIS, S. Thermodynamic, electronic and structural properties of Cu/CeO_2 surfaces and interfaces from first-principles DFT+U calculations. *J. Chem. Phys.* 2010. Vol. 133, no. 23, p. 234705 (11pp).

[39] YANG, Z, LUO, G, LU, Z, WOO, TK and HERMANSSON, K. Structural and electronic properties of NM-doped ceria (NM = Pt, Rh): a first-principles study. *J. Phys. Condens. Matter*. 2008. Vol. 20, no. 3, p. 035210 (7pp).

[40] MIZOGUCHI, H, ZAKHAROV, LN, BHUVANESH, NSP, SLEIGHT, AW and SUBRAMANIAN, MA. Synthesis and crystal structure of two new cerium rhodium oxides: $Ce_{2/3-x}Rh^{3+}{}_2O_4$ (x∼0.12) with Ce mixed valency and $Ce^{4+}Rh^{3+}{}_2O_5$. *J. Solid State Chem.* 2011. Vol. 184, no. 6, p. 1381–1386.

[41] SHAPLYGIN, IS, PROSYCHEV, II and LAZAREV, VB. The Chemistry and Properties of Complex Oxides of Rhodium. *Russ. J. Inorg. Chem.* 1986. Vol. 31, no. 11, p. 1649–1652.

[42] HOSOKAWA, S, TANIGUCHI, M, UTANI, K, KANAI, H and IMAMURA, S. Affinity order among noble metals and CeO_2. *Appl. Catal. A Gen*. 2005. Vol. 289, no. 2, p. 115–120.

[43] MATOLÍN, V, MATOLÍNOVÁ, I, VÁCLAVŮ, M, KHALAKHAN, I, VOROKHTA, M, FIALA, R, PÍŠ, I, SOFER, Z, POLTIEROVÁ-VEJPRAVOVÁ, J, MORI, T, POTIN, V, YOSHIKAWA, H, UEDA, S and KOBAYASHI, K. Platinum-doped CeO_2 thin film catalysts prepared by magnetron sputtering. *Langmuir*. 2010. Vol. 26, no. 15, p. 12824–12831.

[44] KHALAKHAN, I, VOROKHTA, M, CHUNDAK, M and MATOLÍN, V. Au-CeO_2 nanoporous films/carbon nanotubes composites prepared by magnetron sputtering. *Appl. Surf. Sci.* [online]. 2013. Vol. 267, p. 150–153.

[45] BERNAL, S, CALVINO, JJ, CAUQUI, MA, PÉREZ OMIL, JA, PINTADO, JM and RODRÍGUEZ-IZIQUIRDO, JM. Image simulation and experimental HREM study of the metal dispersion in Rh/CeO_2 catalysts. Influence of the reduction/reoxidation conditions. *Appl. Catal. B Environ.* 1998. Vol. 16, no. 2, p. 127–138.

[46] ŠEVČÍKOVÁ, K, KOLÁŘOVÁ, T, SKÁLA, T, TSUD, N, VÁCLAVŮ, M, LYKHACH, Y, MATOLÍN, V and NEHASIL, V. Impact of Rh–CeO_x interaction on CO oxidation mechanisms. *Appl. Surf. Sci.* 2015. Vol. 332, p. 747–755.

[47] HOLGADO, JP, MUNUERA, G, ESPINÓS, JP and GONZÁLEZ-ELIPE, AR. XPS study of oxidation processes of CeO_x defective layers. *Appl. Surf. Sci.* 2000. Vol. 158, no. 1-2, p. 164–171.

[48] NEHASIL, V, ŠEVČÍKOVÁ, K and ZAHORANOVÁ, T. Photoemission and thermo-programmed reaction study of the catalytic properties of Rh/CeO_2 system. *Surf. Interface Anal.* 2010. Vol. 42, no. 6-7, p. 931–934.

[49] PASCHOAL, JOA., KLEYKAMP, H and THÜMMLER, F. The constitution of the Ru–Rh system. *J. Less Common Met.* 1984. Vol. 98, no. 2, p. 279–284.

[50] VOROKHTA, M, MATOLÍNOVÁ, I, DUBAU, M, HAVIAR, S, KHALAKHAN, I, ŠEVČÍKOVÁ, K, MORI, T, YOSHIKAWA, H and MATOLÍN, V. HAXPES study of CeO_x thin film–silicon oxide interface. *Appl. Surf. Sci.* 2014. Vol. 303, p. 46–53.

[51] ZAHORANOVÁ, T, MORI, T, YAN, P, ŠEVČÍKOVÁ, K, VÁCLAVŮ, M, MATOLÍN, V and NEHASIL, V. Study of the character of gold nanoparticles deposited onto sputtered cerium oxide layers by deposition-precipitation method: Influence of the preparation parameters. *Vacuum*. 2015. Vol. 114, p. 86–92.

[52] SCOFIELD, JH. *Lawrance Livermore Laboratory Report UCRL-51326*. Livermore, CA, 1973.

[53] TANUMA, S, POWELL, CJ and PENN, DR. Calculations of electron inelastic mean free paths. VIII. Data for 15 elemental solids over the 50-2000 eV range. *Surf. Interface Anal.* 2005. Vol. 37, no. 1, p. 1–14.

[54] NEHASIL, V, STARÁ, I and MATOLÍN, V. Study of CO desorption and dissociation on Rh surfaces. *Surf. Sci.* 1995. Vol. 331-333, p. 105–109.

[55] KOBATA, M, PÍŠ, I, IWAI, H, YAMAZUI, H, TAKAHASHI, H, SUZUKI, M, MATSUDA, H, DAIMON, H and KOBAYASHI, K. Development of the Hard-X-ray Angle Resolved X-ray Photoemission Spectrometer for Laboratory Use. *Anal. Sci.* 2010. Vol. 26, no. 2, p. 227–232.

[56] LANGFORD, JI AND WILSON, AJC. Seherrer after Sixty Years: A Survey and Some New Results in the Determination of Crystallite Size. *J. Appl. Cryst.* 1978. Vol. 11, p. 102–113.

[57] FABRIS, S, DE GIRONCOLI, S, BARONI, S, VICARIO, G and BALDUCCI, G. Taming multiple valency with density functionals : *Phys. Rev. B*. 2005. Vol. 71, p. 041102 (4pp).

[58] DA SILVA, JLF, GANDUGLIA-PIROVANO, MV, SAUER, J, BAYER, V and KRESSE, G. Hybrid functionals applied to rare-earth oxides: The example of ceria. *Phys. Rev. B*. 2007. Vol. 75, no. 4, p. 045121 (10pp).

[59] FABRIS, S, VICARIO, G, BALDUCCI, G, DE GIRONCOLI, S and BARONI, S. Electronic and atomistic structures of clean and reduced ceria surfaces. *J. Phys. Chem. B* [online]. 2005. Vol. 109, no. 48, p. 22860–7.

[60] BAGUS, PS, ILTON, ES and NELIN, CJ. The interpretation of XPS spectra: Insights into materials properties. *Surf. Sci. Rep.* 2013. Vol. 68, no. 2, p. 273–304.

[61] YANG, Z, WOO, TK, BAUDIN, M and HERMANSSON, K. Atomic and electronic structure of unreduced and reduced CeO_2 surfaces: a first-principles study. *J. Chem. Phys.* 2004. Vol. 120, no. 16, p. 7741–7749.

[62] FUJIMORI, A. Correlation effects in the electronic structure and photoemission spectra of mixed-valence cerium compounds. *Phys. Rev. B.* 1983. Vol. 28, no. 8, p. 4489–4499.

[63] KOTANI, A, MIZUTA, H, JO, T and PARLEBAS, JC. Theory of core photoemission spectra in CeO_2. *Solid State Commun.* 1985. Vol. 53, no. 9, p. 805–810.

[64] CAFUN, JD, KVASHNINA, K., CASALS, E, PUNTES, V. and GLATZEL, P. Absence of Ce^{3+} sites in chemically active colloidal ceria nanoparticles. *ACS Nano*. 2013. Vol. 7, no. 12, p. 10726–10732.

[65] MATSUMOTO, M, SODA, K, ICHIKAWA, K, TANAKA, S, TAGUCHI, Y, JOUDA, K, AITA, O, TEZUKA, Y and SHIN, S. Resonant photoemission study of CeO_2. *Phys. Rev. B.* 1994. Vol. 50, no. 16, p. 11340–11346.

[66] MULLINS, DR, OVERBURY, SH and HUNTLEY, DR. Electron spectroscopy of single crystal and polycrystalline cerium oxide surfaces. *Surf. Sci*. 1998. Vol. 409, no. 2, p. 307–319.

[67] PFAU, A and SCHIERBAUM, KD. The electronic structure of stoichiometric and reduced CeO_2 surfaces: an XPS, UPS and HREELS study. *Surf. Sci.* 1994. Vol. 321, no. 1-2, p. 71–80.

[68] WUILLOUD, E, DELLEY, B, SCHNEIDER, WD and BAER, Y. Spectroscopic evidence for localized and extended f-symmetry states in CeO_2. *Phys. Rev. Lett.* 1984. Vol. 53, no. 2, p. 202–205.

[69] ROMEO, M, BAK, K, EL FALLAH, J, LE NORMAND, F and HILAIRE, L. XPS Study of the reduction of cerium dioxide. *Surf. Interface Anal.* 1993. Vol. 20, no. 6, p. 508–512.

[70] BRIGGS, D and GRANT, JT. *Surface Analysis by Auger and X-Ray Photoelectron Spectroscopy*. Trowbridge, UK : IM Publications and SurfaceSpectra Limited, 2003. ISBN 1901019047.

[71] BURROUGHS, P, HAMNETT, A, ORCHARD, AF and THORNTON, G. Satellite structure in the X-ray photoelectron spectra of some binary and mixed oxides of lanthanum and cerium. *J. Chem. Soc. Dalt. Trans.* 1976. No. 17, p. 1686.

[72] SKÁLA, T, ŠUTARA, F, ŠKODA, M, PRINCE, KC and MATOLÍN, V. Palladium interaction with CeO_2, Sn-Ce-O and Ga-Ce-O layers. *J. Phys. Condens. Matter*. 2009. Vol. 21, no. 5, p. 055005 (9pp).

[73] LARACHI, F, PIERRE, J, ADNOT, A and BERNIS, A. Ce 3*d* XPS study of composite $Ce_xMn_{1-x}O_{2-y}$ wet oxidation catalysts. *Appl. Surf. Sci.* 2002. Vol. 195, p. 236–250.

[74] MATOLÍN, V, MATOLÍNOVÁ, I, SEDLÁČEK, L, PRINCE, KC and SKÁLA, T. A resonant photoemission applied to cerium oxide based nanocrystals. *Nanotechnology*. 2009. Vol. 20, no. 21, p. 215706 (7pp).

[75] SKÁLA, T, ŠUTARA, F, CABALA, M, ŠKODA, ML, PRINCE, KC and MATOLÍN, V. A photoemission study of the interaction of Ga with CeO_2(111) thin films. *Appl. Surf. Sci.* 2008. Vol. 254, no. 21, p. 6860–6864.

[76] LYKHACH, Y, NEITZEL, A, ŠEVČÍKOVÁ, K, JOHÁNEK, V, TSUD, N, SKÁLA, T, PRINCE, KC, MATOLÍN, V and LIBUDA, J. The mechanism of hydrocarbon oxygenate reforming: C-C bond scission, carbon formation, and noble-metal-free oxide catalysts. *ChemSusChem*. 2014. Vol. 7, no. 1, p. 77–81.

[77] MATOLÍN, V, CABALA, M, CHÁB, V, MATOLÍNOVÁ, I, PRINCE, KC., ŠKODA, M, ŠUTARA, F, SKÁLA, T and VELTRUSKÁ, K. A resonant photoelectron spectroscopy study of SnO_x doped CeO_2 catalysts. *Surf. Interface Anal.*. 2008. Vol. 40, no. 3-4, p. 225–230.

[78] ECK, S, CASTELLARIN-CUDIA, C, SURNEV, S, RAMSEY, MG and NETZER, FP. Growth and thermal properties of ultrathin cerium oxide layers on Rh(111). *Surf. Sci.* 2002. Vol. 520, no. 3, p. 173–185.

[79] TSUD, N, BERCHA, S, ACRES, RG, VOROKHTA, M, KHALAKHAN, I, PRINCE, KC and MATOLÍN, V. Functionalization of nanostructured cerium oxide films with histidine. *Phys. Chem. Chem. Phys.* 2015. Vol. 17, no. 4, p. 2770–2777.

[80] WAGNER, CD, RIGGS, WM, DAVIS, LE and MOULDER, JF. *Handbook of X-ray Photoelectron Spectroscopy*. 1979. Minnesota, USA : Perkin-Elmer Corporation. ISBN 9780964812413.

[81] TSUD, N, SKÁLA, T, MAŠEK, K, HANYŠ, P, TAKAHASHI, M, SUGA, H, MORI, T, YOSHIKAWA, H, YOSHITAKE, M, KOBAYASHI, K and MATOLÍN, V. Photoemission study of the tin doped cerium oxide thin films prepared by RF magnetron sputtering. *Thin Solid Films*. 2010. Vol. 518, no. 8, p. 2206–2209.

[82] MATOLÍN, V, MATOLÍNOVÁ, I, DVOŘÁK, F, JOHÁNEK, V, MYSLIVEČEK, J, PRINCE, KC, SKÁLA, T, STETSOVYCH, O, TSUD, N, VÁCLAVŮ, M and ŠMÍD, B. Water interaction with CeO_2(111)/Cu(111) model catalyst surface. *Catal. Today*. 2012. Vol. 181, no. 1, p. 124–132.

[83] FORCE, C, ROMÁN, E, GUIL, JM and SANZ, J. XPS and 1H NMR study of thermally stabilized Rh/CeO_2 catalysts submitted to reduction/oxidation treatments. *Langmuir*. 2007. Vol. 23, no. 8, p. 4569–4574.

[84] LYKHACH, Y, JOHÁNEK, V, ALEKSANDROV, HA, KOZLOV, SM, HAPPEL, M, SKÁLA, T, PETKOV, PST, TSUD, N, VAYSSILOV, GN, PRINCE, KC, NEYMAN, KM, MATOLÍN, V and LIBUDA, J. Water Chemistry on Model Ceria and Pt/Ceria Catalysts. *J. Phys. Chem. C*. 2012. Vol. 116, no. 22, p. 12103–12113.

[85] ŠKODA, M, CABALA, M, MATOLÍNOVÁ, I, SKÁLA, T, VELTRUSKÁ, K and MATOLÍN, V. A photoemission study of the ceria and Au-doped ceria/Cu(111) interfaces. *Vacuum*. 2009. Vol. 84, no. 1, p. 8–12.

[86] PFAU, A, SCHIERBAUM, KD and GÖPEL, W. The electronic structure of CeO_2 thin films: the influence of Rh surface dopants. *Surf. Sci*. 1995. Vol. 331-333, p. 1479–1485.

[87] ZHOU, J, BADDORF, AP, MULLINS, DR and OVERBURY, SH. Growth and characterization of Rh and Pd nanoparticles on oxidized and reduced CeO_x(111) thin films by scanning tunneling microscopy. *J. Phys. Chem. C*. 2008. Vol. 112, no. 25, p. 9336–9345.

[88] CUNNINGHAM, J, HICKEY, NJ, FARRELL, F, BOWKER, M and WEEKS, C. $NO + CO \rightarrow 1/2N_2 + CO_2$ differentiated from $2NO + CO \rightarrow N_2O + CO_2$ over rhodia/ceria catalysts using $^{15}N^{18}O$ and $^{13}C^{16}O$ reactants or time- resolution of products. *Stud. Surf. Sci. Catal.* 1998. Vol. 116, p. 409–418.

[89] STAUDT, T, LYKHACH, Y, TSUD, N, SKÁLA, T, PRINCE, KC, MATOLÍN, V and LIBUDA, J. Ceria reoxidation by CO_2: A model study. *J. Catal.* 2010. Vol. 275, no. 1, p. 181–185.

[90] SADI, F, DUPREZ, D, GÉRARD, F and MILOUDI, A. Hydrogen formation in the reaction of steam with Rh/CeO_2 catalysts: a tool for characterising reduced centres of ceria. *J. Catal.* 2003. Vol. 213, no. 2, p. 226–234.

[91] WANG, Y-G, YOON, Y, GLEZAKOU, V-A, LI, J and ROUSSEAU, R. The role of reducible oxide-metal cluster charge transfer in catalytic processes: new insights on the catalytic mechanism of CO oxidation on Au/TiO_2 from *ab initio* molecular dynamics. *J. Am. Chem. Soc.* 2013. Vol. 135, no. 29, p. 10673–10683.

[92] JIANG, Z, ZHANG, W, JIN, L, YANG, X, XU, F, ZHU, J and HUANG, W. Direct XPS Evidence for Charge Transfer from a Reduced Rutile TiO_2(110) Surface to Au Clusters. *J. Phys. Chem. C*. 2007. Vol. 111, no. 33, p. 12434–12439.

[93] DVOŘÁK, F, STETSOVYCH, O, STEGER, M, CHERRADI, E, MATOLÍNOVÁ, I, TSUD, N, ŠKODA, M, SKÁLA, T, MYSLIVEČEK, J and MATOLÍN, V. Adjusting morphology and surface reduction of CeO_2(111) thin films on Cu(111). *J. Phys. Chem. C*. 2011. Vol. 115, no. 15, p. 7496–7503.

[94] ŠEVČÍKOVÁ, K. *Study of catalytic properties of cerium oxide - metal system*. Charles University in Prague, 2010.

[95] ENGEL, T and ERTL, G. Elementary steps in the catalytic oxidation of carbon monoxide on platinum metals. *Adv. Catal.* 1979. Vol. 28, p. 1–78.

[96] ZAFIRIS, GS and GORTE, RJ. Evidence for a Second CO Oxidation Mechanism on Rh/Ceria. *J. Catal.* 1993. Vol. 143, no. 1, p. 86–91.

[97] FU, Q, SALTSBURG, H and FLYTZANI-STEPHANOPOULOS, M. Active nonmetallic Au and Pt species on ceria-based water-gas shift catalysts. *Science.* 2003. Vol. 301, no. 5635, p. 935–938.

[98] HEGDE, MS, MADRAS, G and PATIL, KC. Noble metal ionic catalysts. *Acc. Chem. Res.* 2009. Vol. 42, no. 6, p. 704–712.

[99] BERA, P, PRIOLKAR, KR, SARODE, PR, HEGDE, MS, EMURA, S, KUMASHIRO, R and LALLA, NP. Structural investigation of combustion synthesized Cu/CeO_2 catalysts by EXAFS and other physical techniques: Formation of a $Ce_{1-x}Cu_xO_{2-\delta}$ solid solution. *Chem. Mater*. 2002. Vol. 14, no. 8, p. 3591–3601.

[100] MATOLÍN, V, CABALA, M, MATOLÍNOVÁ, I, ŠKODA, M, LIBRA, J, VÁCLAVŮ, M, PRINCE, KC, SKÁLA, T, YOSHIKAWA, H, YAMASHITA, Y, UEDA, S and KOBAYASHI, K. Au^+ and Au^{3+} ions in CeO_2 rf-sputtered thin films. *J. Phys. D. Appl. Phys.* 2009. Vol. 42, no. 11, p. 115301 (7pp).

[101] FIALA, R, MATOLÍNOVÁ, I, MATOLÍN, V, ŠEVČÍKOVÁ, K, YOSHIKAWA, H and TAPAN, A. Electro-Oxidation Activity of Pt-CeO_x Carbon Supported Catalysts. *Int. J. Electrochem. Sci.* 2013. Vol. 8, no. 8, p. 10204–10218.

[102] MATOLÍNOVÁ, I, FIALA, R, KHALAKHAN, I, VOROKHTA, M, SOFER, Z, YOSHIKAWA, H, KOBAYASHI, K and MATOLÍN, V. Synchrotron radiation photoelectron spectroscopy study of metal-oxide thin film catalysts: Pt–CeO_2 coated CNTs. *Appl. Surf. Sci.* 2012. Vol. 258, no. 6, p. 2161–2164.

[103] YANG, Z, HE, B, LU, Z and HERMANSSON, K. Physisorbed, chemisorbed, and oxidized CO on highly active Cu-CeO_2(111). *J. Phys. Chem. C*. 2010. Vol. 114, no. 10, p. 4486–4494.

[104] SKÁLA, T and MATOLÍN, V. Photoemission study of cerium silicate model systems. *Appl. Surf. Sci.* 2013. Vol. 265, p. 817–822.

[105] NAGATA, H. A preliminary consideration of the growth behaviour of CeO_2, $SrTiO_3$ and $SrVO_3$ films on Si substrate. *Thin Solid Films*. 1993. Vol. 224, no. 1, p. 1–3.

[106] HILLEBRECHT, FU, RONAY, M, RIEGER, D and HIMPSEL, FJ. Enhancement of Si oxidation by cerium overlayers and formation of cerium silicate. *Phys. Rev. B.* 1986. Vol. 34, no. 8, p. 5377–5380.

[107] NEFEDOV, VI, FIRSOV, MN and SHAPLYGIN, IS Electronic structures of $MRhO_2$, MRh_2O_4, $RhMO_4$ and Rh_2MO_6 on the basis of X-ray spectroscopy and ESCA data. *J. Electron Spectros. Relat. Phenomena*. 1982. Vol. 26, no. 1, p. 65–78.

[108] CRUCQ, A and FRENNET, A (eds.). Catalysis and Automotive Pollution Control, vol. 30. *Stud. Surf. Sci. Catal.* Netherlands : Elsevier Science Publisher B.V., 1987. p. 1–495. ISBN 0444427783.

[109] PENNER, S, WANG, D, PODLOUCKY, R, SCHLÖGL, R and HAYEK, K. Rh and Pt nanoparticles supported by CeO_2: Metal-support interaction upon high-temperature reduction observed by electron microscopy. *Phys. Chem. Chem. Phys.* 2004. Vol. 6, no. 22, p. 5244–5249.

[110] BERG, C, RAAEN, S, BORG, A and VENVIK, HJ. Photoemission study of the Ce/Rh(100) overlayer system: Hybridization of *f* and *d* states. *Phys. Rev. B*. 1994. Vol. 50, no. 3, p. 1976–1979.

[111] VAVASSORI, P, DUÒ, L, CHIAIA, G, QVARFORD, M and LINDAU, I. Bulk electronic structure of Ce compounds studied by x-ray photoemission and x-ray absorption spectroscopies. *Phys. Rev. B*. 1995. Vol. 52, no. 23, p. 16503–16507.

[112] JUEL, M, MARTINSEN, S and RAAEN, S. Oxidation of thin Ce layers on Rh(110). *Thin Solid Films*. 2008. Vol. 517, no. 2, p. 805–810.

[113] ŠEVČÍKOVÁ, K, NEHASIL, V, ZAHORANOVÁ, T, VOROKHTA, M, TSUD, N, YOSHIKAWA, H, KOBATA, M, KOBAYASHI, K and MATOLÍN, V. The effect of the substrate on thermal stability of CeO_x and Rh-Ce-O thin films. *Surf. Interface Anal*. 2014. Vol. 46, no. 10-11, p. 980–983.

[114] MULLINS, DR, KUNDAKOVIC, LJ and OVERBURY, SH. The Interaction between NO and CO on Rh-Loaded CeO_x(111). *J. Catal.* 2000. Vol. 195, no. 1, p. 169–179.

[115] MAROT, L, MATHYS, D, DE TEMMERMAN, G and OELHAFEN, P. Characterization of sub-stoichiometric rhodium oxide deposited by magnetron sputtering. *Surf. Sci.* 2008. Vol. 602, no. 21, p. 3375–3380.

[116] GRASS, ME, ZHANG, Y, BUTCHER, DR, PARK, JY, LI, Y, BLUHM, H, BRATLIE, KM, ZHANG, T and SOMORJAI, GA. A reactive oxide overlayer on rhodium nanoparticles during CO oxidation and its size dependence studied by in situ ambient-pressure X-ray photoelectron spectroscopy. *Angew. Chem. Int. Ed. Engl.* 2008. Vol. 47, no. 46, p. 8893–8896.

[117] SAYLE, TXT., PARKER, SC and CATLOW, CRA. Surface Segregation of Metal Ions in Cerium Dioxide. *J. Phys. Chem.* 1994. Vol. 98, no. 51, p. 13625–13630.

[118] KILDEMO, M and RAAEN, S. Catalytic oxidation of 4H-SiC by a Ce overlayer. *Phys. Rev. B*. 2006. Vol. 73, no. 20, p. 205338 (9pp).

[119] ZEC, S and BOSKOVIC, S. Cerium silicates formation from mechanically activated oxide mixtures. *J. Mater. Sci*. 2004. Vol. 39, no. 16/17, p. 5283–5286.

[120] ESCH, F, FABRIS, S, ZHOU, L, MONTINI, T, AFRICH, C, FORNASIERO, P, COMELLI, G and ROSEI, R. Electron localization determines defect formation on ceria substrates. *Science*. 2005. Vol. 309, no. 5735, p. 752–755.

List of Tables

List of Abbreviations

BL15XU	BL15XU beamline at SPring-8 synchrotron, Japan
DFT	Density functional theory
Elettra	Elettra synchrotron, Italy
EMSI	Electron metal-support interaction
FWHM	Full width in half maximum
GGA	Generalized gradient approximation
HEAP Lab	HEAP Lab experimental station at National Institute for Materials Science, Japan
HREELS	High-resolution electron energy loss spectroscopy
HXPS	Hard X-ray photoelectron spectroscopy
IMFP	Inelastic mean free path
KFPP	Department of Surface and Plasma Science at Charles University in Prague, the Czech Republic
KolXPD	KolXPD software for processing the photoelectron spectroscopic data
LEED	Low-energy electron diffraction
ML	Monolayer
MSB	Materials Science beamline at Elettra synchrotron, Italy
NIMS	National Institute for Materials Science, Japan
NTIS	European centre of excellence in Pilsen, the Czech Republic
OSC	Oxygen storage capacity
PES	Photoelectron spectroscopy
PID (controller)	Proportional-integral-derivative (controller)
QMS	Quadrupole mass spectrometer
QUASES-IMFP-TPP2M	QUASES-IMFP-TPP2M software for estimating an inelastic mean free path of electrons in a solid
RER	Resonance enhancement ratio
RPES	Resonant photoelectron spectroscopy
SEM	Scanning electron microscopy
SPring-8	SPring-8 synchrotron, Japan
SuperESCA	SuperESCA beamline at Elettra synchrotron, Italy
SXPS	Soft X-ray photoelectron spectroscopy
TPR	Temperature programmed reaction
UHV	Ultra-high vacuum
UPS	Ultra-violet photoelectron spectroscopy
XPS	X-ray photoelectron spectroscopy
XPS-TPR	XPS-TPR experimental station at Department of Surface and Plasma Science, the Czech Republic
XRD	X-ray diffraction

Appendix A

Table A1: The list of the Rh/CeO_x samples (the Rh particles supported by the cerium oxide thin films).

Sample name	Substrate	Details of preparation
$Rh/CeO_x^{(Ox)}$	Si(100)	20 nm thick CeO_2 layer prepared *ex situ* by magnetron sputtering in $4 \cdot 10^{-3}$ mbar of Ar at 300 K, cleaned by heating in UHV (640 K, 10 min) and exposure in O_2 (300 K, $5 \cdot 10^{-8}$ mbar). Resulting stoichiometry $CeO_{1.94}$. 1 ML of rhodium evaporated in UHV at 300 K.
$Rh/CeO_x^{(Red)}$	Si(100)	20 nm thick CeO_2 layer prepared *ex situ* by magnetron sputtering in $4 \cdot 10^{-3}$ mbar of Ar at 300 K, reduced in UHV by a combination of heating (800 K) and ion sputtering (1 μA, 25 min). Resulting stoichiometry $CeO_{1.85}$. 1 ML of rhodium evaporated in UHV and 300 K.
$Rh/CeO_{1.98}$	Cu(111)	21 Å thick CeO_2 buffer layer (Ce evaporated *in situ* in $5 \cdot 10^{-7}$ mbar of O_2 at 520 K, 10 min post-annealing and cooling in O_2). Stoichiometry $CeO_{1.98}$. 0.97 ML of Rh deposited in UHV at 300 K in 6 steps.
$Rh/CeO_{1.97}$	Cu(111)	21 Å thick CeO_2 buffer layer (Ce evaporated *in situ* in $5 \cdot 10^{-7}$ mbar of O_2 at 520 K, 10 min post-annealing and cooling in O_2). Reduction by 3 min of Ce evaporation in UHV. Resulting stoichiometry $CeO_{1.97}$. 0.49 ML of Rh deposited in UHV at 300 K in 5 steps.
$Rh/CeO_{1.97}$	Cu(111)	23 Å thick CeO_2 buffer layer (Ce evaporated *in situ* in $5 \cdot 10^{-7}$ mbar of O_2 at 520 K, 10 min post-annealing and cooling in O_2). Reduction by 5 min of Ce evaporation in UHV. Resulting stoichiometry $CeO_{1.97}$. 0.62 ML of Rh deposited in UHV at 300 K in 5 steps.
$Rh/CeO_{1.93}$	Cu(111)	19 Å thick CeO_2 buffer layer (Ce evaporated *in situ* in $5 \cdot 10^{-7}$ mbar of O_2 at 520 K, 10 min post-annealing and cooling in O_2). Reduction by 7 min of Ce evaporation in UHV. Resulting stoichiometry $CeO_{1.93}$. 0.47 ML of Rh deposited in UHV at 300 K in 5 steps.

$Rh/CeO_{1.92}$	Cu(111)	19 Å thick CeO_2 buffer layer (Ce evaporated *in situ* in $5 \cdot 10^{-7}$ mbar of O_2 at 520 K, 10 min post-annealing and cooling in O_2). Reduction by 10 min of Ce evaporation in UHV. Resulting stoichiometry $CeO_{1.92}$. 0.74 ML of Rh deposited in UHV at 300 K in 5 steps.
$Rh/CeO_{1.90}$	Cu(111)	18 Å thick CeO_2 buffer layer (Ce evaporated *in situ* in $5 \cdot 10^{-7}$ mbar of O_2 at 520 K, 10 min post-annealing and cooling in O_2). Reduction by 12 min of Ce evaporation in UHV. Resulting stoichiometry $CeO_{1.90}$. 0.88 ML of Rh deposited in UHV at 300 K in 6 steps.
$Rh/CeO_{1.87}$	Cu(111)	19 Å thick CeO_2 buffer layer (Ce evaporated *in situ* in $5 \cdot 10^{-7}$ mbar of O_2 at 520 K, 10 min post-annealing and cooling in O_2). Reduction by 13 min of Ce evaporation in UHV. Resulting stoichiometry $CeO_{1.87}$. 0.53 ML of Rh deposited in UHV at 300 K in 5 steps.
$Rh/CeO_{1.82}$	Cu(111)	19 Å thick CeO_2 buffer layer (Ce evaporated *in situ* in $5 \cdot 10^{-7}$ mbar of O_2 at 520 K, 10 min post-annealing and cooling in O_2). Reduction by 13 min of Ce evaporation in UHV. Resulting stoichiometry $CeO_{1.82}$. 0.65 ML of Rh deposited in UHV at 300 K in 5 steps.
$Rh/CeO_{1.81}$	Cu(111)	20 Å thick CeO_2 buffer layer (Ce evaporated *in situ* in $5 \cdot 10^{-7}$ mbar of O_2 at 520 K, 10 min post-annealing and cooling in O_2). Reduction by 15 min of Ce evaporation in UHV. Resulting stoichiometry $CeO_{1.81}$. 0.40 ML of Rh deposited in UHV at 300 K in 4 steps.
$Rh/CeO_{1.67}$	Cu(111)	19 Å thick CeO_2 buffer layer (Ce evaporated *in situ* in $5 \cdot 10^{-7}$ mbar of O_2 at 520 K, 10 min post-annealing and cooling in O_2). Reduction by 30 min of Ce evaporation in UHV. Resulting stoichiometry $CeO_{1.67}$. 0.70 ML of Rh deposited in UHV at 300 K in 6 steps.

Table A2: The list of the Rh-CeO_x samples (the cerium oxide thin films doped by rhodium).

Sample name	Substrate	Details
Rh-CeO_x	SiO_2/Si(100)	20 nm thick Rh-CeO_2 layer prepared *ex situ* by magnetron sputtering from the composite target in $4 \cdot 10^{-3}$ mbar of Ar at 300 K. Concentration of rhodium varied from 1 to 9%. 60 nm thick SiO_2 layer achieved by annealing the Si crystal in air at 1430 K for 5 min (annealing rate 60 $K \cdot min^{-1}$).
Rh-CeO_x	SiO_2/Si(100)	6 nm thick Rh-CeO_2 layer prepared *in situ* by magnetron sputtering from the composite target in $6 \cdot 10^{-3}$ mbar of Ar at 300 K. Layer contained 1 and 5% of rhodium. 60 nm thick SiO_2 layer achieved by annealing the Si crystal in air at 1430 K for 5 min (annealing rate 60 $K \cdot min^{-1}$).
Rh-CeO_x	Cu	6 nm thick Rh-CeO_2 layer prepared *in situ* by magnetron sputtering from the composite target in $6 \cdot 10^{-3}$ mbar of Ar at 300 K. Layer contained 1 and 5% of rhodium. 60 nm thick SiO_2 layer achieved by annealing the Si crystal in air at 1430 K for 5 min (annealing rate 60 $K \cdot min^{-1}$).

Table A3: The list of the cerium oxide thin films doped by F, Si, Au, and Cu.

Sample name	Substrate	Details
F-CeO_x	Cu(111)	22 Å thick CeO_2 layer (Ce contaminated by fluorine evaporated *in situ* in $5 \cdot 10^{-7}$ mbar of O_2 at 520 K, 10 min post-annealing and cooling in O_2). 11% of fluorine.
Si-CeO_x	Si(100)	3 nm thick CeO_2 layer prepared *ex situ* by magnetron sputtering in $4 \cdot 10^{-3}$ mbar of Ar at 300 K. Si-doping resulted from migration of Si atoms from substrate to CeO_2 layer.
Au-CeO_x	C/SiO_2/Si(111)	4 nm thick Au-CeO_2 layer prepared *ex situ* by a combination of magnetron sputtering from the CeO_2 target in $5 \cdot 10^{-3}$ mbar of Ar and simultaneous evaporation of Au at 300 K. Layer contained 5% of gold. 30 nm thick carbon film prepared by magnetron sputtering from graphite target in $6 \cdot 10^{-3}$ mbar of Ar at 300 K. 60 nm thick SiO_2 layer achieved by annealing the Si crystal in air at 1430 K for 5 min (annealing rate 60 $K \cdot min^{-1}$).
Cu-CeO_x	SiO_2/Si(100)	25 nm thick Cu-CeO_2 layer prepared *ex situ* by magnetron sputtering from the composite target in $4 \cdot 10^{-3}$ mbar of Ar at 300 K. Layer contained 8% of copper. 60 nm thick SiO_2 layer achieved by annealing the Si crystal in air at 1430 K for 5 min (annealing rate 60 $K \cdot min^{-1}$).

Applied Surface Science 332 (2015) 747–755

Appendix B

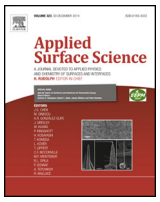

Impact of Rh–CeO_x interaction on CO oxidation mechanisms

Klára Ševčíková [a,*], Tatiana Kolářová [a], Tomáš Skála [a], Nataliya Tsud [a], Michal Václavů [a], Yaroslava Lykhach [b], Vladimír Matolín [a], Václav Nehasil [a]

[a] Charles University in Prague, Faculty of Mathematics and Physics, Department of Surface and Plasma Science, V Holešovičkách 2, 18000 Prague 8, Czech Republic
[b] Lehrstuhl für Physikalische Chemie II, Friedrich-Alexander-Universität Erlangen-Nürnberg, Egerlandstrasse 3, 91058 Erlangen, Germany

ARTICLE INFO

Article history:
Received 13 November 2014
Received in revised form 22 January 2015
Accepted 25 January 2015
Available online 3 February 2015

Keywords:
Rhodium
Ceria
CO oxidation
Spillover
Metal–oxide interaction
Photoelectron spectroscopy

ABSTRACT

We have investigated the impact of electronic metal–support interaction on catalytic properties of Rh/CeO_x system, i.e. its capacity for the *reverse* and *direct* oxygen spillover, in the context of CO oxidation. The studies were carried out on two types of samples consisting of Rh particles supported on polycrystalline nearly stoichiometric and partially reduced cerium oxide films using temperature programmed reaction, temperature programmed desorption, and conventional X-ray and resonant photoelectron spectroscopies. We have found that the electronic Rh–CeO_x interaction leads to a buildup of a net positive charge on Rh particles supported on stoichiometric cerium oxide, and a net negative charge on Rh particles on reduced cerium oxide. The effect of the Rh–CeO_x interaction is manifested in suppression of the *reverse* and *direct* oxygen spillover on Rh particles supported on partially reduced ceria.

1. Introduction

Ceria based catalysts possess unique catalytic properties that arise from the oxygen storage capacity of cerium oxide [1–3]. In the systems containing small noble metal particles dispersed on the reducible cerium oxide, the release of lattice oxygen proceeds via the *reverse* spillover of activated oxygen species onto the surfaces of supported metal particles [4–6]. Spillover of active species between the metal and the support is considered to be of a paramount importance in heterogeneous catalysis [7]. The *reverse* oxygen spillover, in particular, plays an important role in preventing carbon poisoning of the noble metal particles and controlling oxidation reactions [4,6]. The evidence for the *reverse* oxygen spillover has been obtained on Rh, Pd, and Pt particles supported on cerium oxide [6,8–13]. For example, the *reverse* oxygen spillover is responsible for depletion of oxygen in the ceria near-surface region [5,6,12–14], oxidation of adsorbed CO without carbon formation on Rh/CeO_2 [4], oxidation of Pd particles upon annealing of Pd/ceria–zirconia layer above 500 K [9], CO formation during C_2H_4 decomposition on Rh/CeO_2 [10], and removal of carbon on Pd/CeO_2 [11], Rh/CeO_2 [12], and Pt/CeO_2 [13].

Furthermore, Bunluesin et al. [8] showed that the controlling factor of the oxygen reverse spillover in ceria based systems is the structure of the cerium oxide rather than the choice of a catalytically active metal. This is consistent with lowering the energy of oxygen vacancy formation for systems containing CeO_x nanostructures and rough surfaces compared to the highly ordered CeO_2 systems [6,14,15]. Polycrystalline cerium oxide shows high oxygen mobility through the material and therefore, provides a suitable substrate for studying the effects of the oxygen reverse spillover [14].

The stoichiometry of cerium oxide, specifically the degree of its reduction, is yet another factor that may influence catalytic properties of supported catalysts. The electronic metal–support interaction (EMSI) and associated charge transfer between the oxide and the supported metal particle can be employed to tune the electronic and catalytic reactivity of the metal/oxide catalyst [16,17]. Amazingly, the direction of charge transfer can be altered by simply changing the stoichiometry of the oxide before depositing of metal particles. The most relevant and widely studied example in the literature is Au particles supported on reducible TiO_2(1 1 0) substrate [17–19]. In this system, the charge transfer from Au particles into the support causes the reduction of titanium oxide and positive net charge on Au particles supported on stoichiometric TiO_2(1 1 0). In contrast, charge transfer from the support to the metal particles leads to re-oxidation of titanium oxide and negative net charge on Au particles supported on reduced TiO_{2-x}(1 1 0).

* Corresponding author. Tel.: +420 733 514 434; fax: +420 284685095.
E-mail address: klarak.sevcikova@seznam.cz (K. Ševčíková).

http://dx.doi.org/10.1016/j.apsusc.2015.01.197
0169-4332/

The charge transfer from the metal particles to the support has been also identified in several systems containing metal particles supported on well-ordered stoichiometric CeO_2(1 1 1) films: Pt/CeO_2 [6,16], Pd/CeO_2 [20,21], Au/CeO_2 [22], Ag/CeO_2 [23], and Cu/CeO_2 [24]. However, fewer studies exist on the effects of metal deposition on reduced CeO_{2-x} surfaces [24]. Apart from the systems listed above, Rh/CeO_2 has not been yet investigated with respect to the EMSI between Rh particles and cerium oxide substrate.

Rh/CeO_2 is well studied system in the variety of chemical reactions, however, a clear relation between its catalytic properties and the charge transfer phenomena arising from the EMSI has never been established for this system.

In the current paper we study the impact of the EMSI on catalytic properties of Rh/CeO_2 system, in particular, on the *reverse* and *direct* oxygen spillover between Rh particles and the ceria support during CO oxidation.

Catalytic oxidation of carbon monoxide is often used to characterize the properties of catalytic systems [25–27], especially those related to the metal particle size [27–32] and the electronic metal–support interaction [18,32]. The influence of the degree of ceria reduction on the reactivity of the noble metal particles toward CO is the most prominent for Rh. It was reported that the amount of dissociated CO increases considerably on Rh particles deposited on reduced ceria [2,12]. Stubenrauch and Vohs [12] estimated that as much as 62% of the adsorbed CO underwent dissociation on Rh particles supported on partially reduced CeO_x in contrast to only 14% on Rh particles on nearly stoichiometric CeO_2. Unlike on Rh/CeO_2, the degree of ceria reduction has no effect on the extent of CO dissociation on Pd or Pt particles supported on cerium oxide [11,33]. Clearly, the interaction of ceria with Rh is different from that with Pd or Pt. Mullins and Overbury [2] hypothesized that Rh particles could withdraw charge from Ce^{3+} sites. The authors suggested that Rh could be slightly anionic, thus promoting dissociation of the C—O bond.

In the current paper, we will first demonstrate that EMSI results in the charge transfer between Rh and ceria support and that the direction of this charge transfer depends on the degree of ceria reduction. Next we will show that both *reverse* and *direct* oxygen spillover are facile on Rh supported on nearly stoichiometric ceria but substantially suppressed when Rh is supported on reduced ceria. For this purpose, we have combined the temperature programmed reaction (TPR) study with the X-ray and resonant photoelectron spectroscopy measurements (XPS, RPES).

2. Materials and methods

Two types of samples comprising Rh particles supported on nearly stoichiometric (A) and partially reduced polycrystalline (B) cerium oxide films have been used to study the Rh–CeO_x interaction and its influence on CO oxidation under steady-state and CO reaction with oxygen pre-exposed surfaces. Thin films of polycrystalline cerium oxide have been deposited by magnetron sputtering of CeO_2 target (99.99%, Lesker) ex situ either onto a clean polycrystalline oxygen-free copper foil (99.9%, Goodfellow) or a single crystalline Si(1 0 0) wafer covered by a natural oxide. During one sputtering (Ar plasma, 6×10^{-3} mbar, 50 W, deposition rate ~ 1 nm min^{-1}), several samples with same specifications were prepared, which were subsequently used for various types of experiments. The atomic force microscope (AFM) measurements showed that the thickness of the cerium oxide films was approximately 30 nm. The grain size in the ceria films supported on Si(1 0 0) was between 5 and 20 nm. The surface roughness in the direction of the surface normal was about 3 nm. Thus, the morphology of as prepared films resembled the structure of cerium oxide substrates on which the reverse oxygen spillover was found facile [14].

Cerium oxide substrates labeled (A) were used as prepared, i.e. without any further cleaning. Substrates for the samples (B) were cleaned by a combination of soft Ar^+ ion sputtering at 300 K (500 eV, 1 μA cm^{-2}, 25 min) and annealing to 800 K. This procedure caused considerable reduction of the oxide [34].

The Ce 3*d* spectra were fitted with five doublets using the Voigt profile after a subtraction of Shirley background [35]. The detailed description of the fitting procedure along with the list of fitting parameters is available in Supplementary material. The stoichiometry of CeO_x films was determined from the contribution of Ce^{3+} states to the total signal (Ce^{3+} + Ce^{4+}) from Ce 3*d* spectra. The stoichiometries of the cerium oxide substrates (A) and (B) prior to Rh deposition were $CeO_{1.95}$ and $CeO_{1.70}$, respectively, if not stated otherwise.

Subsequently, similar amounts of Rh were deposited onto all (A) and (B) substrates by means of physical vapor deposition from an Rh wire (99.9%, Goodfellow) at 300 K in situ. Because of the very low deposition rate ($\sim$1 nm h^{-1}), rhodium was evaporated in 1 min-cycles with 1 min-breaks to prevent heating the substrate. The amount of deposited Rh was calibrated by means of an oscillating quartz microbalance and by XPS. The samples used in temperature programmed desorption (TPD) and reactions (TPR) experiments contained Rh amount equivalent to approximately 1 monolayer (ML) of Rh. The samples for the study of Rh–CeO_x interaction were prepared in five consecutive steps and the total Rh thickness was equivalent to 0.6 ML. Total pressure during Rh deposition was always lower than 3×10^{-9} mbar.

The samples used for the studies of Rh–CeO_x interaction, TPD, and TPR during the reaction of CO with oxygen pre-exposed samples have been prepared on copper foil. The samples used for the TPR under steady-state conditions were prepared on silicon wafers.

The Rh interaction with both CeO_x substrates (A) and (B) was studied at the Materials Science Beamline at the Elettra synchrotron radiation source in Trieste, Italy. The experimental ultra-high vacuum (UHV) chamber with a base pressure $\sim 10^{-10}$ mbar was equipped with a Specs Phoibos 150 hemispherical electron analyzer, a dual-anode Mg/Al Kα X-ray source, an Ar^+ sputter gun, an Rh evaporator, a gas inlet, and a sample heating and cooling system. The Ce 3*d* core levels discussed below were acquired with Al Kα radiation (1486.6 eV). Valence band spectra were acquired at three different photon energies, 121.4, 124.8, and 115.0 eV. These energies correspond to the resonant enhancements in Ce^{3+}, Ce^{4+} ions, and to the off-resonance conditions, respectively. Analysis of the spectra obtained with these photon energies is the basis of RPES [36]. The Ce^{3+} resonance at photon energy 121.4 eV is caused by a super Coster–Kronig decay involving electron emission from Ce 4*f* states located about 1.4 eV below the Fermi level. The Ce^{4+} resonance at photon energy 124.8 eV involves emission of the O 2*p* electrons (hybridized with Ce states) from the valence band around 4.0 eV. The valence band spectrum measured at photon energy 115 eV is used as a background for calculating the intensity difference between the corresponding features on- and off-resonance, denoted as the resonant enhancements for Ce^{3+} (DCe^{3+}) and Ce^{4+} (DCe^{4+}). The resonant enhancement ratio DCe^{3+}/DCe^{4+}, is a direct measure of the degree of ceria reduction.

The valence band spectra were acquired at the emission angles of 0° and Ce 3*d* spectra at 20° with respect to the surface normal. The valence band spectra were normalized to the incident photon flux. The total spectral resolutions achieved were 1 eV (Al Kα) and 150 meV ($h\nu$ = 115–125 eV).

Series of TPD and CO oxidation TPR experiments were performed in an UHV chamber at the Department of Surface and Plasma Science in Prague. The chamber was equipped with a dual-anode Mg/Al Kα X-ray source, an Omicron EA 125 hemispherical electron analyzer, an Ar^+ sputter gun, an Rh evaporator, a molecular beams system, a quadrupole mass spectrometer (QMS) Leybold

Inficon 2000, and a system for a temperature regulation. The QMS was mounted in a differentially pumped chamber connected to the experimental chamber by a 3 mm orifice. Samples were positioned opposite to the orifice within a defined distance. The base pressure was in 10^{-10} mbar range.

Prior to each TPD cycle, samples were exposed to a saturation dose of CO (10 L) at 300 K. The following TPD spectra were recorded between 300 and 800 K. The temperature was ramped at 1 K s^{-1}.

The CO reaction with oxygen pre-exposed samples involved pre-exposure of the sample to 30 L of O_2 at 440 K, setting up the reaction temperature and exposing the sample to the molecular beams of CO. XPS measurements were performed to characterize changes in the chemical state of the sample induced by the TPR experiments. The Ce 3*d* core level spectra were acquired at an emission angle of 0° using Al Kα X-ray source (total resolution 1 eV). The ratio of Ce^{3+}/Ce^{4+} spectral contributions to Ce 3*d* spectra was used to quantify the degree of ceria reduction.

The steady-state reaction experiments were executed as follows. Molecular beams of CO and O_2 at the intensity of 5×10^{12} molecules cm^{-2} s^{-1} were directed onto the sample kept at 300 K. Next, the sample temperature was increased linearly to 800 K, and heating was switched off at that temperature. Immediately after this, the sample was cooled down to 300 K under continuous exposure to molecular beams. This procedure is regarded as a single reaction cycle.

The partial pressures of the reflected molecular beams (CO, O_2) or reaction products (CO_2) were monitored by the QMS during both steady-state experiment and CO reaction with pre-exposed samples. The temperature was measured by a K-type thermocouple and registered by the analog port of the QMS.

3. Results and discussion

3.1. Electronic metal–support interaction

Interaction of Rh particles with CeO_x substrates was studied as a function of the degree of ceria reduction. Rhodium was deposited in five consecutive steps onto nearly stoichiometric ($CeO_{1.95}$, A) and partially reduced ($CeO_{1.70}$, B) substrates at 300 K. Developments of the degree of ceria reduction determined by means of RPES (DCe^{3+}/DCe^{4+}) and XPS (Ce^{3+}/Ce^{4+}) during Rh deposition are plotted in Fig. 1. Both parameters, DCe^{3+}/DCe^{4+} and Ce^{3+}/Ce^{4+}, show similar trends and can be used independently to estimate the reduction degree of the ceria surface.

Evolution of both DCe^{3+}/DCe^{4+} and Ce^{3+}/Ce^{4+} parameters during Rh deposition reveals striking difference between two samples (A) and (B). Both parameters increase in parallel during Rh deposition on sample (A) but decrease on sample (B). This behavior suggests that Rh deposition induces reduction of cerium oxide on sample (A) and re-oxidation of cerium oxide on sample (B).

Reduction of ceria by deposited metal has been reported earlier for Pt/CeO_2 [6], Pd/CeO_2 [20,21], Au/CeO_2 [22], and Cu/CeO_2 [24] systems. The extent of ceria reduction induced by these metals is comparable to that observed on Rh/CeO_x (A) sample. Therefore, we assign reduction of cerium oxide upon Rh deposition on sample (A) to the electronic metal–support interaction and associated charge transfer from Rh particles to ceria. According to Vayssilov et al. [6] the electron transfer from metal cluster and formation of Ce^{3+} is facilitated by a small energy difference between the highest occupied levels in metal and empty Ce 4*f* states. This view is corroborated by Pfau et al. [37], who derived a nonzero overlap between Rh 4*d* and Ce 4*f* orbitals on Rh/CeO_2(1 1 1) system. The charge transfer from Rh to CeO_2 has been also predicted by Lu and Yang [38] based on density functional (DF) calculations.

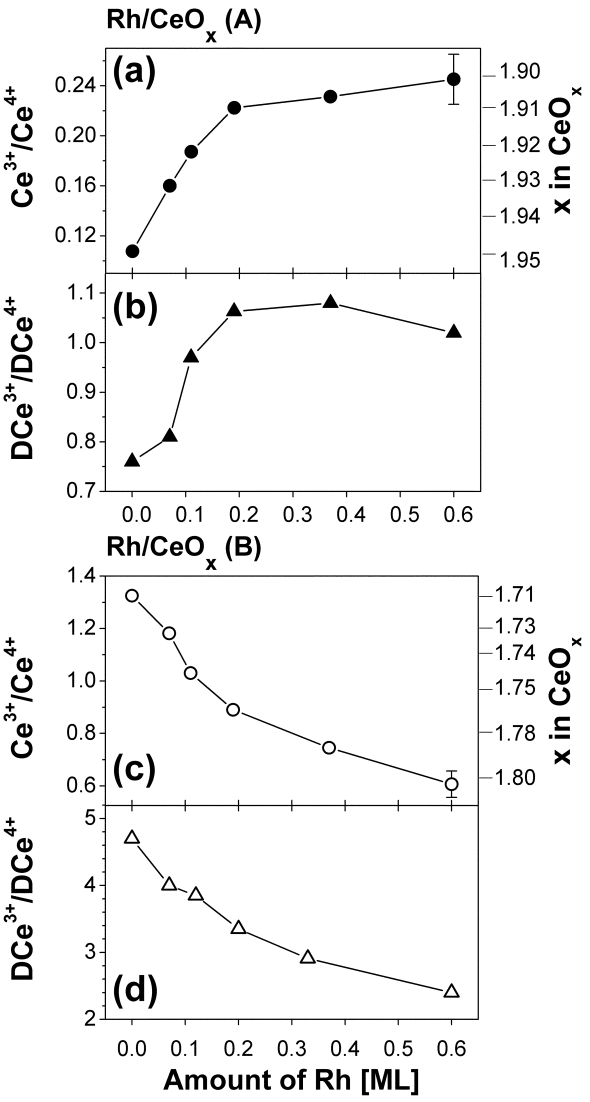

Fig. 1. Evolution of the degree of ceria reduction during Rh deposition onto CeO_x films (A) (a and b) and (B) (c and d) as determined from XPS, Ce^{3+}/Ce^{4+}, (a and c) and SRPES, DCe^{3+}/DCe^{4+}, (b and d).

Re-oxidation of cerium oxide upon Rh deposition on sample (B) is rather unusual. Since Rh deposition has been performed in situ and under UHV, presence of molecular oxygen in the chamber can be ruled out. Small amount of water is usually present in the chamber but it would not cause any detectable re-oxidation of reduced cerium oxide at 300 K [39,40]. The re-oxidation of reduced cerium oxide due to transport of oxygen from deeper and more oxidized layers toward more reduced surface is well known effect [4] but it does not play an important role during Rh deposition at room temperature. The extent of oxygen migration at 300 K is very low and it would not explain the differences between the samples (A) and (B) discussed in further chapters. Moreover, we did not observe any significant changes in O 1*s* regions (data not shown). Therefore, re-oxidation of reduced cerium oxide (B) has to be induced by the interaction with rhodium which is different from that discussed for the sample (A). The nearly stoichiometric cerium oxide (A) is terminated with O^{2-} layer while the partially reduced cerium oxide (B) surface contains exposed Ce^{3+} ions. Rhodium can thus interact directly with cerium ions (Rh–Ce), unlike on stoichiometric cerium oxide (A) where Rh and Ce is separated by an oxygen layer (Rh—O—Ce).

The Rh–Ce interaction on the Rh/CeO_x (B) samples is evident from our measurement of the valence band region (see Fig. S3 in Supplementary Information). The interaction between Ce and Rh atoms induces partial transfer of the electron density from Ce 4*f* to Rh 4*d* state. The decreasing occupancy of Ce 4*f* state can be clearly seen from both, RPES measurements of valence band (Fig. 1(c)), and from Ce 3*d* core level measured by XPS (Fig. 1(d)). The partial charge transfer from Ce^{3+} to Rh results in a buildup of a negative charge on rhodium. Mullins and Overbury [2] hypothesized that Rh particles could withdraw charge from relatively electron rich Ce^{3+} sites making Rh slightly anionic on reduced substrate. This assumption complies with the DFT calculations of Yang et al. [41], who predicted formation of the gap states (mixed Rh 4*d* with O 2*p*) capable of accommodation of the electrons left upon removal of oxygen from cerium oxide. Therefore, the observed re-oxidation of reduced cerium oxide might be caused by a charge transfer from the support to the Rh particles similar to Au/TiO_2(1 1 0) [18,19] and Cu/CeO_2 [24] systems.

The difference between two samples (A) and (B) is also apparent from the development of Rh $3d_{5/2}$ core levels (Fig. S1). The corresponding Rh $3d_{5/2}$ peaks emerge at 308.1 eV (sample (A)) and 307.7 eV (sample (B)) after first deposition step and gradually shift to 307.5 eV and 307.1 eV, respectively, with increasing Rh coverage. The downward shift of binding energy on both samples is consistent with formation of small Rh particles and their growth during Rh deposition [28]. Despite the same amounts of rhodium were deposited at each step on both samples, Rh $3d_{5/2}$ binding energy is systematically lower on the sample (B) and it is also slightly lower than the value reported in the literature for bulk Rh (307.2 eV) [42]. The offset of the Rh $3d_{5/2}$ binding energy between samples (A) and (B) after the last Rh deposition was 0.4 eV. Although the metal particle morphology can influence binding energy of core level peaks, as in the case of Au nanoparticles [43], this should not apply for Rh/CeO_x. Zhou et al. [44] reported that the morphology of Rh particles was nearly independent of the degree of ceria reduction. Therefore, the reason for the binding energy offset between the two samples should not be related to the particle size but rather to a difference in effective charges on rhodium. Higher binding energy of Rh 3*d* peaks can be explained by the charge transfer from rhodium to cerium oxide on the sample (A). On the contrary, lower binding energy of Rh 3*d* is in agreement with a buildup of net negative charge on rhodium in the case of the sample (B).

The alternative explanation of the observed development on the sample (B) upon Rh deposition could be formation of Ce–Rh alloy. For instance, re-oxidation of reduced cerium oxide upon deposition of palladium at 300 K on mixed Ga—Ce—O and Sn—Ce—O oxides has been reported by Skála et al. [20]. The authors explained the observed effect by formation of Pd–Ga and Pd–Sn alloys. Formation of various alloy phases has been also reported for Rh/CeO_2 system during reductive treatments above 723 K [45]. The low binding energy of Rh 3*d* has been observed by Berg and Raaen [46] upon formation of a Rh–Ce mixed phase. The shift of Rh 3*d* core level by 0.4 eV to lower binding energy has been also explained by the formation of Rh–Ce alloy upon deposition of metallic Ce on Rh(1 1 0) at 300 K [47]. However, based on the thermodynamic considerations and Gibbs energies for CeO_2, Ce_2O_3, and Rh–Ce alloys (Ce_5Rh_4, $CeRh_2$, $CeRh_3$), the reactions between rhodium and reduced ceria resulting in re-oxidation of ceria and formation of any Rh–Ce alloy are not favorable under the current experimental conditions.

Therefore we assume that the charge transfer from the partially reduced cerium oxide to supported Rh particles yields partial re-oxidation of reduced cerium oxide and net negative charge on Rh particles.

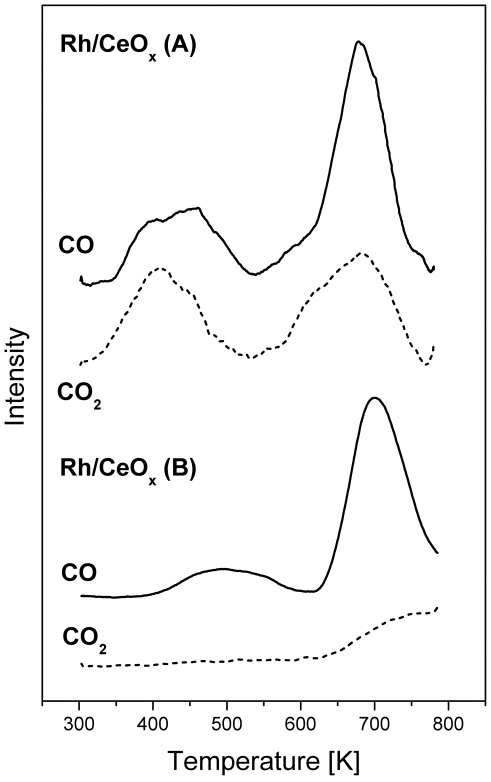

Fig. 2. CO (solid line) and CO_2 (dotted line) TPD spectra following adsorption of 10 L of CO on Rh/CeO_x (A) and Rh/CeO_x (B) at 300 K. The linear background was subtracted from all spectra. Spectra were offset for clarity.

3.2. Influence of electronic metal–support interaction on CO adsorption

We have performed TPD study of CO adsorption and desorption on both samples Rh/CeO_x (A) and (B). Development of CO and CO_2 on both samples was compared to the results obtained on Rh/CeO_x systems prepared on single crystalline [12,14] and well-ordered thin cerium oxide substrates [2,33].

CO desorption spectra along with the yield of CO_2 are plotted in Fig. 2. CO desorbs in two peaks: the broad double peak structure with distinct maxima at about 400 and 470 K and a sharp peak at 680 K (sample A). The double peak is associated with molecular CO adsorption. The positions of low temperature maxima, 400 and 470 K, are similar to these reported for Rh particles supported on single crystalline (about 410, 480 K) [12], amorphous (410, 480 K) [4], and polycrystalline CeO_2 (400, 500 K) [14], as well as on Rh(1 1 0) (about 420, 480 K) [48], and Rh(1 1 1) single crystals (410, 500 K) [49]. It is noteworthy that the double peak maxima appears at higher temperatures, at about 475 and 540 K, respectively, on Rh/CeO_x (B) (see Fig. 2).

The shift of the double peak to higher temperatures cannot be explained by the presence of any co-adsorbates such as oxygen or carbon. On the contrary, both co-adsorbed oxygen [50] and carbon [51] on Rh single crystal surfaces shift CO desorption peak to lower temperature.

The origin of the peak at 680 K is associated with the recombinative CO desorption [12]. Dissociation of CO on Rh/CeO_x is well documented in the literature [2,12,14]. It is noteworthy that the high temperature CO desorption peak was absent on the Rh supported on well-ordered CeO_2(1 1 1) films [33]. The fraction of the dissociated CO molecules strongly depends on the degree of ceria reduction [14]. The intensity of this high temperature peak relative to the low temperature peak is markedly higher on sample

(B) as compared to sample (A). It is also shifted to 700 K. However, the difference between desorption temperatures of the recombined CO on samples (A) and (B) is not as substantial as that between molecularly adsorbed CO.

Higher desorption temperature of molecular CO from the sample (B) corroborates the hypothesis of the charge transfer from Ce^{3+} to Rh discussed in Section 3.1. According to Blyholder [52], the negative charge on Rh particle increases the CO—metal bond strength. The additional effect of the negative charge on the rhodium is weakening of the C—O bond [52]. This explanation has been earlier invoked by Mullins and Overbury [2] to explain enhanced CO dissociation on Rh/CeO_x. Most likely, the hybridization and the charge transfer between Ce 4*f* and Rh 4*d* states leads to alteration of the electronic structure of Rh 4*d* band that in turn affects catalytic properties of Rh particles.

Considerable amounts of CO_2 were formed in parallel to the CO desorption on sample (A) (see Fig. 2). Two CO_2 desorption peaks are well resolved at 410 and 680 K on sample (A). It is important to note that the desorption of CO_2 has been observed on Rh supported on thin cerium oxide films [3,4,33] but *not* on the Rh supported on bulk ceria single crystals [12]. The CO_2 peak at 410 K was interpreted as the reaction product of molecular CO with the lattice oxygen provided by cerium oxide [33]. Because CO can adsorb in the used partial pressures only on rhodium, not on cerium oxide, the onset of CO_2 formation would indicate the beginning of the oxygen reverse spillover on Rh/CeO_x. Since CO_2 formation starts slightly above 300 K on sample (A), the polycrystalline cerium oxide substrate appears more reactive than, for example, amorphous cerium oxide films prepared by spray pyrolysis [4]. The second CO_2 desorption peak at 680 K coincides with the recombinative CO desorption peak from sample (A). It is likely that a fraction of dissociated CO recombines with spilled over oxygen on Rh. Note that CO_2 desorption is much lower on sample (B) and is observable only above 650 K (see Fig. 2) which indicates a strong suppression of oxygen reverse spillover.

3.3. Suppression of reverse oxygen spillover

The CO oxidation under steady-state reaction conditions has been studied on both Rh/CeO_x (A) and Rh/CeO_x (B) samples as well as on the reference Rh foil and on nearly stoichiometric Rh-free CeO_x (A). The corresponding CO_2 production curves obtained under the simultaneous exposure of the samples to molecular beams of CO and O_2 (1:1) are shown in Fig. 3.

CO_2 production has been monitored between 300 and 800 K during linear increase of the temperature (Fig. 3, left) and cooling of the sample (Fig. 3, right). These two parts in Fig. 3 are separated by a dotted line. Two distinct maxima of the CO_2 production, (i) and (ii), were observed on both Rh/CeO_x (A) and Rh/CeO_x (B). The peak (i) emerges during heating at 475 K on sample (A) and at 640 K on sample (B). The peak (ii) emerges during cooling at 480 K on sample (A) and at 485 K on sample (B). It is noteworthy that the peak (ii) occurs at similar temperature as the peak (i) on sample (A) but not on the sample (B). The difference between the maxima (i) and (ii) on sample (B) is as much as 150 K. Another difference between two samples is the emergence of the peak (iii), formed at the break heating/cooling point at 800 K on sample (A). It is apparent that the preparation procedure of Rh/CeO_x samples has a tremendous influence on the reactivity of this system.

First we discuss asymmetric positioning of the CO_2 production maxima (i) and (ii) on Rh/CeO_x (B) (Fig. 3(b)). We presume that in the initial stage of the reaction cycle, Rh particles are saturated by strongly bound CO. That would inhibit adsorption of oxygen [4,53], resulting in very small CO_2 production below 400 K. It was reported that CO does not inhibit reverse oxygen spillover [5]. However, reverse oxygen spillover is not as facile on sample

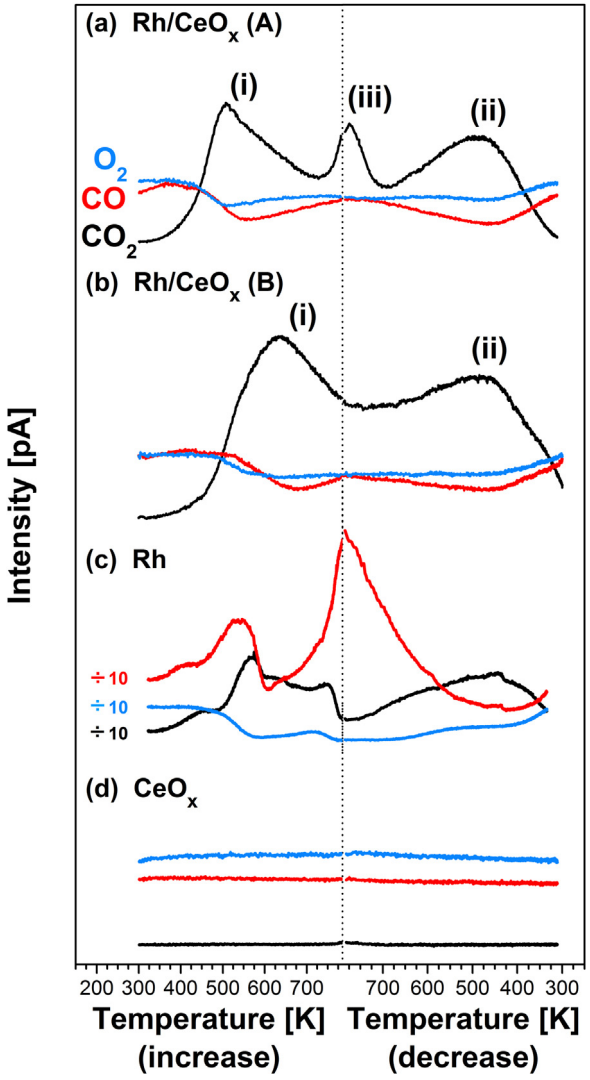

Fig. 3. CO_2 production curve (black), and molecular beam intensities of O_2 (blue) and CO (red) under steady-state conditions on Rh/CeO_x (A) (a), Rh/CeO_x (B) (b), Rh foil (c), and nearly stoichiometric Rh-free CeO_x (A) (d) during linear heating (left) and cooling (right). The intensities on Rh foil (c) were divided by 10 to fit the scale of the figure. Constant background was subtracted and spectra were offset for the sake of clarity. The ratio of molecular beams of CO:O_2 was 1:1. (For interpretation of the references to color in this figure legend, the reader is referred to the web version of this article.)

(B) as it is on sample (A), which is shown in Section 3.2. Most likely, CO_2 production begins as soon as CO desorption starts liberating adsorption sites for O_2. Fig. 2 clearly shows that CO desorbs at higher temperature from Rh/CeO_x (B) compared to (A) what explains the temperature difference between the reaction maxima (i) on the samples (A) and (B). At the temperatures above the peaks (i) and (ii), we assume that the CO residence time on Rh becomes shorter than the time needed for O_2 dissociation and CO_2 formation, and CO oxidation ceases. Because adsorbed oxygen on Rh does not inhibit CO adsorption under present experimental conditions [53], CO_2 production during cooling begins as soon as CO starts to adsorb on Rh. That is why the peaks (ii) occur at approximately same temperature on both samples. On the other hand, the position of the peak (i) is determined by the strength of the CO–Rh/CeO_x bond which is different for the samples (A) and (B).

Next, we discuss peak (iii) formed at the break heating/cooling point at 800 K observed on Rh/CeO_x (A). Since the rapid increase of CO_2 production is above 750 K, CO oxidation can no longer be

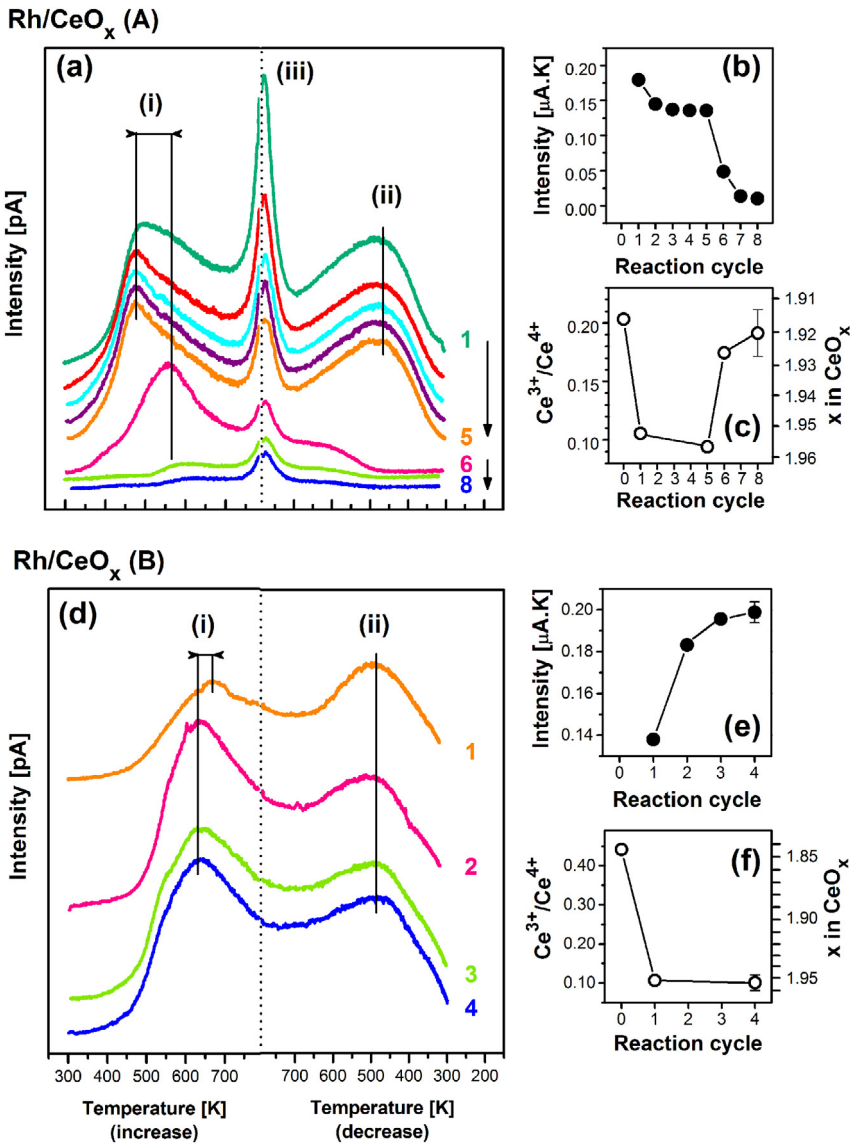

Fig. 4. CO_2 production curves obtained from Rh/CeO_x (A) (a) and Rh/CeO_x (B) (d) during subsequent TPR cycles under steady-state conditions during linear heating (a and d, left) and cooling (a and d, right). Constant background was subtracted and spectra were offset for clarity. The ratio between molecular beams CO:O_2 was 1:1 during TPR cycles 1–5 on both samples (A) and (B) and 1:0 during TPR cycles 6–8 on sample (A). Total amount of CO_2 produced in successive reaction cycles on sample (A) (b) and sample (B) (e). The evolution of the degree of ceria reduction, Ce^{3+}/Ce^{4+}, on sample (A) (c) and sample (B) (f) during the subsequent TPR cycles. The reaction cycle "0" corresponds to the reduction degree of ceria in Rh/CeO_x samples before TPRs.

described by the reaction of molecular CO and O_2 beams on the surface of Rh particles. This is demonstrated by the reference CO_2 production curve on Rh foil (Fig. 3(c)). Note that CO_2 production on Rh foil occurs between 500 and 750 K. The direct oxidation of CO on cerium oxide support via Mars-van Krevelen (MvK) mechanism [54] can also be ruled out under the present experimental conditions. Fig. 3(d) clearly demonstrates that CO does not react with oxygen from the CeO_x substrate in the used partial pressures. Plausible explanation for the CO_2 production above 750 K would be the reaction of the impinging CO molecules with oxygen provided by cerium oxide support by means of the *reverse* oxygen spillover on Rh. This reaction channel becomes dominant at elevated temperature. Note that the peak (iii) is not clearly resolved on sample (B). This means that unlike on sample (A), the reverse oxygen spillover is suppressed on sample (B) even under steady-state conditions which lead to oxidation of cerium oxide.

Next, we have monitored changes in CO_2 production and reduction degree of ceria support on both Rh/CeO_x (A) and (B) samples during subsequent TPR cycles. The corresponding sets of CO_2 production curves are shown in Fig. 4(a) and (d), respectively. The ratio between molecular beams CO:O_2 was 1:1 during the cycles 1–5 and 1:0 during the cycles 6–8 on Rh/CeO_x (A). In case of the Rh/CeO_x (B), all the TPR were performed at CO:O_2 ratio of 1:1.

The total amounts of CO_2 produced on Rh/CeO_x (A) and Rh/CeO_x (B) during subsequent reaction cycles are plotted in Fig. 4(b) and (e), respectively. It was determined as the total area under the CO_2 production curve after the subtraction of constant background. The plots reveal further differences between the samples Rh/CeO_x (A) and Rh/CeO_x (B). Most importantly, CO_2 production *decreased* on sample (A) but *increased* on sample (B) after several cycles. As seen in Fig. 4(b) and (e), the CO_2 production has got stabilized after the third cycle on both samples.

The instabilities of the CO_2 yield during first three cycles could be the result of morphological changes in the Rh/CeO_x samples under the steady-state reaction conditions and elevated temperature (e.g. formation of larger Rh particles [44]). XPS revealed strong

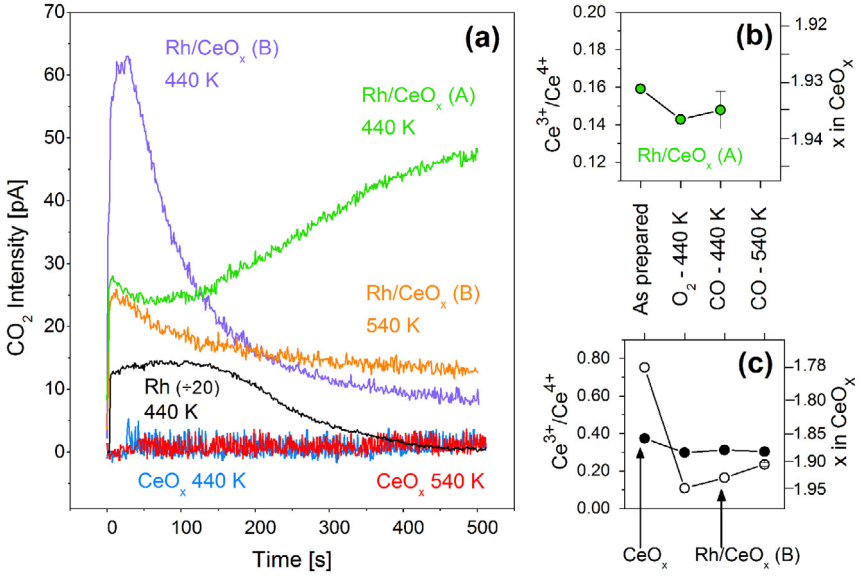

Fig. 5. (a) CO_2 production curves during reaction of CO molecular beam with oxygen pre-exposed Rh/CeO_x (A) and (B), Rh foil, and Rh-free CeO_x (B) at 440 K. The intensity on Rh foil (c) was divided by 20 to fit the scale of the figure. The production curve at 540 K was obtained from Rh/CeO_x (A) without pre-exposure of the sample to oxygen. The evolution of the degrees of ceria reduction, Ce^{3+}/Ce^{4+}, on Rh/CeO_x (A) (b), and Rh-free $CeO_{1.86}$ and Rh/CeO_x (B) (c) during the sample treatment.

re-oxidation of cerium oxide (see Fig. 4(c) and (f)) and a partial coalescence of Rh particles after the first reaction cycle on both samples (data not shown). The evolution of the degree of ceria reduction on Rh/CeO_x (A) and Rh/CeO_x (B) is plotted in Fig. 4(c) and (f), respectively. It indicates re-oxidation of ceria in both Rh/CeO_x (A) and Rh/CeO_x (B) after each reaction cycle carried at molecular beams CO:O_2 ratio of 1:1.

The temperature of CO_2 production maxima is not significantly influenced by the re-oxidation of ceria support in the samples. Only a subtle shift of the peak (i) to lower temperatures has been observed on Rh/CeO_x (B) with increasing number of TPR cycles (Fig. 4(d)).

This suggests that the Rh–CeO_x interaction is not significantly influenced by the re-oxidation of cerium oxide. We assume that the Rh–CeO_x interface remains stable under present experimental conditions. Furthermore, despite re-oxidation of cerium oxide under steady state conditions, the *reverse* oxygen spillover is largely suppressed on Rh/CeO_x (B). This finding is important for the design of the catalyst with tailored properties. The *reverse* oxygen can be enabled and disabled depending on the stoichiometry of the cerium oxide before metal deposition.

Finally, we tested the capacity of Rh/CeO_x (A) for the CO_2 production in absence of molecular O_2. The CO_2 production on the Rh/CeO_x (A) during consecutive TPR cycles at molecular beam ratio CO:O_2 of 1:0 (curves 6–8) is shown in Fig. 4(a). The amount of CO_2 produced in the 6th cycle during heating was comparable to that of the 5th cycle. However, the amount of CO_2 produced in the 6th cycle during cooling was notably smaller. In the 7th cycle, the CO_2 production considerably decreased. Note that 5th TPR cycle caused re-oxidation of cerium oxide while cycles 6–8 induced reduction of ceria (Fig. 4(c)). The reduction of cerium oxide is caused by the removal of lattice oxygen via the *reverse* spillover to Rh during CO_2 production in absence of molecular O_2.

3.4. Suppression of direct oxygen spillover

Fig. 5(a) shows CO_2 production curves recorded during reaction of molecular beams of CO with Rh/CeO_x samples (A) and (B) pre-exposed to 30 L of oxygen at 440 K. As a reference, oxygen pre-exposed Rh foil and Rh-free CeO_x sample (B) have been tested for CO_2 production under the same reaction conditions. After each reaction run, Ce 3*d* core levels were acquired by means of XPS. The evolution of the Ce^{3+}/Ce^{4+} ratio is plotted in Fig. 5(b) and (c).

Pre-exposure of Rh-free CeO_x and Rh/CeO_x samples (A) and (B) to oxygen at 440 K caused re-oxidation of all samples. The exposure of the Rh-free sample (B) to molecular beam of CO did not produce any CO_2 under present experimental conditions. In contrast, CO_2 production was observed on Rh foil and both Rh/CeO_x (A) and (B).

In the case of Rh foil, CO_2 production starts instantly under CO exposure and maintains almost constant rate for about 150 s and then decays to zero after 450 s as all pre-adsorbed oxygen gets depleted. The reaction proceeds according to Langmuir–Hinshelwood reaction mechanism: oxygen pre-adsorbed on rhodium quickly reacts with adsorbing CO to form CO_2.

The shape of CO_2 production curves on two samples (A) and (B) differs significantly. On Rh/CeO_x (B), we observed an abrupt increase of CO_2 production followed by its gradual decrease after approximately 50 s until it is stabilized at non-zero intensity after 450 s. The CO_2 production pattern on this sample is similar to that on Rh foil. However, unlike on Rh foil, the source of oxygen is not completely exhausted at longer reaction times.

On Rh/CeO_x (A), the CO_2 production at the beginning of the reaction is rather small but increased gradually after 50 s until it stabilized after approximately 450 s. It is important to note that CO_2 production was about five times higher on Rh/CeO_x (A) as compared to Rh/CeO_x (B) at 450 s.

The evolution of CO_2 production curves can be explained considering the facility of *direct* oxygen spillover, i.e. spillover of adsorbed atomic oxygen from Rh particles to the support, on Rh/CeO_x (A) and its suppression on Rh/CeO_x (B).

If *direct* spillover of oxygen was allowed on Rh/CeO_x system at 440 K, a fraction of pre-adsorbed oxygen would migrate before the CO exposure from Rh to cerium oxide, where it could occupy the coordinatively unsaturated sites atop the Ce cations. The amount of oxygen on Rh available for the CO oxidation would decrease. Relatively low CO_2 production in initial 50 s of the CO exposure on Rh/CeO_x (A) points to a lesser amount of available oxygen on Rh particles compared to Rh/CeO_x (B) or Rh foil.

On the contrary, if *direct* spillover was *not* allowed, pre-adsorbed oxygen would be confined to the Rh surface. In such case, CO oxidation is intense because the surface is densely populated by pre-adsorbed oxygen. This scenario is consistent with CO_2 production on Rh foil and Rh/CeO_x (B) (Fig. 5(a)).

These results show that in contrast to sample (B), the *direct* oxygen spillover is facile on the sample (A). The increase of CO_2 production after 50 s on Rh/CeO_x (A) indicates an onset of *reverse* spillover of oxygen to Rh particles. Apparently, *reverse* oxygen spillover occurs to some minor extent also on Rh/CeO_x (B), since CO_2 production does not drop to zero under continued CO exposure like it occurred on Rh-foil (Fig. 5(a)). We observed reduction of cerium oxide on both samples, Rh/CeO_x (A) (Fig. 5(b)) and Rh/CeO_x (B) (Fig. 5(c)) that indicates release of oxygen from both supports. The CO_2 production curve obtained during the reaction of molecular beam of CO with Rh/CeO_x (B) at 540 K *without* pre-exposure of the sample to oxygen is shown in Fig. 5(a). The low initial CO_2 production at 540 K is consistent with a shortage of oxygen on Rh particles. However, the intensity of CO_2 signal at 450 s is higher at 540 K than at 440 K. This means that the increase of the reaction temperature enhances CO_2 production via reverse oxygen spillover. Yet, this channel is minor on sample Rh/CeO_x (B).

4. Conclusions

We have investigated the impact of Rh–CeO_x interaction on the catalytic properties of Rh/CeO_x system, namely on its capacity for the *reverse* and *direct* oxygen spillover, in the context of the CO oxidation. The electronic metal–support interaction in Rh/CeO_x system results in buildup of a charge on Rh particles determined by the degree of reduction of cerium oxide prior to Rh deposition. Specifically, a positive charge and reduction of cerium oxide in contrast to a net negative charge and re-oxidation of cerium oxide occurs when Rh is deposited on nearly stoichiometric or partially reduced CeO_x, respectively.

The EMSI effect has a tremendous influence on the mechanisms of CO oxidation on Rh particles supported on cerium oxide. In particular, CO_2 production during the reaction of molecular beams of CO and O_2 is shifted to higher temperature by 150 K on the sample containing Rh particles deposited on the partially reduced cerium oxide with respect to Rh deposited on nearly stoichiometric cerium oxide. The shift of CO_2 production maximum occurs due to stronger CO—Rh bonding on Rh particles deposited on reduced cerium oxide. We found that desorption temperature of molecularly adsorbed CO is shifted to higher temperature by about 75 K on this system as compared to the Rh deposited on stoichiometric cerium oxide.

The most important consequence of the EMSI is suppression of both *reverse* and *direct* oxygen spillover on Rh deposited on partially reduced cerium oxide. Our study suggests that neither lattice oxygen nor the oxygen adsorbed on Rh particles from molecular O_2 beam will migrate between the Rh particles and cerium oxide even under oxidizing (steady state) conditions on this system. In contrast to this, both *reverse* and *direct* oxygen spillover take place on Rh particles supported on nearly stoichiometric cerium oxide. We found that reverse oxygen spillover becomes a dominant channel for CO oxidation above 750 K on Rh particles deposited on nearly stoichiometric cerium oxide.

Acknowledgements

This work was supported by the grants LD13054 and LG12003 provided by the Ministry of Education of the Czech Republic. K.Š. acknowledges the support of the Grant Agency of the Charles University (GAUK 794313). K.Š. thanks Dr. Jiří Libra for the KolXPD software which was used for processing the photoelectron spectra. K.Š. and V.N. thanks Dr. Ivan Khalakhan for complementary AFM measurements and results consultation.

Appendix A. Supplementary data

Supplementary data associated with this article can be found, in the online version, at http://dx.doi.org/10.1016/j.apsusc.2015.01.197.

References

[1] A. Trovarelli, Catalysis by Ceria and Related Metals, Imperial College Press, London, 2002.
[2] D.R. Mullins, S.H. Overbury, CO dissociation on Rh deposited on reduced cerium oxide thin films, J. Catal. 188 (1999) 340–345.
[3] R.M. Ferrizz, T. Egami, J.M. Vohs, Temperature programmed desorption study of the reaction of C_2H_4 and CO on Rh supported on α-Al_2O_3(0 0 0 1), YSZ (1 0 0) and CeO_2 thin films, Surf. Sci. 465 (2000) 127–137.
[4] G.S. Zafiris, R.J. Gorte, Evidence for low-temperature oxygen migration from ceria to Rh, J. Catal. 139 (1993) 561–567.
[5] G.S. Zafiris, R.J. Gorte, Evidence for a second CO oxidation mechanism on Rh/ceria, J. Catal. 143 (1993) 86–91.
[6] G.N. Vayssilov, Y. Lykhach, A. Migani, T. Staudt, G.P. Petrova, N. Tsud, T. Skála, A. Bruix, F. Illas, K.C. Prince, V. Matolín, K.M. Neyman, J. Libuda, Support nanostructure boosts oxygen transfer to catalytically active platinum nanoparticles, Nat. Mater. 10 (2011) 310–315.
[7] W.C. Conner, J.L. Falconer, Spillover in heterogeneous catalysis, Chem. Rev. 95 (1995) 759–788.
[8] T. Bunluesin, E.S. Putna, R.J. Gorte, A comparison of CO oxidation on ceria-supported Pt, Pd, and Rh, Catal. Lett. 41 (1996) 1–5.
[9] M.Y. Smirnov, G.W. Graham, Pd oxidation under UHV in a model Pd/ceria–zirconia catalyst, Catal. Lett. 72 (2001) 39–44.
[10] D.R. Mullins, K. Zhang, Interaction between NO and C_2H_4 on Rh-loaded CeO_x(1 1 1), J. Phys. Chem. B 105 (2001) 1374–1380.
[11] S.D. Senanayake, J. Zhou, A.P. Baddorf, D.R. Mullins, The reaction of carbon monoxide with palladium supported on cerium oxide thin films, Surf. Sci. 601 (2007) 3215–3223.
[12] J. Stubenrauch, J.M. Vohs, Support effects in the dissociation of CO on Rh/CeO_2(1 1 1), Catal. Lett. 47 (1997) 21–25.
[13] Y. Lykhach, T. Staudt, M.P.A. Lorenz, R. Streber, A. Bayer, H.P. Steinrück, J. Libuda, Microscopic insights into methane activation and related processes on Pt/ceria model catalysts, ChemPhysChem 11 (2010) 1496–1504.
[14] H. Cordatos, T. Bunluesin, J. Stubenrauch, J.M. Vohs, R.J. Gorte, Effect of ceria structure on oxygen migration for Rh/ceria catalysts, J. Phys. Chem. 100 (1996) 785–789.
[15] A. Migani, G.N. Vayssilov, S.T. Bromley, F. Illas, K.M. Neyman, Greatly facilitated oxygen vacancy formation in ceria nanocrystallites, Chem. Commun. 46 (2010) 5936–5938.
[16] A. Bruix, J.A. Rodriguez, P.J. Ramírez, S.D. Senanayake, J. Evans, J.B. Park, D. Stacchiola, P. Liu, J. Hrbek, F. Illas, A new type of strong metal–support interaction and the production of H_2 through the transformation of water on Pt/CeO_2(1 1 1) and Pt/CeO_x/TiO_2(1 1 0) catalysts, J. Am. Chem. Soc. 134 (2012) 8968–8974.
[17] G. Pacchioni, Electronic interactions and charge transfers of metal atoms and clusters on oxide surfaces, Phys. Chem. Chem. Phys. 15 (2013) 1737–1757.
[18] Y.-G. Wang, Y. Yoon, V.-A. Glezakou, J. Li, R. Rousseau, The role of reducible oxide–metal cluster charge transfer in catalytic processes: new insights on the catalytic mechanism of CO oxidation on Au/TiO_2 from ab initio molecular dynamics, J. Am. Chem. Soc. 135 (2013) 10673–10683.
[19] Z. Jiang, W. Zhang, L. Jin, X. Yang, F. Xu, J. Zhu, W. Huang, Direct XPS evidence for charge transfer from a reduced rutile TiO_2(1 1 0) surface to Au clusters, J. Phys. Chem. C 111 (2007) 12434–12439.
[20] T. Skála, F. Šutara, M. Škoda, K.C. Prince, V. Matolín, Palladium interaction with CeO_2, Sn—Ce—O and Ga—Ce—O layers, J. Phys.: Condens. Matter 21 (2009) 0550051 (9 pp).
[21] J. Matharu, G. Cabailh, R. Lindsay, C.L. Pang, D.C. Grinter, T. Skala, G. Thornton, Reduction of thin-film ceria on Pt(1 1 1) by supported Pd nanoparticles probed with resonant photoemission, Surf. Sci. 605 (2011) 1062–1066.
[22] M. Škoda, M. Cabala, I. Matolínová, K.C. Prince, T. Skála, F. Šutara, K. Veltruská, V. Matolín, Interaction of Au with CeO_2(1 1 1): a photoemission study, J. Chem. Phys. 130 (2009) 0347031 (7 pp).
[23] P. Luches, F. Pagliuca, S. Valeri, F. Illas, G. Preda, G. Pacchioni, Nature of Ag islands and nanoparticles on the CeO_2(1 1 1) surface, J. Phys. Chem. C 116 (2011) 1122–1132.
[24] L. Szabová, T. Skála, I. Matolínová, S. Fabris, M. Farnesi Camellone, V. Matolín, Copper–ceria interaction: a combined photoemission and DFT study, Appl. Surf. Sci. 267 (2013) 12–16.
[25] F. Gao, Y. Cai, K.K. Gath, Y. Wang, M.S. Chen, Q.L. Guo, D.W. Goodman, CO oxidation on Pt-group metals from ultrahigh vacuum to near atmospheric pressures. 1. Rhodium, J. Phys. Chem. C 113 (2009) 182–192.
[26] H. Falsig, B. Hvolbæk, I.S. Kristensen, T. Jiang, T. Bligaard, C.H. Christensen, J.K. Nørskov, Trends in the catalytic CO oxidation activity of nanoparticles, Angew. Chem. Int. Ed. 47 (2008) 4835–4839.

[27] I.V. Yudanov, A. Genest, S. Schauermann, H.-J. Freund, N. Rösch, Size dependence of the adsorption energy of CO on metal nanoparticles: a DFT search for the minimum value, Nano Lett. 12 (2012) 2134–2139.
[28] B.R. Cuenya, Synthesis and catalytic properties of metal nanoparticles: size, shape, support, composition, and oxidation state effects, Thin Solid Films 518 (2010) 3127–3150.
[29] M. Haruta, Size- and support-dependency in the catalysis of gold, Catal. Today 36 (1997) 153–166.
[30] S.H. Joo, J.Y. Park, J.R. Renzas, D.R. Butcher, W. Huang, G.A. Somorjai, Size effect of ruthenium nanoparticles in catalytic carbon monoxide oxidation, Nano Lett. 10 (2010) 2709–2713.
[31] S.H. Overbury, V. Schwartz, D.R. Mullins, W. Yana, S. Dai, Evaluation of the Au size effect: CO oxidation catalyzed by Au/TiO_2, J. Catal. 241 (2006) 56–65.
[32] M. Cargnello, V.V.T. Doan-Nguyen, T.R. Gordon, R.E. Diaz, E.A. Stach, R.J. Gorte, P. Fornasiero, C.B. Murray, Control of metal nanocrystal size reveals metal–support interface role for ceria catalysts, Science 341 (2013) 771–773.
[33] E.S. Putna, R.J. Gorte, J.M. Vohs, G.W. Graham, Evidence for enhanced dissociation of CO on Rh/ceria, J. Catal. 178 (1998) 598–603.
[34] V. Nehasil, K. Ševčíková, T. Zahoranová, Photoemission and thermo-programmed reaction study of the catalytic properties of Rh/CeO_2 system, Surf. Interface Anal. 42 (2010) 931–934.
[35] T. Skála, F. Šutara, K.C. Prince, V. Matolín, Cerium oxide stoichiometry alteration via Sn deposition: influence of temperature, J. Electron Spectrosc. Relat. Phenom. 169 (2009) 20–25.
[36] T. Skála, F. Šutara, M. Cabala, M. Škoda, K.C. Prince, V. Matolín, A photoemission study of the interaction of Ga with CeO_2(1 1 1) thin films, Appl. Surf. Sci. 254 (2008) 6860–6865.
[37] A. Pfau, K.D. Schierbaum, W. Göpel, The electronic structure of CeO_2 thin films: the influence of Rh surface dopants, Surf. Sci. 331–333 (331) (1995) 1479–1480.
[38] Z. Lu, Z. Yang, Interfacial properties of NM/CeO_2(1 1 1) (NM = noble metal atoms or clusters of Pd, Pt and Rh): a first principles study, J. Phys.: Condens. Matter 22 (2010) 475003 (10 pp).
[39] Y. Lykhach, V. Johánek, H. Alexandrov, S.M. Kozlov, M. Happel, T. Skála, P.S. Petkov, N. Tsud, G.N. Vayssilov, K.C. Prince, K.M. Neyman, V. Matolín, J. Libuda, Water chemistry on model ceria and Pt/ceria catalysts, J. Phys. Chem. C 116 (2012) 12103–12113.
[40] F. Sadi, D. Duprez, F. Gérard, A. Miloudi, Hydrogen formation in the reaction of steam with Rh/CeO_2 catalysts: a tool for characterising reduced centres of ceria, J. Catal. 213 (2003) 226–234.
[41] Z. Yang, G. Luo, Z. Lu, T.K. Woo, K. Hermansson, Structural and electronic properties of NM-doped ceria (NM = Pt, Rh): a first-principles study, J. Phys.: Condens. Matter 20 (2008) 035210 (7 pp).
[42] J.F. Moulder, W.F. Stickle, P.E. Sobol, K.D. Bomben, Handbook of X-ray Photoelectron Spectroscopy, Perkin-Elmer Corporation, Minnesota, USA, 1992.
[43] J. Radnik, C. Mohr, P. Claus, On the origin of binding energy shifts of core levels of supported gold nanoparticles and dependence of pretreatment and material synthesis, Phys. Chem. Chem. Phys. 5 (2003) 172–177.
[44] J. Zhou, A.P. Baddorf, D.R. Mullins, S.H. Overbury, Growth and characterization of Rh and Pd nanoparticles on oxidized and reduced CeO_x(1 1 1) thin films by scanning tunneling microscopy, J. Phys. Chem. C 112 (2008) 9336–9345.
[45] S. Penner, D. Wang, R. Podloucky, R. Schlögl, K. Hayek, Rh and Pt nanoparticles supported by CeO_2: metal–support interaction upon high-temperature reduction observed by electron microscopy, Phys. Chem. Chem. Phys. 6 (2004) 5244–5249.
[46] C. Berg, S. Raaen, An X-ray photoemission study of Ce–Rh, Ce–Pd and Ce–Ag interfaces, J. Phys.: Condens. Matter 4 (1992) 8021–8028.
[47] M. Juel, S. Martinsen, S. Raaen, Oxidation of thin Ce layers on Rh(1 1 0), Thin Solid Films 517 (2008) 805–810.
[48] A. Baraldi, L. Gregoratti, G. Comelli, V.R. Dhanak, M. Kiskinova, R. Rosei, CO adsorption and CO oxidation on Rh(1 0 0), Appl. Surf. Sci. 99 (1996) 1–8.
[49] T.W. Root, L.D. Schmidt, G.B. Fisher, Nitric oxide reduction by CO ON Rh(1 1 1): temperature programmed reaction, Surf. Sci. 150 (1985) 173–192.
[50] S. Schwegmann, H. Over, V. De Renzi, G. Ertl, The atomic geometry of the O and CO + O phases on Rh(1 1 1), Surf. Sci. 375 (1997) 91–106.
[51] D.L.S. Nieskens, M.M.M. Jansen, A.P. van Bavel, D. Curulla-Ferre, J.W. Niemantsverdriet, The influence of carbon on the adsorption of CO on a Rh(1 0 0) single crystal, Phys. Chem. Chem. Phys. 8 (2006) 624–632.
[52] G. Blyholder, Molecular orbital view of chemisorbed carbon monoxide, J. Phys. Chem. 68 (1964) 2772–2777.
[53] T. Engel, G. Ertl, Elementary steps in the catalytic oxidation of carbon monoxide on platinum metals, Adv. Catal. 28 (1979) 1–78.
[54] M. Huang, S. Fabris, C.O. Adsorption, Oxidation on ceria surfaces from DFT + U calculations, J. Phys. Chem. C 112 (2008) 8643–8648.